DELTA DYNAMICS: UNDERSTANDING PROCESS, PATTERN, AND PEOPLE USING REMOTE SENSING AND SYSTEMS ANALYSIS IN COASTAL LOUISIANA AND AMAZON RIVER DELTA

Samapriya Roy

Submitted to the faculty of the University Graduate School

in partial fulfillment of the requirements

for the degree Doctor of Philosophy

in the Department of Geography, Indiana University

July 2019

Accepted by the Graduate Faculty, Indiana University, in partial fulfillment of the requirements for the degree of Doctor of Philosophy.

Doctoral Committee

Scott Robeson, PhD

Douglas Edmonds, PhD

Taehee Hwang, PhD

Eduardo Brondizio, PhD

April 22, 2019

Acknowledgments

One of the most challenging moments in my doctoral pursuit was figuring out the problem I wanted to work on. This challenging time made me try, and fail and try again, and keep changing approaches. Throughout this process, I was lucky to have found mentors, friends, and family who pushed with me just a nudge at a time. The “why” behind why we do research has always been fascinating to me because my approach has always been about problem-solving, which is likely a carryover from my days as an engineer. Science, as per me, should be eclectic; it should be simple; it should be approachable and reproducible and beautiful and not exclusive in any way. I hope that my research touches upon at least a few facets of that goal.

I want to take the time to thank my committee members who in some way or the other kept me grounded and let me evolve with my ideas. I think sometimes the hardest thing for an international student is to find an extended support group, a version of “family” away from home. To that end, I would like to thank the office staff in the Geography Department namely Susan White and Kristi Carlson, those early morning conversations with them kept me connected. I want to thank my family for being supportive, for trusting me while I was still figuring things out for myself and doing this without expectations. I was lucky to have amazing friends like Landon Yoder who gave me comments and edits and have spent a lot of time with me trying to teach me everything from topic sentences to relearning approaches in writing. Also, none of this would have been possible without the presence of my best friend, mentor, and partner Briana Whitaker. I think I like to borrow the idea from quantum entanglements. We are entangled with a few people even at a distance, in every good way that I can think of, in effects that are independent of time. Thank you for all of these experiences.

Samapriya Roy

DELTA DYNAMICS: UNDERSTANDING PROCESS, PATTERN, AND PEOPLE USING REMOTE SENSING AND SYSTEMS ANALYSIS IN COASTAL LOUISIANA AND AMAZON RIVER DELTA

My dissertation research spans several topics in spatial landscape theory. In the first project, I examined the temporal dynamics of land loss in the Lower Mississippi River Delta (LMRD), with a focus on identifying temporal stability and spatial patterns of loss. After creating composite images that were classified into land and water, I developed and used a novel stability index to quantify the transitionary behavior of land and water pixels. I found that while most land in LMRD is lost in a single transition (nearly 75%) the remaining 25% of the land area undergoes multiple transitions between land and water before permanently transitioning to water. This indicates that there dynamic nature of deltaic land loss and the importance of repeated measurements across varying time scales to understand delta stability. For the second part of the LMRD project, I used multi-sensor analysis to analyze land loss and fragmentation at varying spatial, temporal, and spectral resolutions. I found that finer spatio-temporal resolution more effectively removes atmospheric anomalies, such as cloud and haze, and improves quantitative estimates of land loss. At the same time, higher spectral resolution allowed us to differentiate land and water better. In a third project on the Amazon River Delta (ARD), I applied a novel methodology using multilayer network analysis coupled with remote sensing approaches to improve spatial estimates of urban flood vulnerability in Belem, Brazil. I created an adjusted vulnerability index using indicator variables to improve on estimates from urbanicity, permeability, and link to flooding potential. I found that there are stark differences in vulnerability between planned and unplanned settlements. Through my dissertation research, I have provided evidence for the importance of using high spatial

and temporal resolutions in delta landscapes. The novel methods that I have developed provide better estimates of land loss and the associated vulnerability to flooding in delta environments. This work can be extended to other delta regions of the world in future research to assess vulnerability as sea-level continues to rise and populations in delta environments increase.

Scott Robeson, PhD

Douglas Edmonds, PhD

Taehee Hwang, PhD

Eduardo Brondizio, PhD

Table of Contents

Chapter 1: Introduction

Globally, deltas remain some of the most populated and vulnerable regions of the world – with a higher population growth rate than the global average (Costa and Brondízio, 2011; Edmonds et al., 2017; Syvitski et al., 2009). Deltaic populations are growing at 1.59% per year, which outpaces the world growth rate of 1.11%. As a result, average population densities in deltas are high and increasing with time, rising from 322 people/km^2 in 2000 to projected values of 422 people/km^2 by 2020 (Edmonds et al., 2017). High population densities, coupled with climate change and natural and anthropogenic modifications, put deltas around the world under constant threat of flooding, degradation, and loss (Mansur et al., 2016; Overeem and Brakenridge, 2009; Syvitski et al., 2009). Despite the incredible importance of deltas to ecological productivity and people's livelihood, they are extremely vulnerable to land loss. Substantial anthropogenic modifications of delta processes and environments have accelerated the natural delta cycle which consists of time dependent delta formation and degradation. The acceleration in the delta cycle has subsequently contributed to increased flooding and associated land loss in deltas across the globe (Newton et al., 2012; Renaud and Kuenzer, 2012; Syvitski et al., 2009; Tessler et al., 2015).

In deltaic environments, the extent of flooding, along with land and water morphology, serve as proxies or indicators of the processes driving land loss. Despite the potential value of deltas to ecological dynamics, including overall productivity and value of ecosystem services, we continue to lack finer resolution understanding of how much and where land is converting to water. Analyzing spatial changes in morphology of degrading wetlands requires high temporal and spatial resolution that allows pixel-level examination of the changing spatial and temporal extent. Similarly, understanding the socio-economic vulnerability of people living in these delta areas allows us to understand why these areas have the highest population densities despite being some of the most threatened landscapes.

Large populations living in the delta area over the next couple of decades will experience increasing vulnerability owing to flooding extent combined with socioeconomic vulnerability. (Edmonds et al., 2017; Overeem and Brakenridge, 2009; Syvitski et al., 2009; Tessler et al., 2015). Delta dynamics has hence long been considered essential to understanding delta vulnerability. River deltas across the globe are starved of riverine sediment load, and plagued by increased storm surges, and sea-level rise (Rabalais et al., 2002; Turner and Rabalais, 1991; Walling, 2008; Walling and Fang, 2003). The additional loss of land area due to human development and pollution further reduces delta ecosystem resilience by exposing vital infrastructure to increased storm damage (Adger and Kelly, 2012; Janssen, 2007; Renaud and Kuenzer, 2012). While land loss estimates have been a reliable source of estimating the current health of landscapes, rapidly changing landscape such as deltas require frequent and robust methods of land loss and change detection. This dissertation has two primary objectives: i) assessing morphological changes in terms of land-water boundaries and associated land loss across the Louisiana coastline using high-resolution remote sensing approaches and ii) assessed flood vulnerability and its change with increasing urbanization in Belem, an urban delta system within the Amazon River Delta (ARD). The following three chapter titles represent the summation of these works.

Chapter 2 – Spatial and temporal patterns of land loss in the Mississippi River Delta, 1980-2016

Chapter 3 – Remotely sensed measurement of land loss and gain in the Lower Mississippi River Delta using Landsat, Sentinel-2, and PlanetScope within the Google Earth Engine

Chapter 4 – Urban Flood Vulnerability in Belém, Brazil: Application of Adjusted Vulnerability Index using Multilayer Geo-constrained Networks

1.1 Research significance and contributions

In the following sections, I summarize the main contributions of my research. I will discuss the research topics in full in the later chapters.

Two chapters of my dissertation deal with spatial and temporal scale patterns in the LMRD. For the second chapter, my research develops a new understanding of delta morphology and land loss dynamics using long-term data from Landsat missions (Chander and Markham, 2003; Hansen and Loveland, 2012; Roy et al., 2010). The ultimate goals of this section of the study were to 1) understand the magnitude and patterns of land change and land loss 2) evaluate periodic stability of a land pixel transitioning to water using a novel stability index and 3) assess periodicity and morphology of land loss in deltaic landscapes. I created a temporally rich and spatio-temporally consistent dataset to analyze land-water conversions, identify the dominant transformations (i.e., loss or gain) within each watershed boundary, and evaluate the patterns of change using landscape and class metrics. The work leverages big data and distributed computing (Donchyts et al., 2016; Gorelick et al., 2017; Shelestov et al., 2017) to produce novel products utilizing a time-series, sub-pixel classification, which ultimately enhances our understanding of land-water transitions. This study allowed me to both qualitatively and quantitatively analyze multiple facets of deltaic land loss via visual interpretation of maps and spatial clustering analyses, respectively.

The third chapter of my dissertation revisits the LMRD and augments my long-term spatio-temporal analysis of land loss to further examine land loss estimates as a function of the sensor characteristics. To do this, I investigated how the use of different spatial, temporal, and spectral resolution affects our understanding of land loss patterns in river deltas. A secondary aim of this chapter was to develop a streamlined workflow for users to incorporate multiple satellite sensors into their research studies (Tolle et al., 2011; Wilkinson et al., 2016). We derived land loss estimates from Landsat, Sentinel, and PlanetScope constellation sensors with spatial resolutions set at 30m, 20-10m, and 3m (respectively) and with a temporal resolution of 16 days, 5 days and 1 day (respectively). My analyses applied a monotonic trend using the Mann-Kendall statistic (Bogucki et al., 2012; Hamed, 2008; Hamed and Rao, 1998) for both index based (Normalized Difference Water Index) (Gao, 1996; McFeeters, 1996; Xu, 2006) and constrained spectral-unmixing (Keshava, 2003; Keshava and Mustard, 2002) based land loss analysis. We found large scale variability in the estimated land loss across all three sensors. Interannual scales introduce significant signal to noise ratios which tend to over and underestimate overall loss across shorter temporal windows. As climate events become more stochastic and with improvements in Earth Observation systems, short-term assessment of landscape changes will be critical to understanding the overall health of the delta region.

In my fourth chapter, I examined anthropogenic vulnerability and adaptation among communities living in deltaic landscapes to urban flooding. My analysis within the Metropolitan area of Belem, Brazil took into consideration different spatial units such as census sectors and bairros as well as social units designated as planned and unplanned settlements. In my work, I developed a novel index known as the adjusted vulnerability index (AVI) to examine the effects of spatial clustering and dispersion of social-economic variables on the overall vulnerability experienced by census sector as the finest spatial unit. My work further leverages remote sensing methodologies to generate high spatial and temporal resolution land cover datasets (Antrop and Van Eetvelde, 2000; Azzari and Lobell, 2017; Gorelick et al., 2017) along with climate datasets such as precipitation (Funk et al., 2015; Katsanos et al., 2016) and tide (Flater, 1998, 1996) that serve as proxy indicators describing how vulnerability is clustered within the city. I combine multiple methods such as Analytical hierarchical process (AHP), Local Indicator of Spatial Autocorrelation (for spatial clustering) and a multilayer network analysis to create the AVI (Anselin, 1995; Ord and Getis, 2001;

Saaty, 1987, 2008). This study allowed me to both assess the spatial and social distribution of vulnerability across varying spatial scales. The method I developed could be used for adding a temporal dimension to understand evolving changes in urban vulnerability to flooding.

1.2 Dissertation structure

This dissertation has three main parts:

The second chapter is dedicated to assessing the overall land loss by area and by morphology within the Lower Mississippi River Basin (LMRB). The idea for this paper was developed during discussions with the author's co-advisors (Douglas Edmonds & Scott Robeson). The author did the paper write-up, and data analysis for this paper and his co-advisors provided detailed feedback and comments, and another coauthor (Alejandra Ortiz) provided detailed feedback and comments.

The third chapter revisits the first paper and is on improving estimates of land loss using multiple remote sensing sensors within the Lower Mississippi River Basin (LMRB). The author developed the idea of this paper. The author led the paper to write up and data analysis while detailed feedbacks were provided by his advisor (Douglas Edmonds) and coauthors (Tyson Swetnam and Joseph Mascaro). This paper is being prepared for publication in the *Remote Sensing of Environment*.

The fourth chapter is on estimating spatially adjusted urban vulnerability to flooding in the urban delta, in our case, Belem, Brazil. The author developed the idea of this paper. The author led the paper write-up and data analysis with feedback from his committee member (Eduardo Brondizio) and coauthors (Landon Yoder and Vitor Dias). Vitor Dias collected the in situ data for this paper in the summer of 2018. This paper is being prepared for publication in *Sustainability Science* as a follow up to our earlier paper (Mansur et al., 2016).

The author published an additional second author, as well as three third-author papers. An additional third-author paper and one fifth-author paper are in review. These co-authored works are relevant to the overall dissertation topic, but they are not discussed here to maintain brevity and have been included in the CV for completeness.

References

Adger, W.N., Kelly, P.M., 2012. Social vulnerability and resilience, in: Living with Environmental Change. Routledge, pp. 41–56.

Anselin, L., 1995. Local indicators of spatial association—LISA. Geographical analysis 27, 93–115.

Antrop, M., Van Eetvelde, V., 2000. Holistic aspects of suburban landscapes: visual image interpretation and landscape metrics. Landscape and urban planning 50, 43–58.

Azzari, G., Lobell, D.B., 2017. Landsat-based classification in the cloud: An opportunity for a paradigm shift in land cover monitoring. Remote Sensing of Environment 202, 64–74.

Bogucki, D.J., Bormann, F.H., Box, E.O., Bratton, S.P., Dolan, R., Dunn, C.P., Forman, R.T.T., Gruendling, G.K., Guntenspergen, G.R., Hayes, T.D., 2012. Landscape heterogeneity and disturbance. Springer Science & Business Media.

Chander, G., Markham, B., 2003. Revised Landsat-5 TM radiometric calibration procedures and postcalibration dynamic ranges. IEEE Transactions on geoscience and remote sensing 41, 2674–2677.

Costa, S.M., Brondízio, E.S., 2011. Cities along the floodplain of the Brazilian Amazon: characteristics and trends, in: The Amazon Várzea. Springer, pp. 83–97.

Donchyts, G., Baart, F., Winsemius, H., Gorelick, N., Kwadijk, J., van de Giesen, N., 2016. Earth's surface water change over the past 30 years. Nature Climate Change 6, 810.

Edmonds, D., Caldwell, R., Baumgardner, S., Paola, C., Roy, S., Nelson, A., Nienhuis, J., 2017. A global analysis of human habitation on river deltas, in: EGU General Assembly Conference Abstracts. p. 10832.

Flater, D., 1998. XTide Manual: Harmonic tide clock and tide predictor. EUA Google Scholar.

Flater, D., 1996. A brief introduction to XTide. Linux Journal 1996, 6.

Funk, C., Peterson, P., Landsfeld, M., Pedreros, D., Verdin, J., Shukla, S., Husak, G., Rowland, J., Harrison, L., Hoell, A., 2015. The climate hazards infrared precipitation with stations—a new environmental record for monitoring extremes. Scientific data 2, 150066.

Gao, B.-C., 1996. NDWI—A normalized difference water index for remote sensing of vegetation liquid water from space. Remote sensing of environment 58, 257–266.

Gorelick, N., Hancher, M., Dixon, M., Ilyushchenko, S., Thau, D., Moore, R., 2017. Google Earth Engine: Planetary-scale geospatial analysis for everyone. Remote Sensing of Environment 202, 18–27.

Hamed, K.H., 2008. Trend detection in hydrologic data: the Mann–Kendall trend test under the scaling hypothesis. Journal of hydrology 349, 350–363.

Hamed, K.H., Rao, A.R., 1998. A modified Mann-Kendall trend test for autocorrelated data. Journal of hydrology 204, 182–196.

Hansen, M.C., Loveland, T.R., 2012. A review of large area monitoring of land cover change using Landsat data. Remote sensing of Environment 122, 66–74.

Janssen, M.A., 2007. An update on the scholarly networks on resilience, vulnerability, and adaptation within the human dimensions of global environmental change. Ecology and Society 12.

Katsanos, D., Retalis, A., Michaelides, S., 2016. Validation of a high-resolution precipitation database (CHIRPS) over Cyprus for a 30-year period. Atmospheric Research 169, 459–464.

Keshava, N., 2003. A survey of spectral unmixing algorithms. Lincoln laboratory journal 14, 55–78.

Keshava, N., Mustard, J.F., 2002. Spectral unmixing. IEEE signal processing magazine 19, 44–57.

Mansur, A.V., Brondízio, E.S., Roy, S., Hetrick, S., Vogt, N.D., Newton, A., 2016. An assessment of urban vulnerability in the Amazon Delta and Estuary: a multi-criterion index of flood exposure, socio-economic conditions and infrastructure. Sustainability Science 11, 625–643.

McFeeters, S.K., 1996. The use of the Normalized Difference Water Index (NDWI) in the delineation of open water features. International journal of remote sensing 17, 1425–1432.

Newton, A., Carruthers, T.J., Icely, J., 2012. The coastal syndromes and hotspots on the coast. Estuarine, Coastal and Shelf Science 96, 39–47.

Ord, J.K., Getis, A., 2001. Testing for local spatial autocorrelation in the presence of global autocorrelation. Journal of Regional Science 41, 411–432.

Overeem, I., Brakenridge, R.G., 2009. Dynamics and vulnerability of delta systems. GKSS Research Centre, LOICZ Internat. Project Office, Inst. for Coastal Research.

Rabalais, N.N., Turner, R.E., Scavia, D., 2002. Beyond Science into Policy: Gulf of Mexico Hypoxia and the Mississippi River: Nutrient policy development for the Mississippi River watershed reflects the accumulated scientific evidence that the increase in nitrogen loading is the primary factor in the worsening of hypoxia in the northern Gulf of Mexico. AIBS Bulletin 52, 129–142.

Renaud, F.G., Kuenzer, C., 2012. The Mekong Delta system: Interdisciplinary analyses of a river delta. Springer Science & Business Media.

Roy, D.P., Ju, J., Kline, K., Scaramuzza, P.L., Kovalskyy, V., Hansen, M., Loveland, T.R., Vermote, E., Zhang, C., 2010. Web-enabled Landsat Data (WELD): Landsat ETM+

composited mosaics of the conterminous United States. Remote Sensing of Environment 114, 35–49.

Saaty, R.W., 1987. The analytic hierarchy process—what it is and how it is used. Mathematical modelling 9, 161–176.

Saaty, T.L., 2008. Decision making with the analytic hierarchy process. International journal of services sciences 1, 83–98.

Shelestov, A., Lavreniuk, M., Kussul, N., Novikov, A., Skakun, S., 2017. Exploring Google Earth Engine platform for big data processing: classification of multi-temporal satellite imagery for crop mapping. Frontiers in Earth Science 5, 17.

Syvitski, J.P., Kettner, A.J., Overeem, I., Hutton, E.W., Hannon, M.T., Brakenridge, G.R., Day, J., Vörösmarty, C., Saito, Y., Giosan, L., 2009. Sinking deltas due to human activities. Nature Geoscience 2, 681–686.

Tessler, Z.D., Vörösmarty, C.J., Grossberg, M., Gladkova, I., Aizenman, H., Syvitski, J.P.M., Foufoula-Georgiou, E., 2015. Profiling risk and sustainability in coastal deltas of the world. Science 349, 638–643.

Tolle, K.M., Tansley, D.S.W., Hey, A.J., 2011. The fourth paradigm: Data-intensive scientific discovery [point of view]. Proceedings of the IEEE 99, 1334–1337.

Turner, R.E., Rabalais, N.N., 1991. Changes in Mississippi River Water Quality This Century. Bioscience 41, 140–147.

Walling, D.E., 2008. The changing sediment load of the Mekong River. Ambio 37, 150–157.

Walling, D.E., Fang, D., 2003. Recent trends in the suspended sediment loads of the world's rivers. Glob. Planet. Change 39, 111–126.

Wilkinson, M.D., Dumontier, M., Aalbersberg, I.J.J., Appleton, G., Axton, M., Baak, A., Blomberg, N., Boiten, J.-W., da Silva Santos, L.B., Bourne, P.E., Bouwman, J., Brookes, A.J., Clark, T., Crosas, M., Dillo, I., Dumon, O., Edmunds, S., Evelo, C.T., Finkers, R., Gonzalez-Beltran, A., Gray, A.J.G., Groth, P., Goble, C., Grethe, J.S., Heringa, J., ’t Hoen, P.A.C., Hooft, R., Kuhn, T., Kok, R., Kok, J., Lusher, S.J., Martone, M.E., Mons, A., Packer, A.L., Persson, B., Rocca-Serra, P., Roos, M., van Schaik, R., Sansone, S.-A., Schultes, E., Sengstag, T., Slater, T., Strawn, G., Swertz, M.A., Thompson, M., van der Lei, J., van Mulligen, E., Velterop, J., Waagmeester, A., Wittenburg, P., Wolstencroft, K., Zhao, J., Mons, B., 2016. The FAIR Guiding Principles for scientific data management and stewardship. Sci Data 3, 160018.

Xu, H., 2006. Modification of normalised difference water index (NDWI) to enhance open water features in remotely sensed imagery. International journal of remote sensing 27, 3025–3033.

Chapter 2

Title: Spatial and temporal patterns of land loss in the Lower Mississippi River Delta, 1984-2016

Authors: Samapriya Roy[1], Scott M. Robeson[1], Alejandra C. Ortiz[2], Douglas Edmonds[3]

[1]Department of Geography, Indiana University, Bloomington, [2]Department of Civil, Construction, and Environmental Engineering, North Carolina State University, Raleigh, North Carolina [3]Department of Earth and Atmospheric Sciences, Indiana University, Bloomington

Corresponding Author: *Samapriya Roy, email: roysam@iu.edu*

Abstract

The Mississippi Delta in coastal Louisiana has some of the highest rates of land loss in the world. This land-loss crisis is likely to become a global problem because most major deltas are expected to be vulnerable to land loss during the remainder of the 21st century and beyond. Despite this predicament, we lack basic information regarding how land loss in a deltaic environment proceeds in time and space. Here, we evaluate the spatial and temporal trends of land loss and gain in the Lower Mississippi River Delta (LMRD) region and then examine the spatial patterns of overall loss using landscape metrics. We used nearly 4800 Landsat images to construct a series of three-year cloud-free composites from 1983 to 2016. From these data, we created a stability index (SI), which is a dimensionless measure of the number of land-to-water transitions that a land pixel makes before converting permanently to water. We then used a local indicator of spatial association to assess spatial clustering of land loss and to further assess the spatial morphology using patch density and shape metrics. Our results indicate that 75% of land loss is a single transition from land to water, while about 25% of land pixels have two or more transitions before changing to water. Our analysis further shows that the land-loss area within the spatial patches with both high and low stability (or high and low values of SI) is strongly related to the density of land patches and their shape (R^2 of 0.717 and 0.545 respectively). Furthermore, our work suggests that using the SI, in combination with local spatial autocorrelation analysis and landscape metrics, serves as an effective tool to monitor and analyze land loss in deltaic environments.

Keywords: land loss, fragmentation, LISA, Fragstats, Google Earth Engine, Landsat

2.1. Introduction

Though deltas cover less than 3% of Earth's land surface, they are home to some of the world's highest population densities and biodiversity (Austin, 2006; Ericson et al., 2006; Syvitski et al., 2009; Tessler et al., 2015). Despite the incredible importance of deltas to ecological productivity and people's livelihoods, they are extremely vulnerable to land loss given their proximity to the sea. The land-loss problem is exacerbated by human activities upstream; people have extensively modified rivers and deltas through channelization and damming, which has decreased sedimentation delivery. The decreased delivery of sediments to deltas, coupled with rises in sea level, has led to increased flooding and land loss in deltas worldwide (Newton et al., 2012; Renaud and Kuenzer, 2012; Syvitski et al., 2009).

Despite the potential value of deltas to ecological services and productivity, we lack a clear picture of spatio-temporal patterns and magnitude of land loss (Blum and Roberts, 2012, 2009; Day et al., 2007, 2000; Lam et al., 2018; Ortiz et al., 2017). The MRD accounts for more than 30% of the coastal wetlands in the United States and has the fourth largest basin area and seventh largest water discharge in the world. The Mississippi River Delta

(MRD), based on subsidence from 1956-1990 has suffered a wetland loss amounted to over 3400 km^2 or about 25% of the overall deltaic wetlands (Blum and Roberts, 2012, 2009; Day et al., 2007, 2000; Morton, 2003). These characteristics make the MRD one of the largest and most ecologically essential deltas in the world and serve as an ideal model for creating sustainable solutions to land loss.

Previous studies of land loss in the MRD relied on hand-drawn maps, ground sampling, and early satellite data. (Britsch and Dunbar, 1993; Couvillion et al., 2011; Craig et al., 1979; Houck, 1983; Penland et al., 2000a). These early studies convincingly demonstrated the severity of the land loss problem over long periods. But, as we move toward designing sustainable solutions for the MRD, we also need to know how land loss operates over shorter timescales. Unfortunately, existing methods are not easily applied to shorter periods because the methods are imprecise and also because the land loss is dynamic. To create more reliable short-term estimates of land loss, we take advantage of the improved capability to create time-series composites and perform parallelized operations on time stacks of imagery (Donchyts et al., 2016a, 2016b; Hansen et al., 2014; Pekel et al., 2016) that produce more temporally consistent datasets.

In this paper, we develop a new approach to the land-loss problem in the Lower Mississippi River Delta (LMRD) to explore the spatial and temporal pattern of permanent land loss. We have defined land to be permanently lost, only if it transitions from land to water and remains as water for the last two periods of observation. We address three core research questions to examine the patterns of deltaic land loss in the LMRD from 1983 to 2016. 1) What proportion of land loss undergoes single versus multiple transitions? 2) Are single or multiple transition pixels spatially clustered or dispersed? 3) Do these spatial clusters have varying morphologies? Our methodology uses a novel concept of stability index as a temporal measure of land water dynamics and land loss trajectory evaluating land loss as a continuous process instead of a single snapshot in time.

In recent years, the methods used to detect and decipher the spatial patterns of land loss have improved considerably, especially with substantial improvements in cloud computing and the capability to analyze deep time stacks of imagery (Donchyts et al., 2016a, 2016b; Gorelick et al., 2017). In addition to the challenges of analyses at high spatio-temporal resolution, most previous analyses focus on permanent land loss (Britsch and Dunbar, 1993, 1993; Couvillion et al., 2011; Penland et al., 2000b). But, not all land loss is permanent, as coastal land can transition from land to water and back to land again over periods ranging from months or years. Herein, we define two broad types of land loss: i) single-transition land loss occurs when land transitions once and becomes water permanently (over the course of our study), and ii) multiple-transition land loss occurs when one or more land-to-water transitions precede the permanent loss from land to water.

These two types of land loss are rarely separated in coastal studies of the LMRD and can provide clues into the processes driving land loss. For example, coastal erosion acts on marsh edges that are exposed continuously to waves and ocean currents (Bernier et al., 2006; Blum and Roberts, 2009; Britsch and Dunbar, 1993; Couvillion et al., 2016, 2011; Day et al., 2000; Kesel, 1989; Penland et al., 2000b). When viewed through time, coastal erosion is effectively instantaneous as land irreversibly becomes water. In contrast, the process of subsidence can occur anywhere within the delta, including more inland areas. Subsidence, though not always, is often slower than edge erosion and loss may be preceded by more frequent flooding (McKee and Cherry, 2009; Miller et al., 2008; Morgan, 1972; Wells, 1996).

2.2. Material and Methods

2.2.1 Study Area and Datasets

Our study area is the Lower Mississippi River Delta (LMRD), where we investigated watersheds at two different spatial scales (Figure 2.1). Hydrological Unit Codes (HUCs) are designations by the United States Geological Survey (USGS), chosen to maintain consistency in the spatial scale of hydrological analysis. Within the LMRD, four HUC-6 watersheds are composed of 94 smaller HUC-12 watersheds (Figure 2.1), with HUC-12 being the smallest designation assigned by USGS. We used coastal HUC-12 watersheds only while avoiding large urban populations, resulting in modified HUC-6 watersheds being used for the analysis (Figure 2.1). Though anthropogenic processes are realized further downstream, the study was focused on highlighting patterns and process of land loss in a delta system as a whole. The study further focuses on trying to link patterns to underlying natural processes that in conjunction with anthropogenic effects play a detrimental effect on the delta lifecycle further justifying decision to exclude areas with large urban clusters and populations. The modified HUC-6 Boundaries and the selected HUC-12 watersheds within these boundaries are shared as supplemental material.

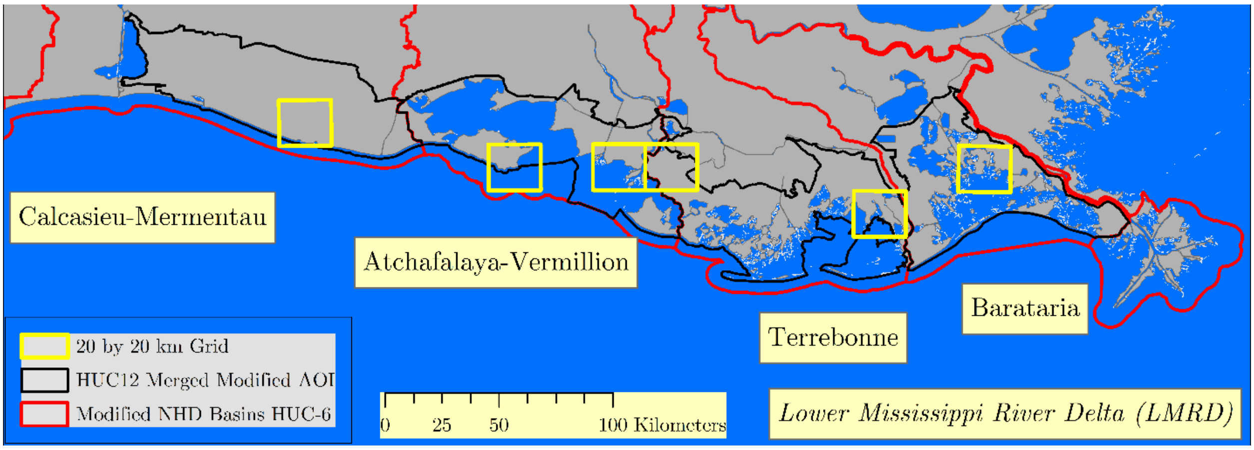

Figure 2.1: Large coastal watersheds (HUC 6 scale) within the LMRD that do not contain large urban areas. Smaller watersheds (HUC-12 scale) also area shown within each (Twilley et al., 2016). Yellow boxes show areas selected for further analysis within the overall basin.

Spatial and temporal consistency for long-term land loss analysis has relied on historical maps and satellite imagery such as that provided by the Landsat continuity missions, which serve as the longest historical and open source satellite dataset in the world. With its 30-meter resolution and 16-day repeat cycle, Landsat products provide a globally consistent spatial and temporal resolution (Hansen et al., 2014; Ju et al., 2012; Li and Roy, 2017; Roy et al., 2010). Given the size of the study area, multiple Landsat scenes were needed for each HUC-12. However, not all Landsat scenes are usable owing to the presence of clouds and cloud shadows which can limit the ability to monitor land (Donchyts et al., 2016a; Hansen et al., 2014; Hansen and Loveland, 2012; Roy et al., 2010). To minimize issues with cloud cover and short-term weather systems, such as hurricanes and storms that rapidly alter land morphology, temporal composite imagery were created from Landsat 5-8 missions (Chander et al., 2009; Chander and Markham, 2003; Donchyts et al., 2016b; Goward and Williams, 1997).

To generate the composite imagery, we evaluated nearly 4800 Landsat tiles with less than 30% cloud cover (Table 2.1). Each multi-year composite image is created from three years of Landsat scenes over the study area. Only TM and ETM+ are used to maintain spatial and spectral consistency (i.e., no MSS data are used). All composites are for three years except the first period (1980 to 1984) since a limited number of images were available (Table 2.1) for our area of interest at the beginning of the period of record.

Table 2.1: Landsat image count for creating image composites with a 30th percentile composite calculated to minimize cloud cover per band. Here Landsat TM (includes Landsat 4 & 5) and Landsat ETM+ (Landsat 7 & 8).

Start Date	End Date	# of Images	Instrument Type
1980-01-01	1984-12-31	56	Landsat TM
1983-01-01	1985-12-31	108	Landsat TM
1986-01-01	1988-12-31	269	Landsat TM

1989-01-01	1991-12-31	240	Landsat TM
1992-01-01	1994-12-31	276	Landsat TM
1995-01-01	1997-12-31	294	Landsat TM
1998-01-01	2000-12-31	503	Landsat TM & Landsat ETM+
2001-01-01	2003-12-31	636	Landsat TM & Landsat ETM+
2004-01-01	2006-12-31	648	Landsat TM & Landsat ETM+
2007-01-01	2009-12-31	606	Landsat TM & Landsat ETM+
2010-01-01	2012-12-31	514	Landsat ETM+
2013-01-01	2015-12-31	648	Landsat ETM+

For each image in our composite, we used orthorectified and calibrated top-of-atmosphere (TOA) reflectance scenes to correct for between-scene variations in solar irradiance, as suggested by (Chander et al., 2013, 2009; Chander and Markham, 2003) and used by many (Donchyts et al., 2016a; Dong et al., 2016; Goldblatt et al., 2016; Hansen and Loveland, 2012; Kuleli et al., 2011; Shelestov et al., 2017). The final step in creating multiyear composites is reducing the stack of images per-band per-pixel for each three-year period into a single image. The three-year period allowed us to remove extreme hydrological events, such as floods or high tides.

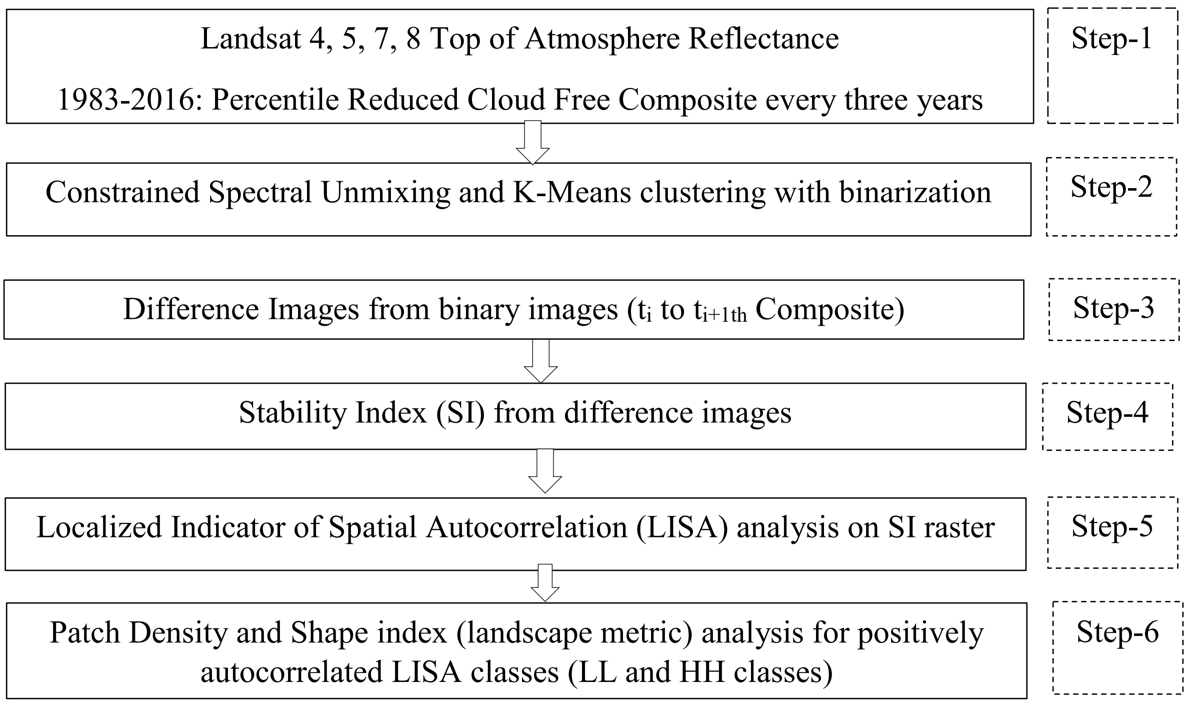

Figure 2.2: Six-step workflow for the overall approach, leading from raw satellite data to landscape metrics in spatially autocorrelated geographic areas.

For each three-year period, we use a percentile reducer on each image within a collection, which uses the reflectance value corresponding to the n^{th} percentile for each pixel (Step 1 in Fig. 2). Percentiles generally perform better than taking a simple average because they are not sensitive to outliers (Bornmann et al., 2013; Donchyts et al., 2016a, 2016b; Pekel et al., 2016) and this method creates robust multiyear cloud-free composites (Donchyts et al., 2016a, 2016b; Pekel et al., 2016). We use the 30^{th} percentile value for each pixel because it performed well during composite creation (along with removing clouds and cloud shadows).

2.2.2 Land-Water Classification: Spectral Unmixing and K-Means clustering

For each three-year composite image, we used spectral unmixing to determine the proportion of land or water in each pixel. As a soft classification technique, spectral unmixing allows for subpixel fractional abundance values of land or water classes for each pixel (Lu and Weng, 2007; Nath et al., 2014). To develop suitable land and water spectra, we collected endmember spectra from areas designated as permanent water and land bodies as designated by earlier global models (Donchyts et al., 2016a; Pekel et al., 2016). We used constrained spectral unmixing to make sure that the percentage of land or water for each pixel summed to one for each three-year composite (Keshava, 2003; Keshava and Mustard, 2002). We describe spectral unmixing using the linear mixing model (LMM) where we have *M* endmembers:

$$x = \sum_{i=1}^{M} a_i s_i + w = Sa + w$$

here x is the L by 1 spectrum vector, and S is the L by M matrix formed by the L endmembers, a is the fractional abundance (M by 1) for which we are solving and w is the L by 1 additive observation noise vector (Keshava and Mustard, 2002). Since the images are temporal composites that are drawn from multiple dates over each three-year window and not a standard calibrated product from a single date, we use an adaptive percentile value composite that chooses a specific value for each pixel for the composite from the time stack.

Hence, though linear spectral unmixing provides a percentage composition of each class and can be used for continuous measurement, a thresholding approach is needed with composites that are drawn from many different time slices (Liu and Yang, 2013; Nichol and Wong, 2007). Unsupervised k-means clustering was applied to the percentage water to generate a single value threshold to binarize land and water. The result was a land-water binary map for each 3-year period that we use to assess spatial patterns of land loss. Also, while validation is possible for single reference imagery, a time series composite provides a unique challenge when comparing to a standard high-resolution image. As such, we perform a validation using existing global datasets such as those, provided by (Donchyts et al., 2016a; Pekel et al., 2016). These global validation datasets themselves are a result of binarization (Donchyts et al., 2016a) and field validation (Pekel et al., 2016) which provides robustness to our overall methodology and to our use of adaptive thresholding which allows for better class separation for matching with these validation datasets. The overall process was assembled as a series of scripts in Google Earth Engine.

2.2.3 Spatial Disturbance and Development of the Stability Index (SI)

In this paper, we introduce the concept of the stability index (SI) and apply it to the land-water binaries. Our stability index is inspired by the ecological theory that shows how ecosystems often iterate towards stability, which can be measured using the relative frequency of a pixel to move between land or water states (Averill et al., 1994; Loreau et al., 2003; Marleau et al., 2014). Our SI is based on the observation that not all pixels undergo a single change from land to water, with some pixels transitioning multiple times between land and water. For every pixel ultimately classified as a permanent loss, we calculate the number of transitions that that pixel undergoes. Difference images are created by subtracting Composite_t-Composite_{t+1} (where t is a specific composite in our time series data and t+1 is the next composite) which captures the transition of a pixel from land to water or vice versa.

These transitions are used to calculate SI which assigns a measure of the stability to land-loss pixels:

$$\text{SI}=\frac{\text{K}}{\begin{cases}\frac{n}{2}\ if\ n\ is\ even\\ \frac{n+1}{2}\ if\ n\ is\ odd\end{cases}}\ \text{for } K>0\ ,$$

where K is the number of times a pixel changes from land to water and n is the number of difference images (here, n=11 as we have 12 three-year composites). We posit SI is a measure of the inherent stability of a land pixel and its tendency to undergo transitions between land and water (i.e., its resistance to permanent change from land to water). Therefore, a pixel with a high SI is one that has multiple transitions from land to water (i.e., it is stable in that it is able to resist the transition), and pixels with low SI have a single transition from land to water. The value of K relative to the number of difference images provides a range of SI values with a maximum value of one which would mean the pixel oscillates between land and water in every single time step. In this application, SI values are not calculated for K=0 because this represents a pixel that has remained either land or water throughout the entire period of the study. It is important to note that SI does not quantify land to water transitions resulting from tidal or river flooding since these are events with small temporal footprints that we filter out during the process of creating the multiyear composites. Because our composites are every three years, a transition from land to water represents a fundamental shift to a different state (from land to water or water to land) across the three-year composites. This suggests to us that the transition reflects a longer-term change in the local environment of the pixel.

2.2.4 Spatio-Temporal Autocorrelation

Calculation of the stability index per pixel through time collapses the temporal differences between the land and water binaries from multiple time steps into a single image with a measure of inherent stability. Land loss across the landscape, however, can be thought of as a spatially autocorrelated process. Moran's *I* (Lam et al., 2018; Nagendra et al., 2004) is often used to measure the degree of spatial autocorrelation; however, Moran's *I* is a global measure that provides just one value for the entire landscape. Moran's *I* is further limited by the stationarity assumption that the statistical properties of the variable of interest do not change across the landscape (Cliff and Ord, 1970; Fotheringham, 2009; Griffith, 2006, 1992; Ord and Getis, 2001), which is frequently not the case. As a result, we used a Local Indicator of Spatial Autocorrelation (LISA) to better understand interactions at the relevant scale of the land-to-water conversion processes:

$$I_i = SI_i \sum_j w_{ij} \, SI_j$$

where I_i is the LISA index for pixel i,SI_i and SI_j are the stability indices for pixel i or j in a standardized form, and w_{ij} is the spatial weight (here, we used inverse-distance weighting with Euclidean distances), with the summation across all other j pixels ($i \neq j$).

The LISA analysis generates an index of how similar the SI value for a pixel is relative to its neighbors (Anselin, 1995; Ord and Getis, 1995; Wulder and Boots, 1998). For each pixel's I, 95% confidence intervals allow us to evaluate the statistical significance of local spatial autocorrelation. Each pixel could then be identified as tending towards being similar or different from its neighbors. For instance, High-High (HH) and Low-Low (LL) refers to statistically significant autocorrelation where a pixel has similarly high or low SI values to its neighbors (i.e., positive autocorrelation between themselves and their neighborhood pixels). This refers to areas where pixels with a high and low value of stability are spatially clustered. Similarly, dispersed spatial arrangements were also identified where a high SI value was surrounded by low values (HL) or a low SI value pixel was surrounded by high SI value pixels (LH). In many applications, these dispersed arrangements that have negative spatial autocorrelation are of less interest owing to the low percentage of pixels in these classes and their complex spatial origin (Griffith, 2006, 1992; Wulder and Boots, 1998).

The percentage area lost in each of the LISA class was calculated for all HUC-12 watersheds while considering the dominant LISA class for positive autocorrelation. The percentage value was then plotted for each HUC-12 watershed in relation to landscape metrics that were subsequently calculated.

2.2.5 Landscape metrics: Spatial Configuration and Morphology

Landscape metrics have arisen as a method to quantify spatial heterogeneity and help to explain the relationship between process and patterns (Turner, 1989; Turner et al., 2001). Landscape patches within the LISA derived cluster types (as provided by positive and negative autocorrelations) served as landscape classes for the study. These determine the spatial distribution of pixels with high and low stability and their analysis using landscape metrics is used to measure their distribution. We use Fragstats (v 4.2.1, developed by the Forest Science Department, Oregon State University) to quantify the configuration and morphology of landscape patch stability over space and time. We focus on landscape metrics that provide a measure of shape, size, and structure (Lin et al., 2015; Nagendra et al., 2004; Turner, 1989; Turner et al., 2001, 1993; Turner and Rao, 1990; Uuemaa et al., 2009). We calculate these metrics on each spatio-temporal cluster derived from the LISA. We chose landscape metrics (Table 2.2) that quantify the degree of fragmentation (patch density) and the shape of land loss (shape index). This choice was also informed by studies where factor analysis was performed across a few of these metrics to identify landscape metrics that are strongly correlated (Riitters et al., 1995). Each metric was calculated using a no sampling approach applied to the LISA classes. Landscape metrics were selected (Table 2.2) keeping in mind the finest resolution of the spatial unit (HUC-12) and the spatial resolution of the imagery since spatial units and the spatial resolution impact the metric values and interpretation (Lin et al., 2015; Nagendra et al., 2004; Turner et al., 2001, 1993; Turner and Rao, 1990; Uuemaa et al., 2009).

Table 2.2: Explanation of landscape metrics used: Patch Density and Shape Index.

Metric	Formula	Description & use
Patch Density (PD)	$PD = \frac{NP}{A}$ NP=Number of Patches A= area(m^2) PD is always > 0 but constrained by cell size.	Higher PD values indicate a greater number of patches within the same area. PD is an indicator of fragmentation.
Shape index	$Shape\ index = \frac{0.25\ p_{ij}}{\sqrt{a_{ij}}}$ p_{ij} = perimeter of patch ij (m) a_{ij} = square root of patch area (m^2) adjusted by a constant to adjust for a square standard	Shape index ranges from 1 to infinity. Shape index =1 represents square patches and at higher values, patches become more irregular.

For both HH and LL LISA classes, we calculated the percentage area lost, which describes the area lost in each HUC-12 watershed relative to all area lost in that watershed. We then used this percent area lost metric to test how land loss varied by landscape metric across the HUC-6 watersheds. This was done using two separate linear regression models for HH and LL classes. In the two models, the percent area is the response variable, and the two landscape metrics (PD and Shape) are continuous predictors while the HUC-6 watershed is a categorical predictor variable. Individual t-statistics for each variable, as well as the F-statistic and adjusted r^2 for the full model, are reported as metrics of the goodness of fit. PD and Shape were log-transformed to meet assumptions of normality.

2.3. Results

2.3.1 Permanent Land Loss

We define permanent land loss as any pixel that transitions from land to water and remains water for at atleast the last two time periods of our study. Our analyses showed that, of all the permanent land-loss pixels, 75% undergo a single transition from land to water, while 21% of the pixels undergo two transitions from land to water and the remaining 4% of the pixels undergo three or more transitions from land to water and back. (Table 2.3).

Table 2.3: Percentage of pixels undergoing transitions for the overall area and within HUC-6 watersheds.

	Percentage of Pixels Undergoing Transition				
# of Transitions	Overall	Atchafalaya-Vermillion	Barataria	Calcasieu-Mermentau	Terrebonne
1	75.08	67.90	75.81	81.20	68.99
2	20.99	27.44	20.20	16.50	24.45
3	3.59	4.20	3.49	2.24	5.87
4	0.30	0.46	0.47	0.06	0.67
5	0.008	0.00	0.02	0.00	0.02

In total, the permanent land loss from 1983-2016 was 1403.85 km^2 (Figure 2.3, Figure 2.4). The permanent loss includes those land pixels that transition from land to water at any given three year time period of 1983 to 2016 and remain water pixels for the last two periods of our observation (2010-2016).

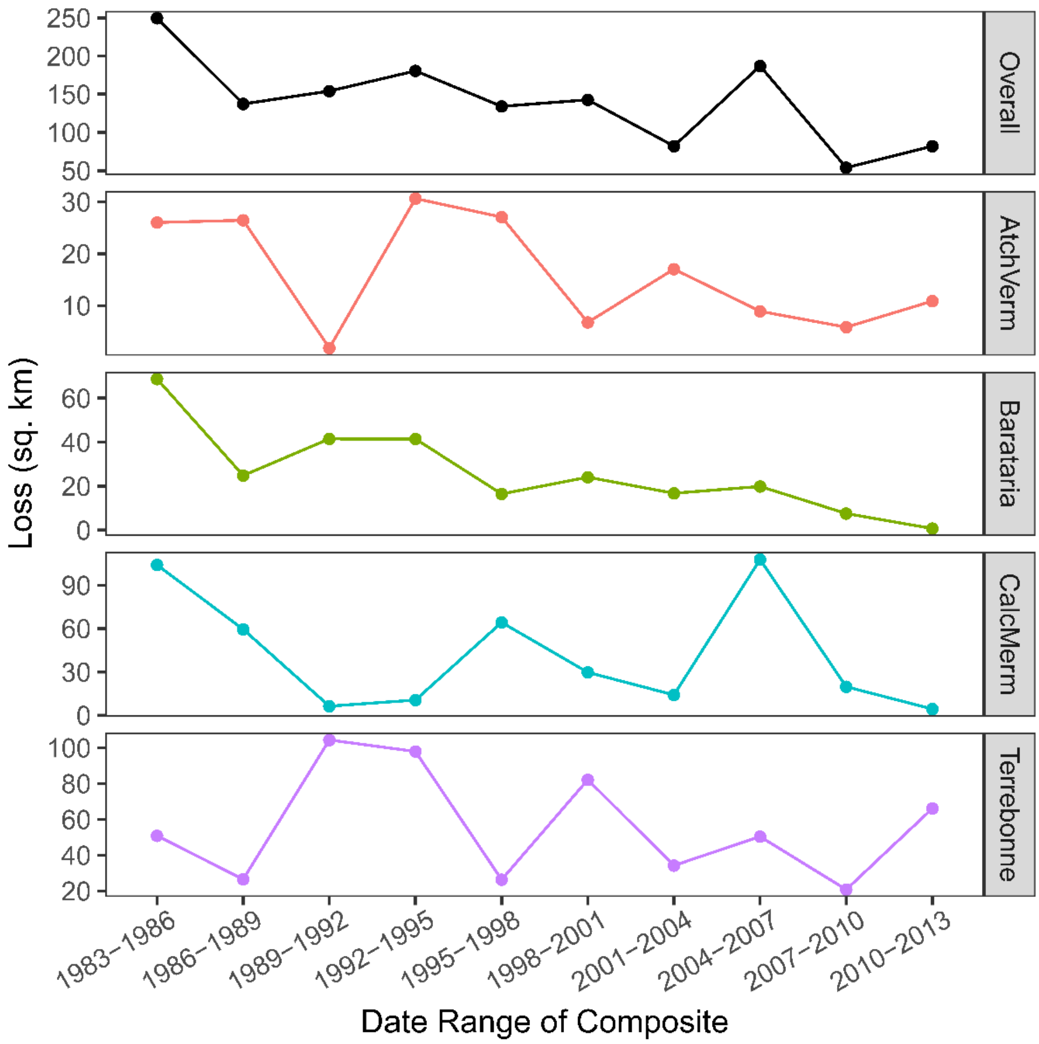

Figure 2.3. Time series of permanent land loss, which refers to land that is lost in each time step and remains as a water class for the last two time steps (2010-13 and 2013-2016). Since the 2013-2016 composite falls within the range determining permanent loss, it is not included in the figure.

Sudden and unusually high increases in the land loss that occurred in 2004-2007 can be attributed to events such as hurricanes Katrina and Rita (Barras, 2007). Though the impacts of single-year events and stochastic flooding are minimized by our methods, these events have a long lasting effect that is captured in the 3-year image composites that we generated for our study. Besides those events, the land loss is relatively steady across the overall study area and the Barataria and Calcasieu-Mermentau (hereafter CalcMerm) watersheds, but more variable through time in Terrebonne and Atchafalaya-Vermilion (hereafter AtchVerm; Figure 2.3).

2.3.2 Spatial Clustering

We found that behavior of land pixels undergoing land loss is spread across undergoing multiple transitions (high SI value) and single transitions (low SI value) (Table 2.3; Figure 2.7). The LISA analysis shows that most LL classes are either along shorelines or lake edges, as well as among fragmented land-water boundaries (Figure 2.4). HH pixels tend to be more inland, away from the coastal edge. Since the landscape is highly fragmented in some areas, there are some isolated low and high values of SI that lead to the LH and HL class distribution (Figure 2.4).

At the basin scale, CalcMerm and Barataria have the highest proportion of area lost in the LL class (Figure 2.5a), closely followed by Terrebonne, while AtchVerm had the lowest amount of land loss. Most pixels are either in the HH or LL class, so the area lost in the HH class is inversely related to that in the LL class, with LL being dominant in most HUC-12 watersheds. We find a higher proportion of area lost that is HH class (Figure 2.5b) in AtchVerm and Terrebonne while Barataria and Calcmerm have lower proportions.

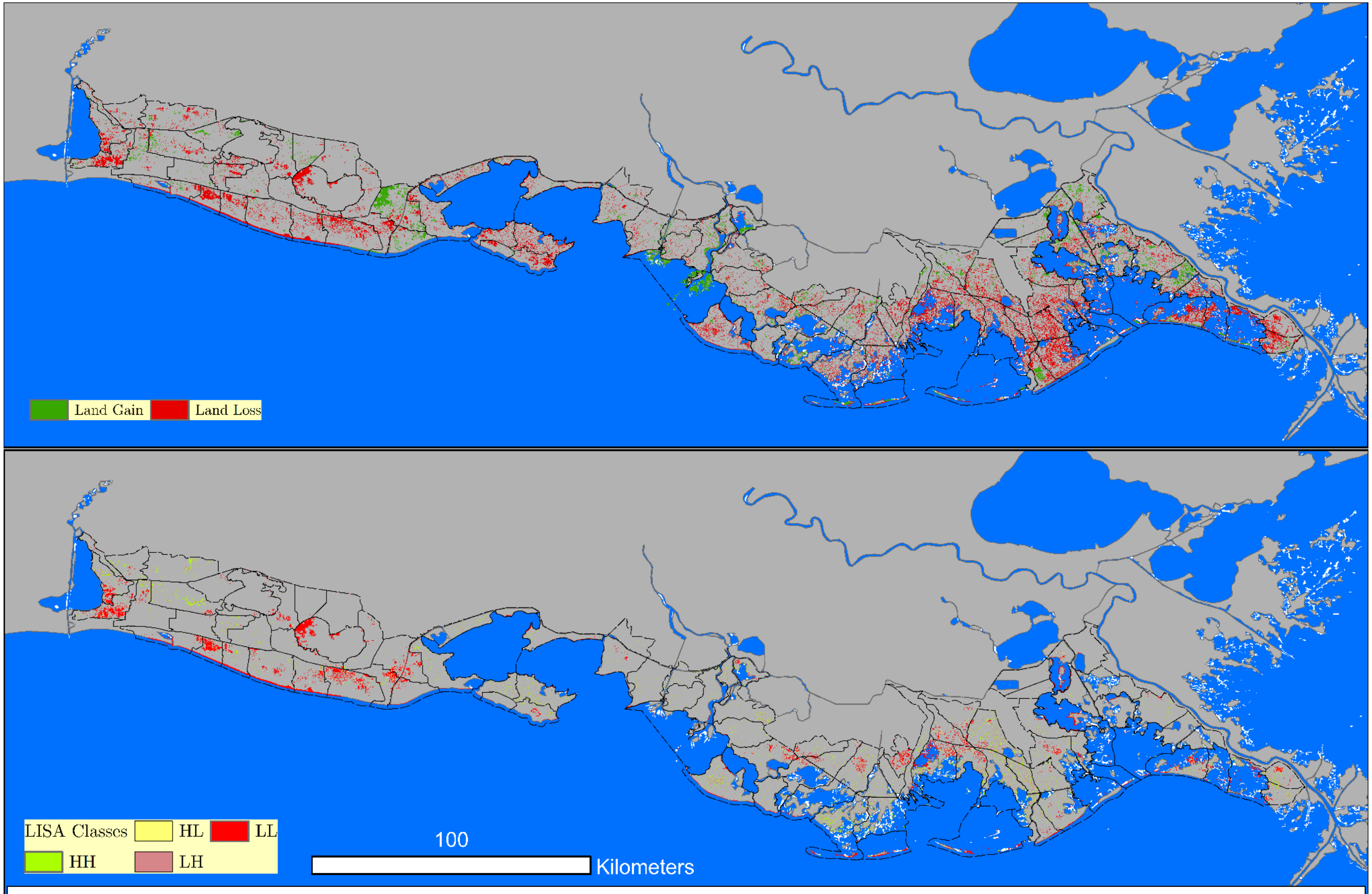

Figure 2.4: Top: Overall Land loss and Land Gain from 1983-2016 and Bottom: LISA classes derived from SI.

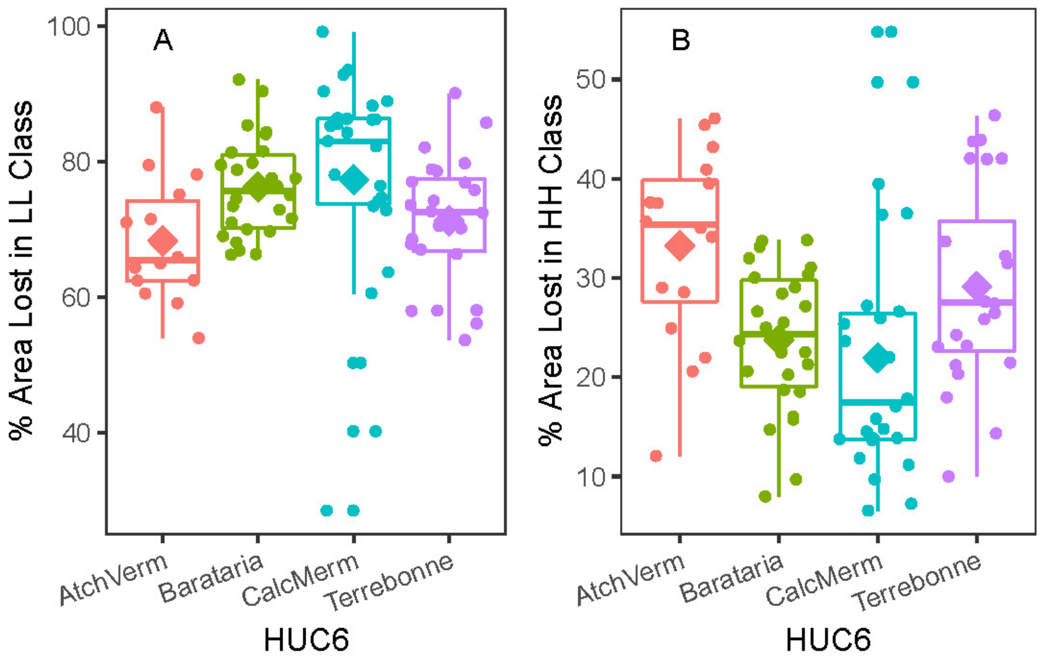

Figure 2.5. Box plot of percentage area lost belonging to A) LL LISA Class and B) HH LISA class for each HUC-12 watershed within the four HUC-6 boundaries. Each circular point represents a single HUC-12 watershed and points are staggered along the x-axis for better viewing. The diamond represents the mean value of the distribution

To understand how land loss (Figure 2.6) and LISA classes (Figure 2.7) are related, we examined six smaller subsets in detail. These subsets were selected using a grid size of 20 by 20 square kilometers to represent land loss across all four HUC-6 watersheds, a varying degree of transitions, and the different LISA classes.

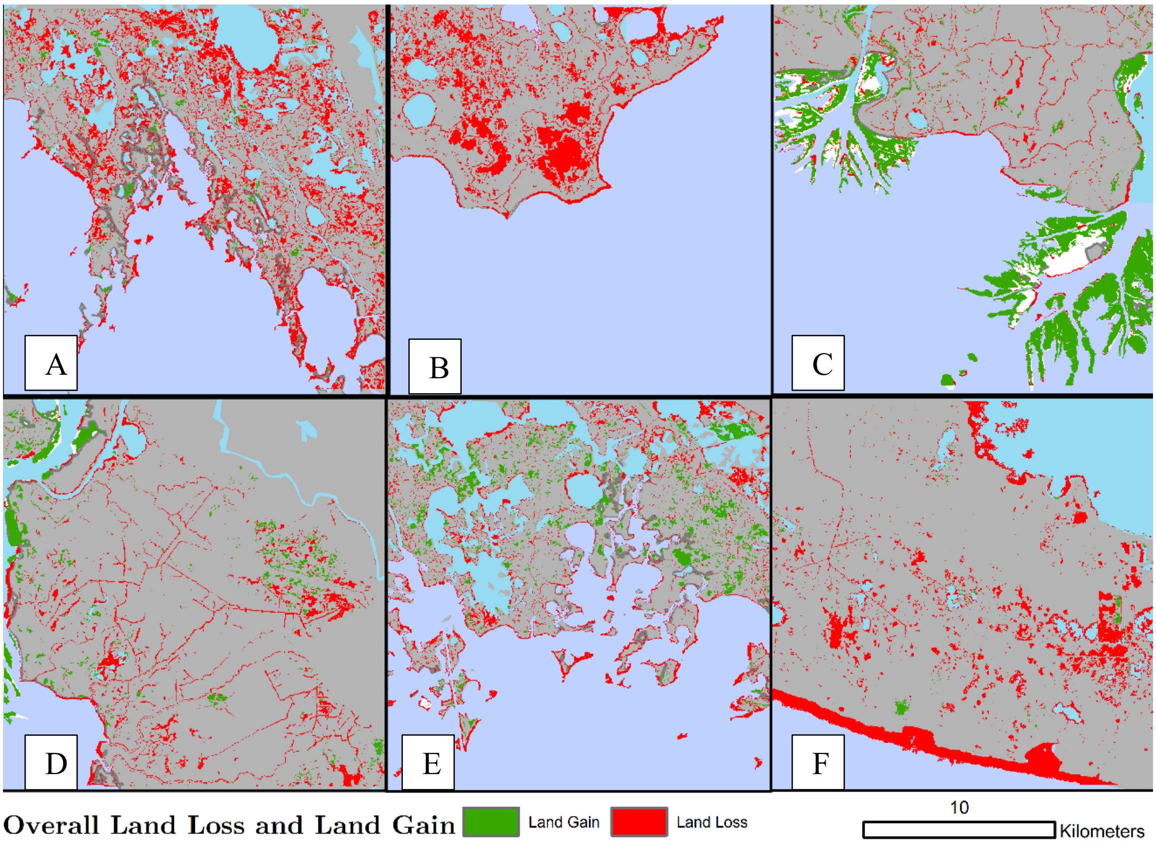

Figure 2.6. Subareas of the LMRD are shown (20 by 20 km^2) to depict representative patterns of land loss between 1983 and 2016 only. Red indicates land loss; green indicates land formation. Panel A & D lies in Terrebonne, Panels B, C lie within Atchverm, Panel E lies in Barataria and Panel F lies in Calcmerm. Gray areas represent land boundaries, light blue represents inland perineal water and dark blue designates world ocean and sea boundaries, and white shading indicates an area where past data does not accurately specify land and water boundaries.

The pixels that experience single transitions tend to be located across coastal and lake edges (Panel B & C of Figure 2.7). Calcmerm shows coastal areas with low SI values (Panel F of Figure 2.7), and most pixels have one transition from land to water. Barataria shows areas lower SI values (Panel E of Figure 2.7) distributed across internal lakes and coastal edges.

Terrebonne low SI along edges (Panel A of Figure 2.7) and higher SI values are located more inland (Panel D of Figure 2.7).

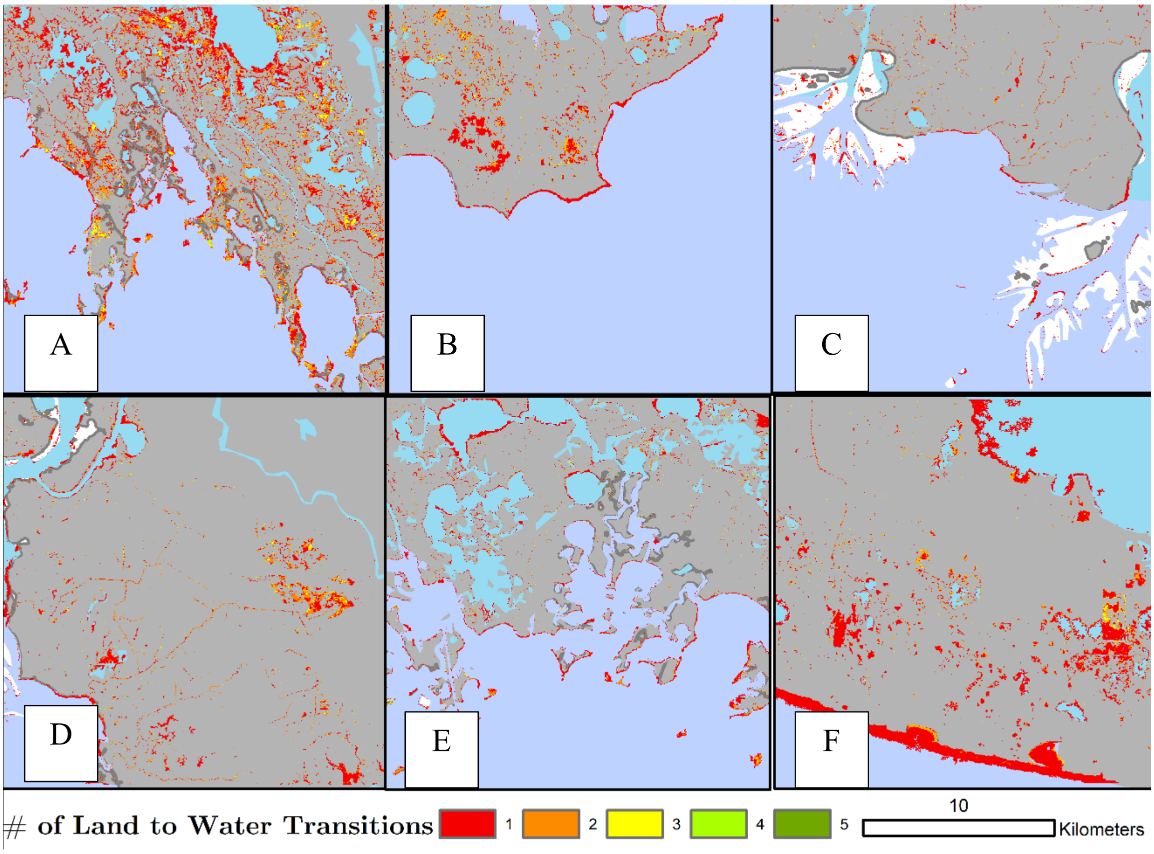

Figure 2.7: Subareas of the LMRD are shown (20 by 20 km^2) to depict the number of land to water transitions. Panel A & D lies in Terrebonne, Panels B, C lie within Atchverm, Panel E lies in Barataria and Panel F lies in Calcmerm. The larger the number of transitions, the higher the stability index. Gray areas represent land boundaries, light blue represents inland perineal water and dark blue designates world ocean and sea boundaries, and white shading indicates an area where past data does not accurately specify land and water boundaries.

Unlike the other sub-watersheds, many locations in Terrebonne have LISA classes that have a mix of single and multiple transitions and varying SI values along with a substantial amount of HL and LH classes (Panel A and D of Figure 2.8). For AtchVerm, we find LL clusters along coastal edges interspersed some LL patches with HH clusters inland (Panel B, C of Figure 2.8). Calcmerm has LL clusters along coastal and lake edges, and HH classes were clustered more inland (Panel F of Figure 2.8), and Barataria shows areas with permanent loss and lower SI values (Panel E of Figure 2.8) distributed across internal lakes and coastal edges.

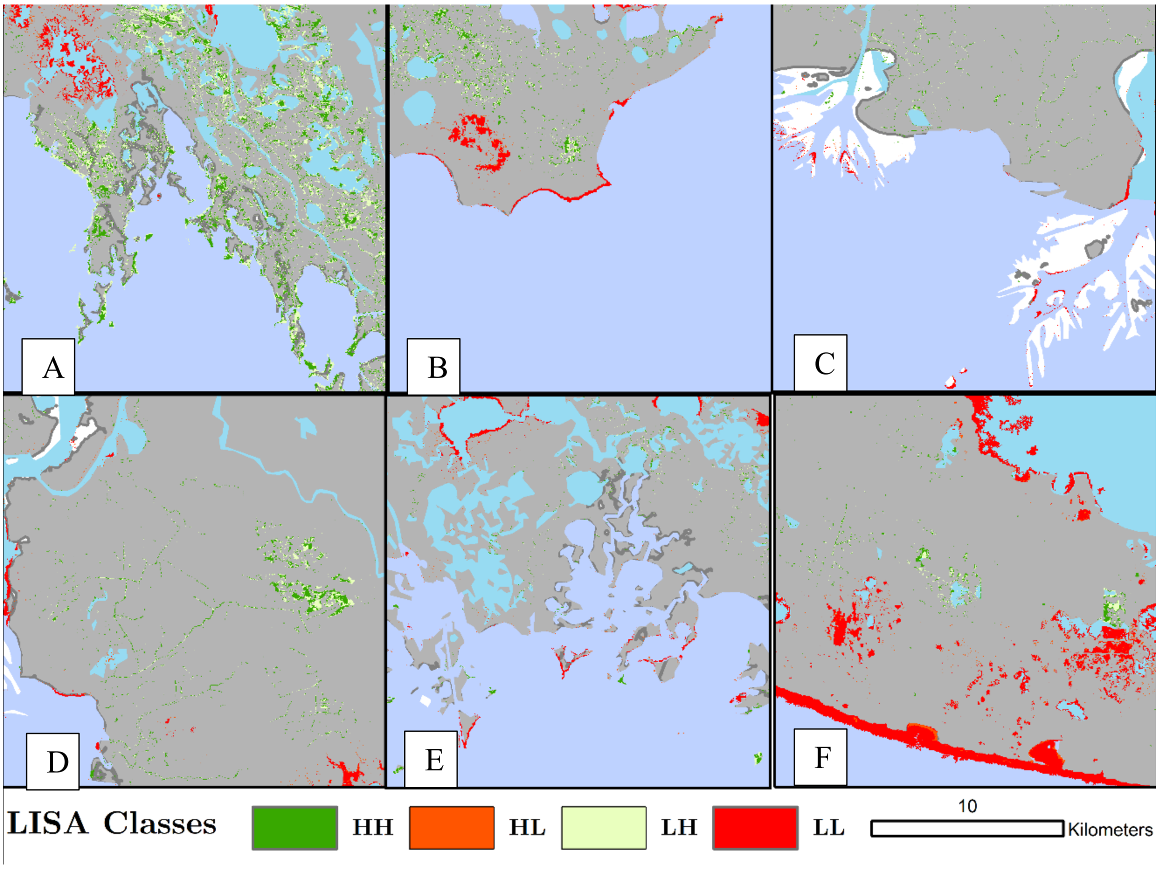

Figure 2.8: Subareas of the LMRD are shown (20 by 20 km^2) to depict cluster types, generated using the Local Indicator of Spatial Autocorrelation. The High-High (HH) and Low-Low (LL) values indicate positive autocorrelation versus HL and LH indicate spatial dispersion. Gray areas represent land boundaries, light blue represents inland perineal water and dark blue designates world ocean and sea boundaries, and white shading indicates an area where past data does not accurately specify land and water boundaries.

2.3.3 Land-loss Morphology

If we examine the morphology of each HH and LL LISA class, we find that the LL class tends to be clumped (low Patch Density value) while the areas in the HH class is more fragmented (high Patch Density value) (Figure 2.9A). HH has lower Shape Index values owing to large fragmented patches in the HH class (higher patch density), with many of the patches being individual pixels.

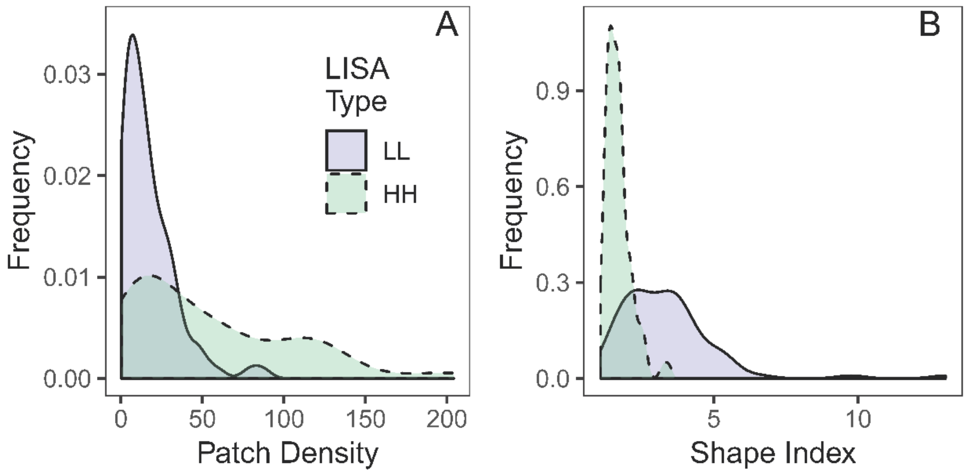

Figure 2.9: Kernel density estimates of the distribution of (A) Patch Density for LL and HH type land loss classes and (B) Shape Index for LL and HH type land loss classes. The spatial metrics were calculated for HUC 12 watershed level.

The relationship between patch density and land fragmentation is key in examining landscape patterns that directly affect land loss (Lam et al., 2018; Rutledge, 2003; Turner and Rao, 1990). Shape index determines the complexity of the underlying morphology created as a result of such fragmentation. This relationship between land loss and landscape metrics was analyzed using a multiple regression model between percentage area lost in LL & HH LISA classes and log-transformed variables landscape metrics (Patch Density and Shape Index). HUC 6 is a categorical variable; the model suggests that while land loss is related to shape and patch density, it is not significantly related to the location/site of the analysis.

Table 2.4: Multiple regression model results across HUC-12 watersheds using the land loss in low-low and high-high class as response variables. Log-transformed Patch Density and Shape Index are used as continuous predictors while HUC 6 watersheds act as categorical variables. Also contains the overall Adjusted R-squared, F-statistics, and p-value for both land loss in low-low and high-high class multiple regression model.

LISA Class	Model Terms	Estimate (±SE)	t-value	P-value
Low-Low Class (n = 95)	Intercept	47.98(±3.27)	14.65	<0.0001
	Patch Density	6.41(±0.76)	8.44	<0.0001
	Shape	7.63(±1.96)	3.89	0.0002
Adjusted R-Squared = 0.545	HUC6-Barataria	3.99(±2.73)	1.459	0.148
Overall F-statistic = 22.58	HUC6-Calcmerm	3.99(±2.73)	1.289	0.201
	HUC6-Terrebonne	3.99(±2.73)	0.859	0.392
Overall P-value <0.0001				
High-High Class (n = 95)	Intercept	-2.20(±2.98)	-0.742	0.460
	Patch Density	6.78(±0.54)	12.655	<0.0001
	Shape	13.25(±2.68)	4.937	<0.0001
Adjusted R-Squared = 0.716	HUC6-Barataria	-3.17(±1.90)	-1.674	0.097
	HUC6-Calcmerm	-1.13(±2.10)	-0.536	0.593
Overall F-statistic = 47.06	HUC6-Terrebonne	0.38(±1.91)	0.198	0.843
Overall P-value <0.0001				

We observe a strong positive relationship between land loss and both PD and Shape, for both LL and HH based land loss. Interestingly, this is not sensitive to whether the loss undergoes single or multiple transitions because a positive relationship is observed for both LL and HH classes across the HUC 12 watersheds (Table 2.4,).

2.4. Discussion and Conclusions

This study examines the overall land loss in the Lower Mississippi River Delta (LMRD) from 1984 to 2016 using Landsat data. The purpose of this study was twofold: to highlight the complexities inherent in robustly estimating land loss and to provide a means of combining spatial and temporal dimensions of loss using SI. The paper introduces the concept of SI to establish land-water transitions that occur in a natural pixel, before converting to permanent water, which in our paper is referred to as permanent loss. By studying land loss that undergoes multiple transitions, relative to a single transition, we may identify important clues about the underlying processes driving land loss in delta environments. Our results are the first to demonstrate that though most land to water transitions occur as a single transition event (~75%), over 25 % of the overall land area goes through two or more transitions between land and water before a permanent loss.

SI further elucidates the dynamic nature of deltaic systems as compared to loss models in other systems, such as studies on global forest loss (Hansen et al., 2013). With forest loss to gain at about 34% or study about the global permanent water area where the net gain of permanent water is twice as much as net loss (Pekel et al., 2016). As the number of oscillations between land and water for each pixel increases and reach an extreme value, the pixels undergoing these oscillations dramatically decreases. AtchVerm and CalcMerm represent areas where the land loss is clustered around coastal and lake edges. By contrast, in Barataria, we find a mix between areas undergoing loss and gain interspersed amongst one another, and in Terrebonne, we find areas with distributed losses including loss along man-made canals and fragmented coastal edges.

Interestingly, our results show that different LISA classes are often clustered and have different shapes and functional characteristics. We hypothesize that the LL and HH LISA represent different processes that are driving land loss. For instance, the LL patches tend to have a low density and an elongated shape (Figure 2.10); moreover, many of these patches are preferentially found on coastal and lake boundaries (Figure 2.4 and 9). Based on this pattern, and also the fact that most of these pixels undergo only a single transition from land to water, we posit that they are primarily caused by wave-edge erosion (Coleman, 1988; Day et al., 2000; Ortiz et al., 2017). Though, it is important to note that LL patches located away from edges (see interior pixels in Figure 2.9F) are not likely to be driven by wave-edge erosion.

Consequently, the opposite is true for HH patches. The HH patches tend to have a high patch density, meaning that they tend to have more patches per unit area and are less concentrated. As a result of the high patch density, the shape index of each cluster is much lower (Figure 2.10), indicating they have a geometrical shape such as a square-like shape and sometimes even represent just a single or limited number of isolated land pixels. If our interpretation of the LISA classes is accurate in terms of the processes associated with them, it would suggest that roughly 75% of land loss on the LMRD is driven by wave edge erosion and other processes that create single transition pixels. This stands in contrast to the recent analysis by (Jankowski et al., 2017), who show using the coastwide reference monitoring station (CRMS) that shallow subsidence is the primary driver of loss. Most of the CRMS data come from interior pixels, and for obvious reason, those stations are not placed on marsh edges. We suspect that the CRMS data oversample the interior parts of islands where subsidence can act.

It is important to note that the processes of edge-erosion and subsidence do not act in isolation. For both the LL and HH patches, we see that land loss increases as land becomes more fragmented, which is measured by the multiple regression models for both LL and HH patches (Table 2.4). This could arise as subsidence or edge-erosion, which further increases edge-length, thus providing more opportunities for erosion. The combination of these processes can a positive feedback loop and accelerate land loss (Lam et al., 2018; Nagendra et al., 2004). In particular, for those clusters that have undergone more than a single transition, flooding due to subsidence could cause edge erosion and ultimately lead to permanent loss.

By studying the positively autocorrelated LISA classes, we were able to yield insights into the evolution of the delta environment more generally, and further show how LISA classes themselves may transition from one type to another as the landscape fragments. The use of both functional and spatial landscape metrics in the linear model provides evidence of a positive feedback loop between fragmentation and land loss. Delta processes such as subsidence, ponding, and sediment deposition change the landscape morphology and can then be interpreted using these landscape metrics as process proxies. For example, previous studies in coastal areas have linked PD to patch isolation and ultimately land fragmentation, by identifying overall increases in marsh edges for wind and wave actions to have a detrimental effect (Kindlmann and Burel, 2008; Ortiz et al., 2017; Turner and Rao, 1990). In the LMRD, an example of this pattern would be the fact that newly formed small ponds often merge with larger ponds and increase land fragmentation, while simultaneously growing pond area via edge erosion and an increase in wind fetch (Ortiz et al., 2017).

We find that core area which refers to core area in the patch, at a distance from the edge decreases (Haines-Young and Chopping, 1996; Luck and Wu, 2002; Neel et al., 2004; Tischendorf, 2001). As core area fragments further edges get exposed to wave and wind action further accelerating fragmentation. We posit that the high values of patch density and shape index, which represents a fragmented landscape with more edges might allow for multiple process regimes to deteriorate land. The paper demonstrates that land loss as a spatio-temporal process can be quantified using SI, which allows for understanding spatial and temporal trajectories of each pixel.

2.5. Conclusions

Deltas around the world are highly vulnerable, but predictive models of land loss are challenging to develop because of oscillations between land loss and land gain. Our study provides a new spatio-temporal model to quantify the land loss and also highlights the underlying processes driving patterns of land loss in the LMRD. While future work will have to determine if the LL and HH classes in this study are caused by subsidence or edge erosion, our results hold promise for using remote sensing to determine processes of land loss. Determining the process driving land loss is essential for effective restoration of coastline, and not all coasts have the data infrastructure of the LMRD where causes of land loss can be directly measured. Future studies should use higher spatial and temporal resolution datasets to further our understanding of these processes at the fine scales and potentially identify smaller patches for increased study and management.

Through this work, we have chosen to focus on a single region, the LMRD. However, the approaches used here should be readily transferable to other delta systems across the globe. Only with an increased understanding of the diversity of ways that land is lost through time can we begin to build more predictive models for future climate change. Such an approach will allow land managers to prioritize areas with the most rapid loss to implement protection and restoration measures affecting multiple deltaic environments.

References

Anselin, L., 1995. Local indicators of spatial association—LISA. Geographical analysis 27, 93–115.

Austin, D.E., 2006. Coastal exploitation, land loss, and hurricanes: a recipe for disaster. American Anthropologist 108, 671–691.

Averill, R.D., Larson, L., Saveland, J., Wargo, P., Williams, J., Bellinger, M., 1994. Disturbance processes and ecosystem management. Washington, DC: US Department of Agriculture, Forest Service. 19 p.

Barras, J.A., 2007. Satellite images and aerial photographs of the effects of Hurricanes Katrina and Rita on coastal Louisiana. Geological Survey (US).

Bernier, J.C., Morton, R.A., Barras, J.A., 2006. Constraining rates and trends of historical wetland loss, Mississippi River Delta Plain, south-central Louisiana. Coastal Environment and Water Quality. Water Resources Publications, Highlands Ranch, USA. pp371-382.

Blum, M.D., Roberts, H.H., 2012. The Mississippi delta region: past, present, and future. Annual Review of Earth and Planetary Sciences 40, 655–683.

Blum, M.D., Roberts, H.H., 2009. Drowning of the Mississippi Delta due to insufficient sediment supply and global sea-level rise. Nature Geoscience 2, 488–491.

Bornmann, L., Leydesdorff, L., Mutz, R., 2013. The use of percentiles and percentile rank classes in the analysis of bibliometric data: Opportunities and limits. Journal of Informetrics 7, 158–165.

Britsch, L.D., Dunbar, J.B., 1993. Land loss rates: Louisiana coastal plain. Journal of coastal research 324–338.

Chander, G., Hewison, T.J., Fox, N., Wu, X., Xiong, X., Blackwell, W.J., 2013. Overview of intercalibration of satellite instruments. IEEE Transactions on Geoscience and Remote Sensing 51, 1056–1080.

Chander, G., Huang, C., Yang, L., Homer, C., Larson, C., 2009. Developing consistent Landsat data sets for large area applications: The MRLC 2001 protocol. IEEE Geoscience and Remote Sensing Letters 6, 777–781.

Chander, G., Markham, B., 2003. Revised Landsat-5 TM radiometric calibration procedures and postcalibration dynamic ranges. IEEE Transactions on geoscience and remote sensing 41, 2674–2677.

Cliff, A.D., Ord, K., 1970. Spatial autocorrelation: a review of existing and new measures with applications. Economic Geography 46, 269–292.

Coleman, J.M., 1988. Dynamic changes and processes in the Mississippi River delta. Geological Society of America Bulletin 100, 999–1015.

Couvillion, B.R., Barras, J.A., Steyer, G.D., Sleavin, W., Fischer, M., Beck, H., Trahan, N., Griffin, B., Heckman, D., 2011. Land area change in coastal Louisiana from 1932 to 2010.

Couvillion, B.R., Fischer, M.R., Beck, H.J., Sleavin, W.J., 2016. Spatial Configuration Trends in Coastal Louisiana from 1985 to 2010. Wetlands 36, 347–359.

Craig, N.J., Turner, R.E., Day, J.W., 1979. Land loss in coastal Louisiana (USA). Environmental Management 3, 133–144.

Day, J.W., Boesch, D.F., Clairain, E.J., Kemp, G.P., Laska, S.B., Mitsch, W.J., Orth, K., Mashriqui, H., Reed, D.J., Shabman, L., 2007. Restoration of the Mississippi Delta: lessons from hurricanes Katrina and Rita. science 315, 1679–1684.

Day, J.W., Britsch, L.D., Hawes, S.R., Shaffer, G.P., Reed, D.J., Cahoon, D., 2000. Pattern and process of land loss in the Mississippi Delta: a spatial and temporal analysis of wetland habitat change. Estuaries and Coasts 23, 425–438.

Donchyts, G., Baart, F., Winsemius, H., Gorelick, N., Kwadijk, J., van de Giesen, N., 2016a. Earth's surface water change over the past 30 years. Nature Climate Change 6, 810.

Donchyts, G., Schellekens, J., Winsemius, H., Eisemann, E., van de Giesen, N., 2016b. A 30 m resolution surface water mask including estimation of positional and thematic differences using landsat 8, srtm and openstreetmap: a case study in the Murray-Darling Basin, Australia. Remote Sensing 8, 386.

Dong, J., Xiao, X., Menarguez, M.A., Zhang, G., Qin, Y., Thau, D., Biradar, C., Moore III, B., 2016. Mapping paddy rice planting area in northeastern Asia with Landsat 8 images, phenology-based algorithm and Google Earth Engine. Remote sensing of environment 185, 142–154.

Ericson, J.P., Vörösmarty, C.J., Dingman, S.L., Ward, L.G., Meybeck, M., 2006. Effective sea-level rise and deltas: causes of change and human dimension implications. Global and Planetary Change 50, 63–82.

Fotheringham, A.S., 2009. "The problem of spatial autocorrelation" and local spatial statistics. Geographical analysis 41, 398–403.

Goldblatt, R., You, W., Hanson, G., Khandelwal, A.K., 2016. Detecting the boundaries of urban areas in India: A dataset for pixel-based image classification in Google Earth Engine. Remote Sensing 8, 634.

Gorelick, N., Hancher, M., Dixon, M., Ilyushchenko, S., Thau, D., Moore, R., 2017. Google Earth Engine: Planetary-scale geospatial analysis for everyone. Remote Sensing of Environment 202, 18–27.

Goward, S.N., Williams, D.L., 1997. Landsat and earth systems science: development of terrestrial monitoring. Photogrammetric engineering and remote sensing 63, 887–900.

Griffith, D.A., 2006. Hidden negative spatial autocorrelation. Journal of Geographical Systems 8, 335–355.

Griffith, D.A., 1992. What is spatial autocorrelation? Reflections on the past 25 years of spatial statistics. L'Espace géographique 265–280.

Haines-Young, R., Chopping, M., 1996. Quantifying landscape structure: a review of landscape indices and their application to forested landscapes. Progress in physical geography 20, 418–445.

Hansen, M.C., Egorov, A., Potapov, P.V., Stehman, S.V., Tyukavina, A., Turubanova, S.A., Roy, D.P., Goetz, S.J., Loveland, T.R., Ju, J., 2014. Monitoring conterminous United States (CONUS) land cover change with web-enabled Landsat data (WELD). Remote sensing of Environment 140, 466–484.

Hansen, M.C., Loveland, T.R., 2012. A review of large area monitoring of land cover change using Landsat data. Remote sensing of Environment 122, 66–74.

Hansen, M.C., Potapov, P.V., Moore, R., Hancher, M., Turubanova, S.A.A., Tyukavina, A., Thau, D., Stehman, S.V., Goetz, S.J., Loveland, T.R., 2013. High-resolution global maps of 21st-century forest cover change. science 342, 850–853.

Houck, O.A., 1983. Land loss in coastal Louisiana: causes, consequences, and remedies. Tul. L. Rev. 58, 3.

Jankowski, K.L., Törnqvist, T.E., Fernandes, A.M., 2017. Vulnerability of Louisiana's coastal wetlands to present-day rates of relative sea-level rise. Nature Communications 8, 14792.

Ju, J., Roy, D.P., Vermote, E., Masek, J., Kovalskyy, V., 2012. Continental-scale validation of MODIS-based and LEDAPS Landsat ETM+ atmospheric correction methods. Remote Sensing of Environment 122, 175–184.

Kesel, R.H., 1989. The role of the Mississippi River in wetland loss in southeastern Louisiana, USA. Environmental Geology and Water Sciences 13, 183–193.

Keshava, N., 2003. A survey of spectral unmixing algorithms. Lincoln laboratory journal 14, 55–78.

Keshava, N., Mustard, J.F., 2002. Spectral unmixing. IEEE signal processing magazine 19, 44–57.

Kindlmann, P., Burel, F., 2008. Connectivity measures: a review. Landscape ecology 23, 879–890.

Kuleli, T., Guneroglu, A., Karsli, F., Dihkan, M., 2011. Automatic detection of shoreline change on coastal Ramsar wetlands of Turkey. Ocean Engineering 38, 1141–1149.

Lam, N.S.-N., Cheng, W., Zou, L., Cai, H., 2018. Effects of landscape fragmentation on land loss. Remote Sensing of Environment 209, 253–262.

Li, J., Roy, D.P., 2017. A Global Analysis of Sentinel-2A, Sentinel-2B and Landsat-8 Data Revisit Intervals and Implications for Terrestrial Monitoring. Remote Sensing 9, 902.

Lin, C., Wu, C.-C., Tsogt, K., Ouyang, Y.-C., Chang, C.-I., 2015. Effects of atmospheric correction and pansharpening on LULC classification accuracy using WorldView-2 imagery. Information Processing in Agriculture 2, 25–36.

Liu, T., Yang, X., 2013. Mapping vegetation in an urban area with stratified classification and multiple endmember spectral mixture analysis. Remote Sensing of Environment 133, 251–264.

Loreau, M., MOuquet, N., Holt, R.D., 2003. Meta-ecosystems: a theoretical framework for a spatial ecosystem ecology. Ecology Letters 6, 673–679.

Lu, D., Weng, Q., 2007. A survey of image classification methods and techniques for improving classification performance. International journal of Remote sensing 28, 823–870.

Luck, M., Wu, J., 2002. A gradient analysis of urban landscape pattern: a case study from the Phoenix metropolitan region, Arizona, USA. Landscape ecology 17, 327–339.

Marleau, J.N., Guichard, F., Loreau, M., 2014. Meta-ecosystem dynamics and functioning on finite spatial networks. Proceedings of the Royal Society B: Biological Sciences 281, 20132094.

McKee, K.L., Cherry, J.A., 2009. Hurricane Katrina sediment slowed elevation loss in subsiding brackish marshes of the Mississippi River delta. Wetlands 29, 2–15.

Miller, R.L., Fram, M., Fujii, R., Wheeler, G., 2008. Subsidence reversal in a re-established wetland in the Sacramento-San Joaquin Delta, California, USA. San Francisco Estuary and Watershed Science 6.

Morgan, J.P., 1972. Impact of subsidence and erosion on Louisiana coastal marshes and estuaries, in: Proceedings of the Coastal Marsh and Estuary Management Symposium. Division of Continuing Education, Louisiana State University, Baton Rouge, La. pp. 217–233.

Morton, R.A., 2003. An overview of coastal land loss: with emphasis on the Southeastern United States. Citeseer.

Nagendra, H., Munroe, D.K., Southworth, J., 2004. From pattern to process: landscape fragmentation and the analysis of land use/land cover change. Elsevier.

Nath, S.S., Mishra, G., Kar, J., Chakraborty, S., Dey, N., 2014. A survey of image classification methods and techniques, in: Control, Instrumentation, Communication and Computational Technologies (ICCICCT), 2014 International Conference On. IEEE, pp. 554–557.

Neel, M.C., McGarigal, K., Cushman, S.A., 2004. Behavior of class-level landscape metrics across gradients of class aggregation and area. Landscape ecology 19, 435–455.

Newton, A., Carruthers, T.J., Icely, J., 2012. The coastal syndromes and hotspots on the coast. Estuarine, Coastal and Shelf Science 96, 39–47.

Nichol, J., Wong, M.S., 2007. Remote sensing of urban vegetation life form by spectral mixture analysis of high-resolution IKONOS satellite images. International Journal of Remote Sensing 28, 985–1000.

Ord, J.K., Getis, A., 2001. Testing for local spatial autocorrelation in the presence of global autocorrelation. Journal of Regional Science 41, 411–432.

Ord, J.K., Getis, A., 1995. Local spatial autocorrelation statistics: distributional issues and an application. Geographical analysis 27, 286–306.

Ortiz, A.C., Roy, S., Edmonds, D.A., 2017. Land loss by pond expansion on the Mississippi River Delta Plain. Geophysical Research Letters 44, 3635–3642.

Pekel, J.-F., Cottam, A., Gorelick, N., Belward, A.S., 2016. High-resolution mapping of global surface water and its long-term changes. Nature 540, 418.

Penland, S., Wayne, L., Britsch, L.D., Williams, S.J., Beall, A.D., Butterworth, V.C., 2000a. Process classification of coastal land loss between 1932 and 1990 in the Mississippi River delta plain, southeastern Louisiana.

Penland, S., Wayne, L., Britsch, L.D., Williams, S.J., Beall, A.D., Butterworth, V.C., 2000b. Geomorphic classification of coastal land loss between 1932 and 1990 in the Mississippi River Delta Plain, Southeastern Louisiana.

Renaud, F.G., Kuenzer, C., 2012. The Mekong Delta system: Interdisciplinary analyses of a river delta. Springer Science & Business Media.

Riitters, K.H., O'neill, R.V., Hunsaker, C.T., Wickham, J.D., Yankee, D.H., Timmins, S.P., Jones, K.B., Jackson, B.L., 1995. A factor analysis of landscape pattern and structure metrics. Landscape ecology 10, 23–39.

Roy, D.P., Ju, J., Kline, K., Scaramuzza, P.L., Kovalskyy, V., Hansen, M., Loveland, T.R., Vermote, E., Zhang, C., 2010. Web-enabled Landsat Data (WELD): Landsat ETM+ composited mosaics of the conterminous United States. Remote Sensing of Environment 114, 35–49.

Rutledge, D.T., 2003. Landscape indices as measures of the effects of fragmentation: can pattern reflect process?

Shelestov, A., Lavreniuk, M., Kussul, N., Novikov, A., Skakun, S., 2017. Exploring Google Earth Engine platform for big data processing: classification of multi-temporal satellite imagery for crop mapping. Frontiers in Earth Science 5, 17.

Syvitski, J.P., Kettner, A.J., Overeem, I., Hutton, E.W., Hannon, M.T., Brakenridge, G.R., Day, J., Vörösmarty, C., Saito, Y., Giosan, L., 2009. Sinking deltas due to human activities. Nature Geoscience 2, 681–686.

Tessler, Z.D., Vörösmarty, C.J., Grossberg, M., Gladkova, I., Aizenman, H., Syvitski, J.P.M., Foufoula-Georgiou, E., 2015. Profiling risk and sustainability in coastal deltas of the world. Science 349, 638–643.

Tischendorf, L., 2001. Can landscape indices predict ecological processes consistently? Landscape ecology 16, 235–254.

Turner, M.G., 1989. Landscape ecology: the effect of pattern on process. Annual review of ecology and systematics 20, 171–197.

Turner, M.G., Gardner, R.H., O'neill, R.V., 2001. Landscape ecology in theory and practice. Springer.

Turner, M.G., Romme, W.H., Gardner, R.H., O'Neill, R.V., Kratz, T.K., 1993. A revised concept of landscape equilibrium: disturbance and stability on scaled landscapes. Landscape Ecology 8, 213–227.

Turner, R.E., Rao, Y.S., 1990. Relationships between wetland fragmentation and recent hydrologic changes in a deltaic coast. Estuaries and Coasts 13, 272–281.

Twilley, R.R., Bentley, S.J., Chen, Q., Edmonds, D.A., Hagen, S.C., Lam, N.S.-N., Willson, C.S., Xu, K., Braud, D., Peele, R.H., 2016. Co-evolution of wetland landscapes, flooding, and human settlement in the Mississippi River Delta Plain. Sustainability Science 11, 711–731.

Uuemaa, E., Antrop, M., Roosaare, J., Marja, R., Mander, Ü., 2009. Landscape metrics and indices: an overview of their use in landscape research. Living reviews in landscape research 3, 1–28.

Wells, J.T., 1996. Subsidence, sea-level rise, and wetland loss in the lower Mississippi River delta, in: Sea-Level Rise and Coastal Subsidence. Springer, pp. 281–311.

Wulder, M., Boots, B., 1998. Local spatial autocorrelation characteristics of remotely sensed imagery assessed with the Getis statistic. International Journal of Remote Sensing 19, 2223–2231.

Chapter 3

Title: Remotely sensed measurement of land loss and gain in the Lower Mississippi River Delta using Landsat, Sentinel-2, and PlanetScope within the Google Earth Engine

Authors: Samapriya Roy[1*], Tyson L. Swetnam[2], Joseph Mascaro[3], Douglas Edmonds[4]

[1]*Department of Geography, Indiana University, Bloomington, IN, 47405*

[2]*BIO5 Institute, University of Arizona, Tucson, AZ, 85721*

[3]*Planet Labs Inc., San Francisco, CA 94103*

[4]*Department of Earth and Atmospheric Sciences, Indiana University, Bloomington, IN, 47405*

Corresponding Author: *Samapriya Roy, email: roysam@iu.edu*

Abstract

Globally, river delta ecosystems are under threat from changes to riverine sediment load, increased storm surge, and sea-level rise. Loss of land area, human development, and pollution reduce delta ecosystem resilience, further exposing vital civil infrastructure to increased storm damage. To better understand these natural events and human-related threats in deltas, we evaluated multiple Earth Observation Systems (EOS) platforms, leveraging improvements in spatial and temporal resolution over legacy NASA Landsat series imagery, European Space Agency (ESA) Sentinel-2, and finally to the private PlanetScope CubeSat constellation. We use Google Earth Engine (GEE) cyberGIS to compare land area change and ecosystem health at weekly, monthly, and annual intervals. Our approach involves index-based pixel-level classification against constrained spectral unmixing, for sub-pixel classification. GEE allowed comparisons of land loss and fragmentation across the three sensors. We classified land and water classes to estimate land loss. A total of 15,090 images were analyzed across Landsat, Sentinel-2, and PlanetScope sensors, with a total of 180 bi-monthly composites. This approach allowed us to refine land loss estimates by filling in spatiotemporal and spectral windows that better account for inland fragmentation, which accelerates overall land loss in deltas. Results showed declining land areas and increasing fragmentation for both index-based and sub-pixel analysis. Land loss estimates are a function of temporal periods of the imagery, the number of images used for compositing and the resultant benefit of the method used for classification. The improved estimates of land loss identification of at-risk areas elucidated by this study will be used to help protect vulnerable populations, providing indirect savings to local governments through improved mitigation strategy.

Keywords: Delta, composites, Sensor, Landsat, fragmentation

3.1 Introduction

River deltas, where a half billion people live worldwide, are intrinsic to human civilization; they support agriculture, control drinking water quality, and provide coastal defense against storms. Globally, river deltas are increasingly under threat from changes in riverine sediment load (Rabalais et al., 2002; Turner and Rabalais, 1991; Walling, 2008; Walling and Fang, 2003) and increased storm surge and sea-level rise (Syvitski et al., 2009). Deltas are in a constant state of flux, yet we have been limited in our ability to make recurrent observations of their dynamism, owing to the lack of availability of remotely sensed observational data. As a result, the nature of land loss and gain in deltaic systems remains poorly observed, and the underlying causes of change unclear. Time-sensitive observations and finer granularity of data can yield important clues as to the evolution of these landscapes in general, and to the quantitative rate of change from natural and anthropogenic causes narrowly. To better understand these natural events and human-related threats in deltas, we evaluated multiple NASA Earth Observation Systems (EOS) platforms, leveraging improvements in spatial and temporal resolution over legacy Landsat series imagery, to European Space Agency (ESA) Sentinel-2, and finally to the PlanetScope CubeSat constellation.

Satellite-based EOS provide a > 40-year record of global river delta dynamics. However, until recently the availability of legacy satellite datasets limited their use in the detection of long-term patterns; coupled with limited computational resources to handle analysis over large areas, few studies have explored the variability of land loss from inter-annual to the decadal time scale. An important challenge to estimating land loss in coastal environments is pixel classification. This is challenging because most commonly a pixel can consist of more than one thematic class, and this mixed pixel problem is further dependent on spatial resolution, of the sensor and also increasing fragmentation. Soft classification reduces issues of sub-pixel thematic information gathering and the mixed pixel issue and is agnostic of the spatial resolution of the sensor (Atkinson, 2005; Foody, 2004; Zhang et al., 2013)and the image. Our land loss classification method was divided into binarization; based on single class index-based image analysis, the Normalized Difference Water Index (NDWI) (Gao, 1996; Han-Qiu, 2005), and soft image classification technique such as Constrained Spectral Unmixing (Foody, 2004; Heylen and Scheunders, 2011; Keshava, 2003; Keshava and Mustard, 2002; Zhang et al., 2013)

Using EOS data obtained from three different systems, we test the effects of increased temporal frequency data (Figure 3.1), greater spatial granularity and spectral characteristics of each dataset (Figure 3.3) on delta land loss estimates. Specifically, we used NASA Landsat ETM+ 7 & Landsat OLI 8; hereafter referred to as ‘Landsat’, ESA Sentinel-2A and 2B, hereafter referred to as ‘Sentinel-2’, and PlanetScope constellation of over 150 cube satellites to explore delta dynamics at 16-day, 5-day and 1-day temporal observation windows and at 30m, 10m, and 3 m spatial resolution, respectively (Figure 3.3).

Our study seeks to answer two questions: 1) Does increased spatiotemporal resolution data improve delta land-loss and land-gain measurements at an interannual rate? 2) How do soft image classification techniques function to estimate land-loss land-gain? We take an open science approach to our data analysis, including an effort at FAIR (findable, accessible, interoperable, and reusable) data principles (Wilkinson et al., 2016) and contributing to open source repeatable analysis guidelines and tools. By being cloud-based, GEE enables a user to send an algorithm to the dataset rather than creating local copies of the dataset. Using publicly available Landsat and Sentinel-2 collections within GEE the users can reproduce our analysis with GEE JavaScript environment and the Python-based API backend to GEE.

3.2 Methodology

3.2.1 Study Area

We explored deltaic dynamics in six, 20x20 km cells in the Lower Mississippi River Delta (LMRD); the cells represented four larger Hydrologic Unit Code-6 watersheds (USGS designation HUC-6) and were selected to ensure that the full diversity of delta landforms (Figure 3.2) and land loss patterns were present within our analysis. Interannual variability in variables such as sediment flow, sea surface temperature, and tidal effects alter the observed effects that are captured based on the period of observation. While a larger time scale is useful to get rid of biases related to interannual variability effects (Allison, 2012; Bianchi and Allison, 2009; Kolker et al., 2011), these variations yield important information about the underlying process regimes that changes in delta morphology occurring on shorter time scales. Seasonal flooding effects, as well as major events like hurricanes and cyclones (both episodic and periodic), can be captured over smaller interannual time periods (Barras, 2007; Pratolongo et al., 2013; Restrepo and Kettner, 2012; Reyes et al., 2004; Xu and Wu, 2006).

While this fine grain measurement was not possible a couple of years ago, improvements in the temporal frequency of sensors such as Sentinel-2 and PlanetScope varying from 5 days to almost 1 day greatly enhances the number of possible consistent observations across a system.

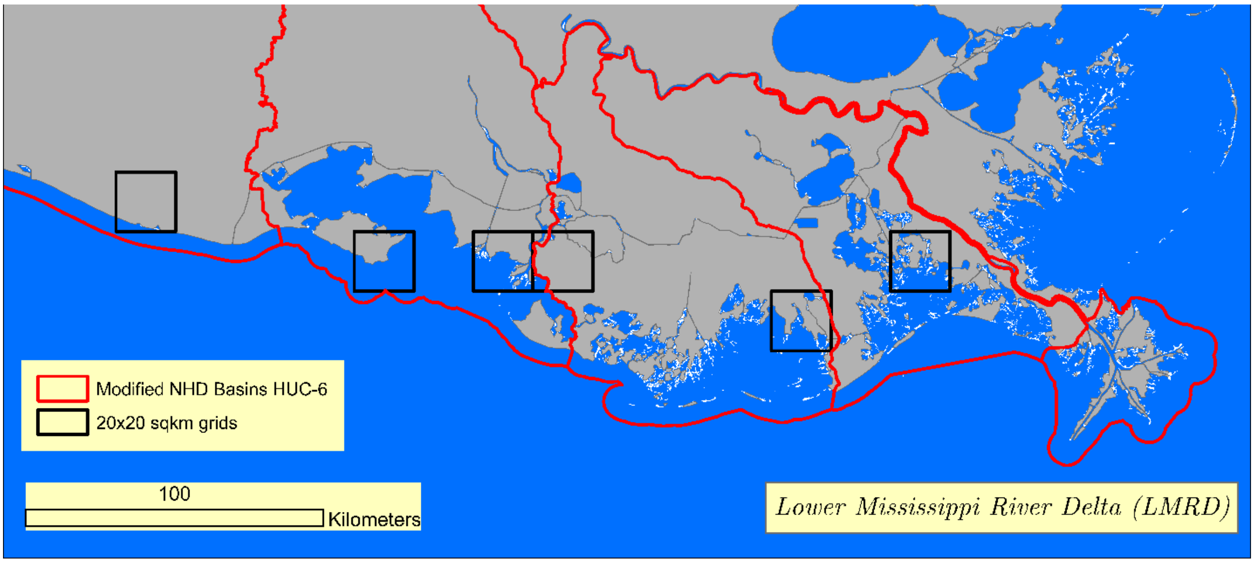

Fig 1. AOI to showing 20x20 km^2 grids within the four HUC-6 watersheds of interest

3.2.2 Earth Observation and Analysis Systems

The growth of subaerial deltaic regions has been observed by satellites since the late 1970s, owing to the first of the NASA Landsat series missions (Rouse et al., 1978; Xia, 1998) along with ground observations that could validate these loss and growth cycles. Earth observation systems (EOS) have changed rapidly in recent years, owing to higher spatial and temporal resolution data from the introduction of cube satellites, faster computation speeds, and increased digital sensor sizes. NASA's Landsat is the longest-serving high-resolution EOS; with a temporal return of 16 days (shortened to 8 days when two or more Landsats are in operation) (Figure 3.2).

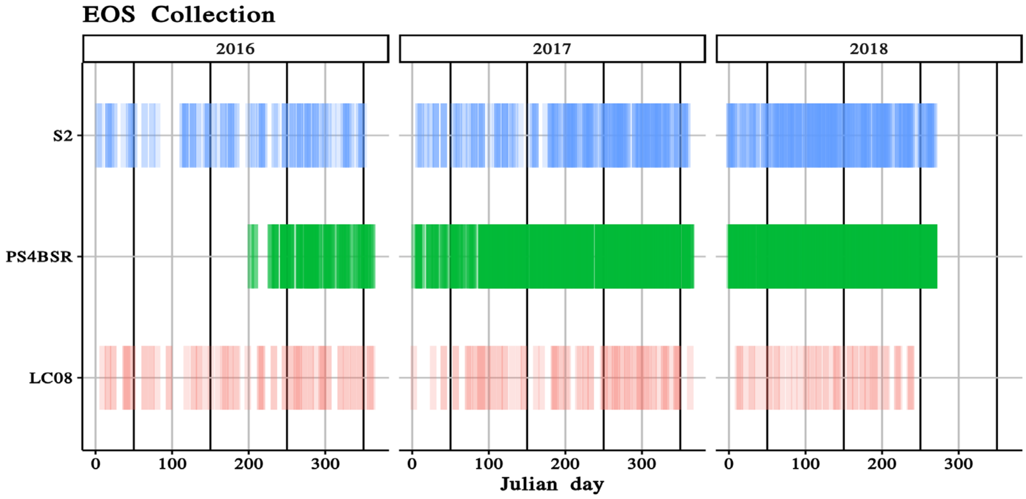

Figure 3.2: Time series of available EOS data for our study area with Sentinel-2 (S2), PlanetScope 4 Band (PS4BSR), and Landsat 8 Collection (LC08). The study period is selected from 2017 onwards to make sure available data covers the entirety of the study period.

Landsat 8 carries the most advanced spectrometers to date, the Operational Land Imager (OLI) and Thermal Infrared Sensor (TIRS). Each Landsat mission has a 16-day interval, with the two current instruments (7 and 8) in an eight-day offset. Since 2003, Landsat 7 results in only partial coverage due to the failure of the scan line corrector (Markham et al., 2004; Scaramuzza and Barsi, 2005). With the addition of the Copernicus program from ESA, free and open earth observation leaped forward with a spatial resolution of 10m and temporal resolution of 5 days. With an array of over 170 current high resolution and multispectral CubeSats, and with the daily repeat cycle Planet's constellation, we can create one of the most densely populated temporal data stack in work with near-daily global coverage in RGB and NIR band and at ~3m resolution. (Figure 3.3).

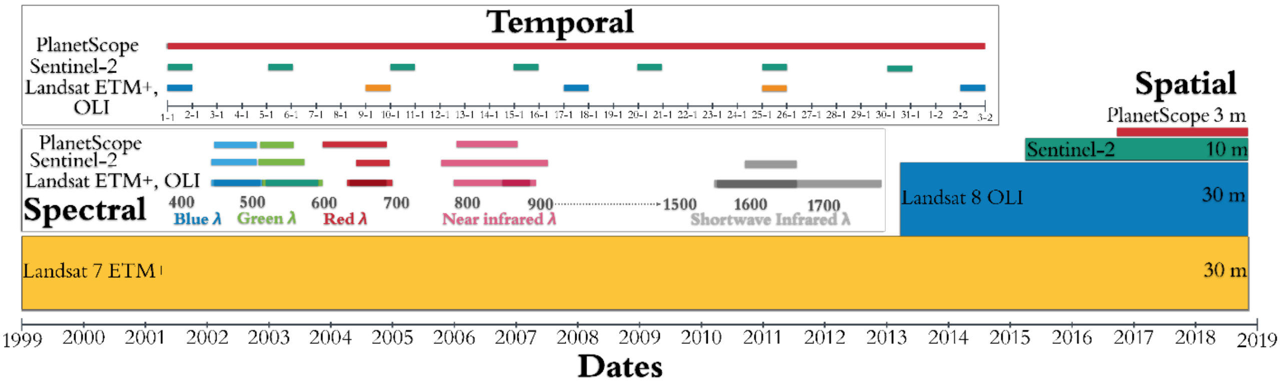

Figure 3.3: EOS dates of availability (years), temporal resolution (days), red and near-infrared spectral bands λ in nanometers (nm) used for NDVI, and spatial resolution in meters (m) for EOS platform data on Google Earth Engine.

With the deployment of Sentinel 2B and additional PlanetScope satellites, the temporal resolution of both these datasets has improved while Landsat 8 has kept a near consistent period. Satellite constellations and CubeSats are emerging and serving as essential and novel earth observation platforms. Large-scale patterns that were once lost by short temporal periods and granularity of imagery could now be analyzed, and historical and archival imagery could be included for analysis over an area of interest.

3.2.3 Imagery

We used the Landsat ecosystem disturbance adaptive processing system (LEDAPS) (Home et al., 2013; Ju et al., 2012; Schmidt et al., 2013) for Landsat 7 Surface Reflectance (SR) and the Landsat Surface Reflectance Code (LaSRC) (USGS 2016) SR product for the Landsat 8. For Sentinel-2, we use the Level-1C data with quality assurance (QA) bit bands present and available. Both Landsat 8 SR and Sentinel-2 L1C imagery are available for use GEE (Gorelick et al., 2017; Shelestov et al., 2017), making this the ideal development and analysis environment. For PlanetScope, we use a 4 Band analytic surface reflectance product

(Table 3.1) which is produced in combination with near simultaneous MODIS imagery for atmospheric correction (Wilson et al., 2017)

Table 3.1: Landsat 7 USGS LEDAPS Surface Reflectance, Landsat 8 USGS LaSRC Surface Reflectance, Sentinel-2, Cross calibrated PlanetScope SR and 4Band analytic for Grids

Platform	Spatial (m)	Temporal	Dates	Total Scenes
Landsat 7 & 8	30	16 days	01/01/2017-30/10/2018	1072
Sentinel-2	10	5 days	01/01/2017-30/10/2018	1665
PlanetScope	3	1-3	01/01/2017-30/10/2018	12353

3.2.4 Image Ingestion and Preprocessing

PlanetScope 4 Band SR imagery was downloaded using a command line interface (CLI) created by the author and released as an open source tool (Roy S., 2018) and later imported to GEE (Supplemental Materials). Only images with less than 75% cloud cover were used. Landsat 8 SR and Sentinel-2 data are already available in the data catalog within GEE and processed to make sure they are available at regular frequencies. To preprocess the Landsat data and Sentinel-2, we used QA bit cloud masking to remove obscured pixels. At the time of our analysis, a cloud mask product was not available for PlanetScope data; however, we did utilize the unusable data mask (UDM), which removed most clouds and saturated pixels. Since both Landsat 7 and Landsat 8 were used, a harmonization (Roy et al., 2016) was applied apart from the cloud masking before combining them into a single image collection. Once these techniques were applied, the datasets were normalized for consistency between multiple sensor and platform types, allowing us to use them for further analysis (Figure 3.4). For all three data sources, we created bimonthly composites and classified land-water boundaries using binary algorithms based on the Normalized Differential Water Index

(NDWI) (Gao, 1996), spectral unmixing (Keshava, 2003; Keshava and Mustard, 2002), statistical measures of monotonicity and variance using Mann Kendall statistics (Abdi, 2007; Hamed, 2008).

Overall all three sensors were compared for land loss and land gain detection. Landsat is the coarsest resolution among our three candidate sensors, with a spatial resolution of 30 m and a temporal resolution of about 16 days. While our use of Landsat-7 and Landsat 8 increased the temporal resolution to about 8 days, the SLC failure in Landsat 7 meant that there were large stripes in the data with missing pixels and as such the improvement in temporal resolution only went so far to improve the overall coverage and towards a cloud-free bi-monthly composite.

Sentinel-2A and 2B, on the other hand, had a varied spatial resolution ranging between 10 and 20 m spatial resolution for our bands of interest and a relatively higher temporal resolution of 5 days. However, this temporal resolution was inconsistent over different parts of the world as applied to global coverage. Similarly, while, PlanetScope constellation provided 3 m resolution, owing to smaller image footprints these images were also limited by the number of ground control points available for georectification. These conditions were further constrained by cloud masking across all sensors. While cloud masking was used to create cloud free composites for Landsat and Sentinel-2, it was possible that the masked composites resulted in large portions of the grid with missing pixels. Similarly, PlanetScope images with smaller image footprints sometimes do not get provide complete coverage of the grid as well.

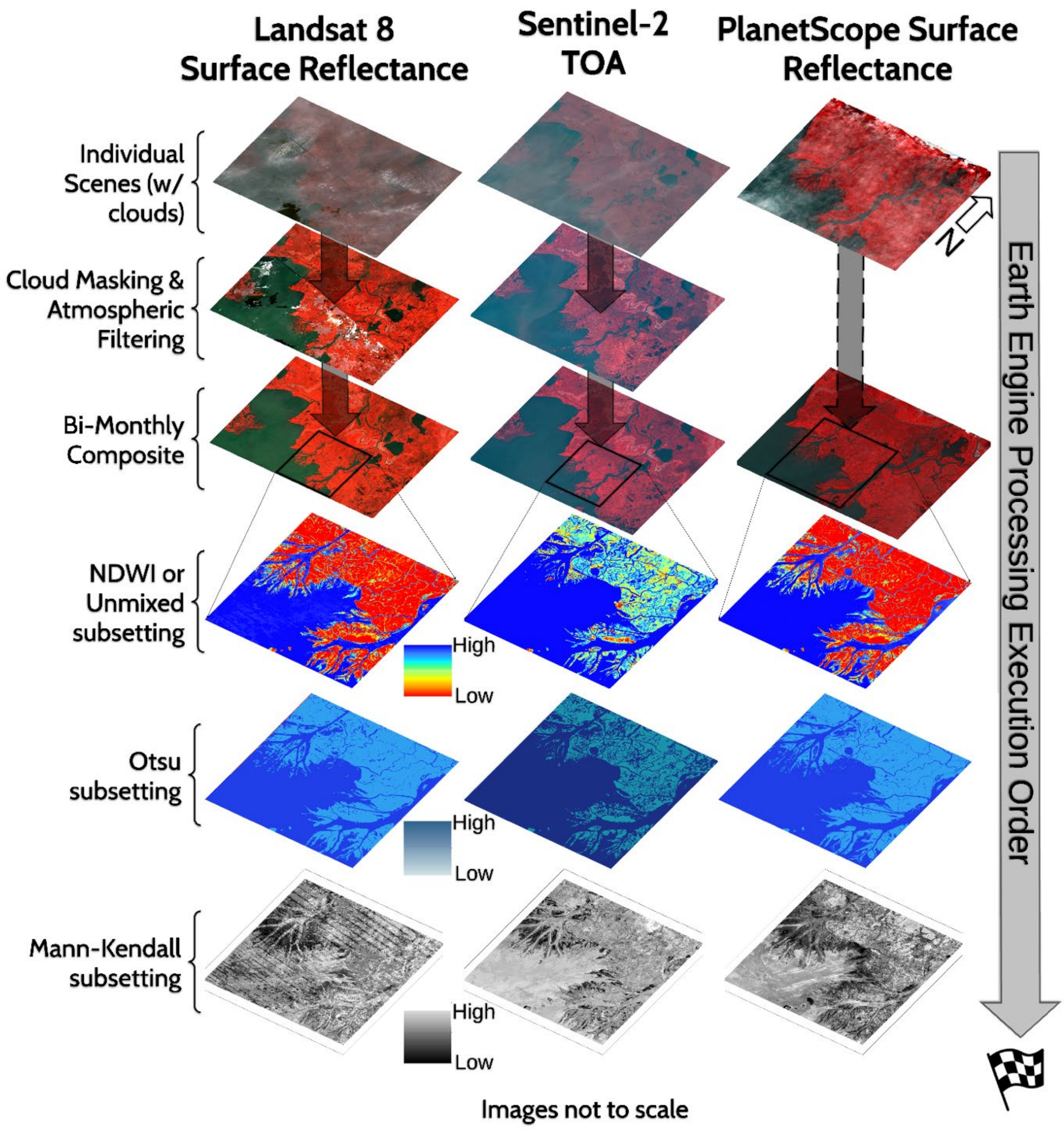

Figure 3.4: The overall methodology, Step 1) Landsat 7 & 8 ETM Surface Reflectance, Sentinel-2A & 2B Top of Atmosphere Reflectance (TOAR) and PlanetScope Constellation Surface Reflectance datasets were filtered and selected. Step 2) Cloud masking was applied to Landsat and Sentinel-2 datasets & UDM masking for PlanetScope Step 3) Bi-Monthly composites were created keeping in account the minimum time needed to develop effective cloud free composites. 4) Normalized Difference Water Index (NDWI) and constrained spectral unmixing was applied to Landsat, Sentinel-2 and PlanetScope constellation, and

Otsu's thresholding was used to both Index and unmixed data for creating binaries 5) Mann Kendall's Tau and Z Score were calculated for each pixel. 6) The temporal difference was calculated *from each binary t1-t2 pair*

To avoid issues with comparing composites with varying coverages, only those which met 100% coverage were used for the overall analysis. The QA band in S2 was utilized to get rid of large cloud, but the method retains cloud and haze which effects the stratified sampling if cloud artifacts are not removed in the bimonthly composites. Landsat7 and Landsat 8 harmonization we used (Roy et al., 2016) further cross-calibrated for the effect of large variations in-swath and removed issues of non-normalized pixels when creating composites. All three sensors produced mostly cloud free composites and areas with a large number of pixels missing owing to cloud removal were removed from observation and analysis. At the time of writing this paper, sen2cor based Sentinel-2 Surface reflectance was not available within GEE that would allow for better cloud masking. Bi-monthly temporal composites were created using three different methodologies and GEE reducers. Specifically, we used the median composite, percentile composite, and medoid composite for composite creation (Azzari and Lobell, 2017; Newingham et al., 2018; Sagar et al., 2018; White et al., 2014). Medoid composites perform better for datasets where the temporal stack or number of images is low, for example, Landsat (Flood, 2013; Petitjean et al., 2011). Median and percentile composites, on the other hand, performed better for Sentinel-2 and PlanetScope constellation images (Donchyts et al., 2016a, 2016b; Kovalskyy and Roy, 2013; Roy et al., 2016, 2010; Tuanmu and Jetz, 2015). Bi-monthly temporal composites were created for all image scenes. This composite allowed us to explore the interannual spatial and temporal variations of each dataset.

3.2.5 *Google Earth Engine CyberGIS*

GEE provides cloud-based EOS image processing across a vast array of satellites and sensors (Gorelick et al., 2017; Patel et al., 2015; Shelestov et al., 2017). The GEE environment rehosts many petabytes of freely released earth observation data. The GEE allows users to write their JavaScript algorithms, and analyze the data of any spatial extent or resolution. Before the advent of volumetric data analysis and high temporal resolution datasets, analyzing areas with large volumes of temporal data was nearly impossible with conventional methods. GEE frees the user from the burden of data movement and analysis on their computing infrastructure, which allows for repeatable and scalable scientific studies (Dong et al., 2016; Hansen et al., 2013; Kennedy et al., 2018). GEE is also unique because it allows the user to bring in their datasets apart from interacting with existing datasets using scripts. For this study, we ingested 15,829 PlanetScope images into GEE. The application of these tools for handling temporal, spatial, and spectral aspects of the analysis made was ideal for our study of land loss and fragmentation.

3.2.6 Image Classification and soft classification techniques

Detecting water in remotely sensed images is complicated because pixels contain atmospheric 'noise,' and may have temporally and spatially variable spectral properties caused by the underlying or overlaying materials that interact with the observed water surface. For example, subsurface vegetation, algal growth, and soil plumes, which change in time and are caused by both natural and anthropogenic reasons modify pixels spectral response. Classifying water with index-based approaches, such as the Normalized Difference Water Index (NDWI) [Eq 1] (Gao, 1996):

$$NDWI = \frac{(\rho Green - \rho NIR)}{(\rho Green + \rho NIR)} \qquad \text{[Eq 1] (Gao 1996)}$$

requires interclass thresholding and, as such, determining water among other classes is challenging. To circumvent issues with pixel classification thresholding, soft classification techniques such as Spectral unmixing (Keshava, 2003; Keshava and Mustard, 2002; Zhang et al., 2013) are useful because they estimate the percentage probability of what a pixel is rather than an absolute classification of a pixel as land or water. While this method provides a probability density function for multiple classes, it is still dependent on the endmember signatures used for training. As such an ensemble of methods was utilized to get at the classification of water followed by classification of land and vegetation. Soft classification provides us with a continuous value probability distribution for multiple classes representing temporal variation in percentage endmember for each pixel. This allowed us to trace the temporal trajectory of a pixel in terms of percentage probability of a class which can then be combined with binarization tools such as Otsu's method based binarization (Otsu, 1979).

For the PlanetScope imagery, which is at a spatial resolution of 3m but only has four spectral bands, endmember analysis using Spectral unmixing still allows for class segregation and discrimination among land water and vegetation. For our classification schema into the two classes (land and water), spectral unmixing was applied to the normalized and preprocessed composites for PlanetScope constellation, Landsat 8 Surface Reflectance Composites and Sentinel-2 TOAR composites. Index based classification (NDWI) and soft classification using spectral unmixing were then converted into binaries using Otsu method (Otsu, 1979) which could be utilized as binary threshold masks (for example vegetation/non-vegetation mask using Otsu applied to NDVI) or water mask as applied to NDWI to further improve on the overall land classification result. Otsu's thresholding does not relate to actual values of the index but rather chooses the threshold to maximize the interclass variance between the two classes.

3.2.7 Spectral Unmixing based Image Classification and Binarization

We used spectral unmixing to determine the proportion of land, water, and vegetation in each pixel. Soft classification techniques, such as spectral unmixing, allow for subpixel fractional abundance values of land or water classes for each pixel (Lu and Weng, 2007; Nath et al., 2014). To capture suitable land and water, persistent areas were used from high-resolution imagery in the area and earlier global models (Donchyts et al., 2016b; Pekel et al., 2016). Stratified sampling is designed to separate the populations into classes or strata for sampling (Imbens and Lancaster, 1996; Stehman, 2012; Tipton et al., 2014; Trost, 1986). In remote sensing, strata can refer to land cover classes (Brink and Eva, 2009; Congalton, 1991; Gallego, 2004; McRoberts and Tomppo, 2007) and in our paper, it refers to the stratification of water and not water. Spectral endmembers have to be collected from each image in the absence of a standard spectral signature (Sousa and Small, 2018, 2017) for "water" and "not water" class in a large spatial area. This is because local signatures vary based on various factors that control a pure pixel's spectral signature. Hence, stratified sampling per image composite allowed us to use image specific endmember signatures for spectral unmixing. The stratified sampling approach was applied within GEE while creating 100 points for water and nonwater classes. These two classes used for choosing the sample locations were based on the JRC annual water classification datasets (Pekel et al., 2016), which classified water and non-water binaries. This dataset was generated using over 3 million Landsat scenes and classified into water and not water using an expert classification system with an overall validation accuracy of over 95% based on over 40,124 ground control validation points. This permanent water and not water mask from the JRC dataset served as bounding area for restricting the random stratified sampling points to be generated in each of these classes separately without spatial overlaps. These were then exported as GEE assets to be used as sampling points for endmember calculation per temporal composite.

3.2.8 Constrained Spectral Unmixing and Otsu's Thresholding

Once the sampling points were generated within GEE, these points were then used to sample and create the endmember matrix array across each band and each sensor (Table 3.2). This was then further integrated into a python code to iteratively run for each grid and each sensor type. The benefit of a stratified random sampling strategy with a large number of points is that it decreases the probability of a null endmember matrix owing to missing data. This allowed us to use the detected endmembers for performing constrained spectral unmixing. Constrained spectral unmixing was used to make sure that the fraction summed to one. We can describe spectral unmixing using the linear mixing model (LMM) where we have *M* endmembers.

$$x = \sum_{i=1}^{M} a_i s_i + w = Sa + w$$

Where *x* is the *L* by 1 received spectrum vector, and *S* is the *L* by *M* matrix formed by the *L* by *M* matrix, *a* is the fractional abundance (*M* by 1 matrix), and *w* is the *L* by additive observation noise vector (Keshava and Mustard, 2002). Spectral unmixing provides fractional composition per pixel, and the water class was selected, and Otsu's thresholding based binarization was performed on fractional probability value for each pixel to generate land-water binaries. The overall method was tested overall all sensors across all temporal composites and spread through the spatial grids a total of 66 grids for each sensor which is 11 temporal grids times six grids and a total of 66 times three sensors or 198. The classified and binarized imagery were exported similar to our earlier results along with the unmixed composites for each spatio-temporal and sensor-based composite. Image scenes were exported from GEE using a python script.

3.2.9 Mann Kendall Time Series Analysis

Trend analysis of NDWI as an index as well as percentage class per pixel by unmixing, allows us to understand sudden abrupt changes (using a step trend method) or a monotonic and consistent directional change such as using a monotonic trend analysis (including linear trend analysis). Mann Kendall trend test is a test of monotonicity and tests the overall increase or decreases of a variable over time and is a non-parametric method for trend regression of monotonicity. The null hypothesis in a trend analysis is that there is no trend present in the data. The Mann Kendall test looks at the nonparametric form for increasing and decreasing monotonic trend regression. It analyzes the sign of the difference between t+1 and t-1 timed values of a data, with t representing the current period value of the dataset. This represents a total of n(n-1)/2 possible pair wise comparison of the datasets where n is the total number of observations. In our case, we have 11 observation periods from January 2017 to October 2018. The test is also considered as a robust nonparametric test because it allows for the data to be transformed (Helsel and Hirsch, 1992) and remains invariant to such a transformation (such as logs, etc.). Any pair of observations (y_i, y_j) where i<j then we calculate the difference y_j-y_i then we get either a positive difference (concordant pair) or a negative difference (discordant pair) or no difference (Equation 3).

$$S = \sum_{i=1}^{n-1} \sum_{j=i+1}^{n} sign(y_j - y_i) \qquad \text{[Eq-3]}$$

Then the test statistics τcan be calculated as

$$\tau = \frac{S}{n(n-1)/2} \qquad \text{[Eq 4]}$$

Simply put the Kendall τ coefficient is defined as

$$\tau = \frac{(number\ of\ concordant\ pairs) - (number\ of\ discordant\ pairs)}{n(n-1)/2} \qquad \text{Eq 4}$$

We calculate statistical significance and Z-score using the formula,

$$z = \frac{3 * T\sqrt{N(N-1)}}{\sqrt{2(2N+5)}} \qquad \text{Eq 5}$$

We calculate the Mann Kendall tau and Z-Score from the NDWI time series from Landsat, Sentinel-2 composites and PlanetScope composites and export it for each sensor and each grid based on the bimonthly composites. We further calculated Mann Kendall Tau and Z scores from the spectrally unmixing based water band. This gives a fractional percentage of water class for each pixel across all sensors and temporally. The Mann Kendall reducer was included in the GEE library, and a Z Score function was written to get to a measure of significance. The corresponding p-value is then calculated to look at areas of statistical significance ($p<0.05$) and allows for interpreting overall swaths of areas with monotonic trends of NDWI index score or fractional abundance of water derived from spectral unmixing which can be directly linked to the probability of the pixel being water and not land. This includes both monotonic increases and decreases, in the probability of the pixel being identified or remaining as water increases or decreases.

3.2.10 Version Control and Data Management

Data-intensive scientific discovery requires the research methodology to be repeatable (Hampton et al., 2015; Hettne et al., 2014; Hey et al., 2009). For this paper, all tools and scripts are configured in GEE toolboxes, with a detailed 'README' files, released with an open MIT license. Since GEE itself holds an internal GIT version control, all JavaScript-based code is available under both the internal GIT control from GEE, as well as uploaded to a public GitHub repository for release (github.com/samapriya/fragmentation-analysis). The tool and the datasets themselves have a Zenodo DOI (Roy, 2019) for ease of use and permanence. We follow an open-science principle and make available all derivative products, codes, and analysis for ease of reproducibility using the FAIR data principles (Wilkinson et al., 2016).

JavaScript and R codes are hosted GEE user profile /samapriya/ and permalink in a GitHub repository along with creating a project DOI in zenodo for maintaining consistent and citable coding practices. This allows for repeatability with our code and datasets were maintained, and derivatives were shared for ease of use. Python codes are created as functions that can be imported and extended by the end user and is created as both Python 2 and Python 3 compatible modules. Since frequent commits are made to the repo, commit logs are maintained, and change logs were added to the overall readme. To make research reproducible, GEE allows the user to create unique links which can then be shared to reproduce setup and run conditions. Reproducible and sustainability is at the core of our paper's design and methodology; as a result, we have created a data management table (Table 3.3) including diving them into segments namely Primary Datasets, Derived Datasets, Code, Location of Primary Dataset, Location of Derivative, Location of Code.

Table 3.3: Data management and distribution plan

Data	**Data Type**	**Data Location**	**Code Location**
Landsat 7 & 8 SR	Primary	GEE	GitHub Repo link GEE link
Sentinel-2 A & B	Primary	GEE	
PlanetScope SR	Primary	Not Shared based on End-user license	
Processing NDWI & Otsu thresholding	Code & Secondary	GEE and GitHub	GitHub Repo link GEE link
Processing and Stratified Sampling	Code & Secondary	GEE and GitHub	GitHub Repo link GEE link
Spectral Unmixing & Otsu thresholding	Code & Secondary	GEE and GitHub	GitHub Repo link GEE link

All noncommercial datasets are included in the code, and for Planet data, the code structure serves as the template and steps are included for the user to change source path for analysis. Datasets were packaged into a single release to generate DOI. These include JavaScript codes for GEE, Python modules for interacting with GEE, and preliminary and supplemental results.

3.3 Results and Discussions

The compiled dataset compares over 15,090 total images spread across Landsat, Sentinel-2, and PlanetScope sensors, with a total of 180 bi-monthly composites. We used 100 points per training class for the six 20 by 20 km grids with a total of 1200 points for endmember selection using stratified random sampling. To our knowledge, this is the first comparison of multiple sensors and using CubeSat based images, over deltaic environments to understand delta fragmentation.

In general, across our six different sample grids, Landsat and PlanetScope were highly correlated across time than either the correlations between LS and S2 or S2 and PS (Table 3.4, Figure 3.6, and 3.7). For example, Pearson's correlation statistics for almost all LS and PS was between X (0.59) and X1(0.97) for spectral unmixing and between X (0.37) and X1(0.97) for NDWI.

Table 3.4: Land Loss correlation analysis for each grid between Landsat (LS), Sentinel-2 (S2) and PlanetScope (PS) for both spectral unmixing and NDWI derived land loss estimates. Color codes indicate the strength of the correlation, with green indicating a strong correlation, yellow indicated moderate correlation and red indicates a weak correlation.

	Grid 1				Grid 2				Grid 3			
Spectral Unmixing		LS	S2	PS		LS	S2	PS		LS	S2	PS
	LS	1			LS	1			LS	1		
	S2	0.43	1		S2	-0.25	1		S2	0.66	1	
	PS	0.97	0.31	1	PS	0.08	0.70	1	PS	0.70	0.79	1
	Grid 4				Grid 5				Grid 6			
		LS	S2	PS		LS	S2	PS		LS	S2	PS
	LS	1			LS	1			LS	1		
	S2	0.71	1		S2	0.18	1		S2	0.18	1	
	PS	0.71	0.95	1	PS	0.81	0.21	1	PS	0.61	-0.12	1

NDWI	Grid 1				Grid 2				Grid 3			
		LS	S2	PS		LS	S2	PS		LS	S2	PS
	LS	1			LS	1			LS	1		
	S2	0.55	1		S2	0.31	1		S2	0.77	1	
	PS	0.59	0.88	1	PS	0.79	0.22	1	PS	0.97	0.62	1
	Grid 4				Grid 5				Grid 6			

	LS	S2	PS		LS	S2	PS		LS	S2	PS
LS	1			LS	1			LS	1		
S2	0.87	1		S2	0.72	1		S2	-0.08	1	
PS	0.86	0.87	1	PS	0.37	-0.19	1	PS	0.76	-0.21	1

Across the six grids, Sentinel-2 tended to differ most from the other two satellites in estimates of land loss and gain (Figures 5 & 6). This was particularly apparent in Grids 1 and Grid 5. Grids G3 and G4 behave consistently across Sentinel-2, PlanetScope and Landsat sensors.

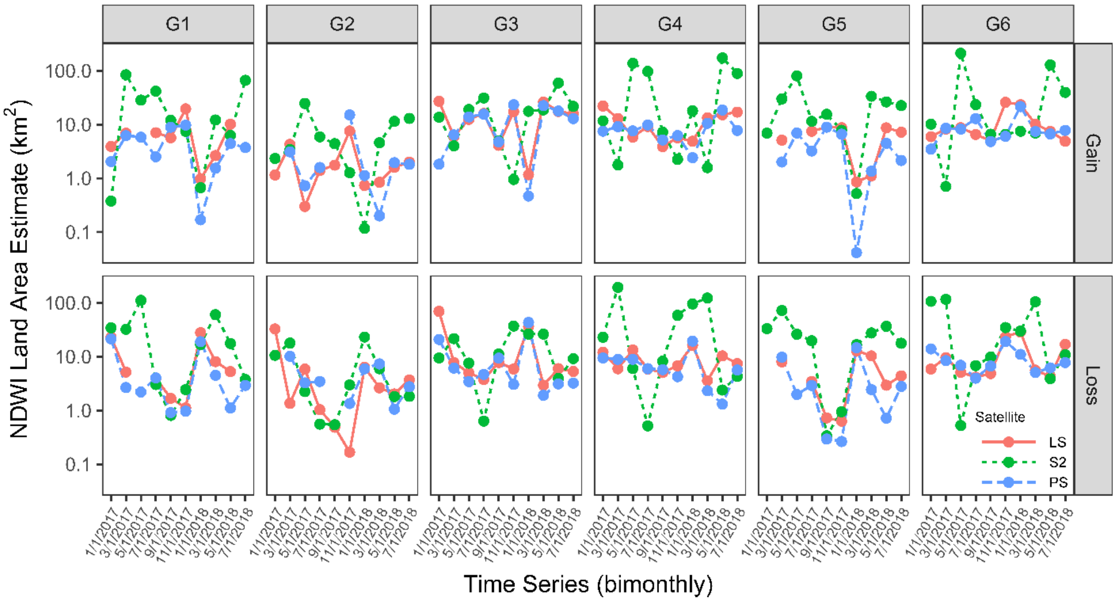

Figure 3.5: Land gain (upper panels) and loss (lower panels) estimates over time for three different sensors using NDWI. Horizontal panels represent land area estimates across six different 20x20 km² grids in the LMRD. Starting date for bimonthly series is depicted along the x-axis. The y-axis is shown on a log scale. LS = Landsat, S2 = Sentinel-2 and PS = PlanetScope Constellation.

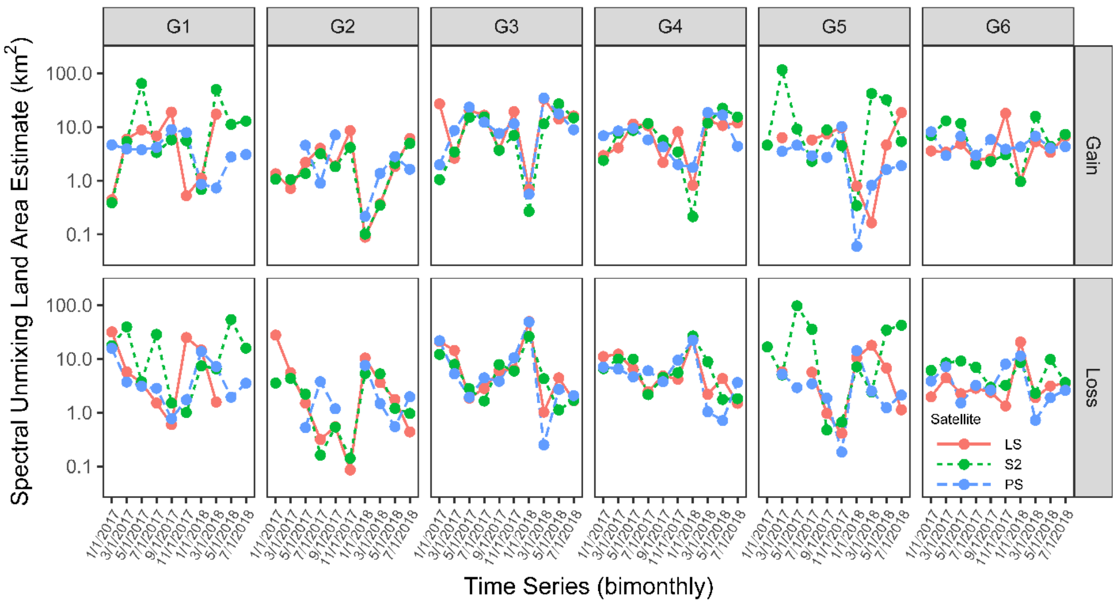

Figure 3.6: Land gain (upper panels) and loss (lower panels) estimates over time for three different sensors using constrained spectral unmixing. Horizontal panels represent land area estimates across six different 20x20 km² grids in the LMRD. Starting date for bimonthly series is depicted along the x-axis. The y-axis is shown on a log scale. LS = Landsat, S2 = Sentinel-2 and PS = PlanetScope Constellation.

Grid 1 and Grid 5, located in Terrebonne and Barataria, respectively are among the most fragmented grids within our study design. Large scale fragmentation increases the overall edges or land-water boundaries where these two classes interact. The edge effect or land and water interactions are amplified by landscape fragmentation and in turn, also amplifies the effect of wind and tidal effects which travel more inland. Coupled with episodic events such as cyclones and periodic events such as precipitation induced sediment plumes can cause higher rates of accretion (Barras, 2007; Day et al., 2007) and temporarily reduce overall land loss. Overall estimates of land loss and land gain across the six grids and three satellite sensors were consistently higher for the spectral unmixing method compared to the NDWI method (Figure 3.5 & 3.6). Spectral unmixing also seemed to consistently perform better in the classification of land and water area and in maintaining harmony between the results from different sensors. Our hypothesis was tied to the sensor agnostic nature of index-based approach (NDWI) which uses the same band for all sensors, where high spectral resolution used in spectral unmixing provides more feature space and hence should provide higher accuracy in sensors with higher spectral resolution. However true classification and separation of land and water classes is dependent on more than just spectral resolution but also things like fragmentation of the landscape, the sampling strategy used to collect land and water signature (Stehman, 2012; Tipton et al., 2014; Trost, 1986), and spatial resolution of the image to account for mixed pixel issue encountered during soft classification and hard classification approaches (Atkinson, 2005; Zhang et al., 2013).

Grid 1 and Grid 5 seem to be the most affected which are also the ones that have the largest open water area and most fragmented, these can affect the stratified sampling applied to the imagery with the possibility of capturing mixed end member signatures. This yields an interesting methodological choice where a user-defined area of endmember selection with low count maybe more useful and significant that maintaining statistically unbiased endmember selection. Earlier studies (Stehman, 2012; Tipton et al., 2014; Trost, 1986) have shown the importance of sample size selection for stratified sampling and finding optimal sample size is difficult keeping in mind the variability of the end product. Sentinel-2, albeit its high spectral resolution, does not match to Landsat and PlanetScope results for both index-based and spectral unmixing. We also consistently find Landsat and PlanetScope to behave in harmony and have medium to strong correlation across all grids and through the temporal distribution (Table 3.4).

Of the two methods used to identify land and water, NDWI, which is an index based method, uses the same bands across all sensors meaning it does not benefit from the spectral resolution of one sensor compared to the other. Thus NDWI is inherently sensor agnostic. Spectral unmixing, on the other hand, relies on spectral resolution (or the number of bands) for separation of class into land and water categories. As such a constrained comparison is better seen with the index based approach using NDWI, however since the classification of land and water edges is dependent on more than just the spectral resolution our results show varying degree of success of each methodology which is spatially and spectrally variant.

3.3.1 Interpretations and research implications

The differences in the behavior of one sensor compare to the other, along with possible reasons that might contribute to such variations have been discussed in the following sections. The authors would like to clarify that these interpretations are based on established literature as well as inference of observed results from the analysis.

3.3.2 Effect of Top of Atmosphere and Surface Reflectance

We used Landsat 8 and PlanetScope surface reflectance data for our study. At the time of preparation of the article Sentinel-2 surface reflectance product was not available within the Earth Engine environment. Planetscope sensors are calibrated to meet with the spectral response function of Landsat surface reflectance. That being said, the process automatically scales the data and applies an atmospheric correction to both of these data sources. Sentinel-2 dataset, on the other hand, does not scale and not atmospherically corrected. This also meant that combined with the available cloud masking methodology being used for Sentinel-2 data, it is more sensitive to atmospheric effects and hence behaves relatively differently along with integrating atmospheric effects and not removing them from the base imagery. This difference in the data type

3.3.3 Effect of Cloud Masking

While the Landsat surface reflectance imagery has a well-developed cloud mask (Foga et al., 2017; Ju and Roy, 2008; Martinuzzi et al., 2007), the Sentinel-2A L1C cloud mask product is not currently reliable and has been discussed in other works that compare Landsat and Sentinel-2 cloud masking algorithms and outcomes (Claverie et al., 2018; Helder et al., 2018;

Storey et al., 2016; Zhang et al., 2018). Similarly, at the time of writing this paper, cloud masks were not available for PlanetScope data, and as a result, the bimonthly composited depended on the temporal depth of the image stack. This was used as a discriminant whereby since cloudy pixels would not occur over the same region through the entire time stack, a composite function would discriminate and remove the cloud value and choose a pixel value from the stack. This method works quite well for our area of interest, and all generated composites are visually checked for cloud visibility. This variability in the availability and performance of cloud masking algorithms allows the sensors to have different degrees of clouds free composites. As a result of the poor performance of the Sentinel-2 cloud masks, we hypothesize that the over or underestimation of land or water pixels may be a result of areas with existing cloud which are aggregated into the NDWI threshold by Otsu's thresholding. We see this behavior of S2 estimates to be much better using spectral unmixing whereby the contributing class of the imagery determines the class percentage per pixel. Here stratified sampling throughout the grid allows for a better representation of the spectral signature of the class, rather than choosing fixed larger areas which might be obscured in the bimonthly composites.

3.3.4 Effect of temporal windows

The bimonthly composites produced by different sensors are dependent on more than just the spatial location of the grid itself, but the temporal resolution and the start and end dates that capture or miss such events (Figure 3.7). We find this to be consistent with spikes in the land loss as well as temporal lags, which are an effect of varying sensors capturing or missing an event. This points to the importance of interannual variability as a means to understand changes in the landscape and also to the importance of temporal resolution while making long term assessments of such dynamic landscapes. While studies in the past have tried to eliminate temporal stochasticity (also called temporal biases) (Méndez-Barroso et al., 2009;

Xu and Wu, 2006) by long term assessment, these changes result in changes in the landscape that are observable over longer time scales.

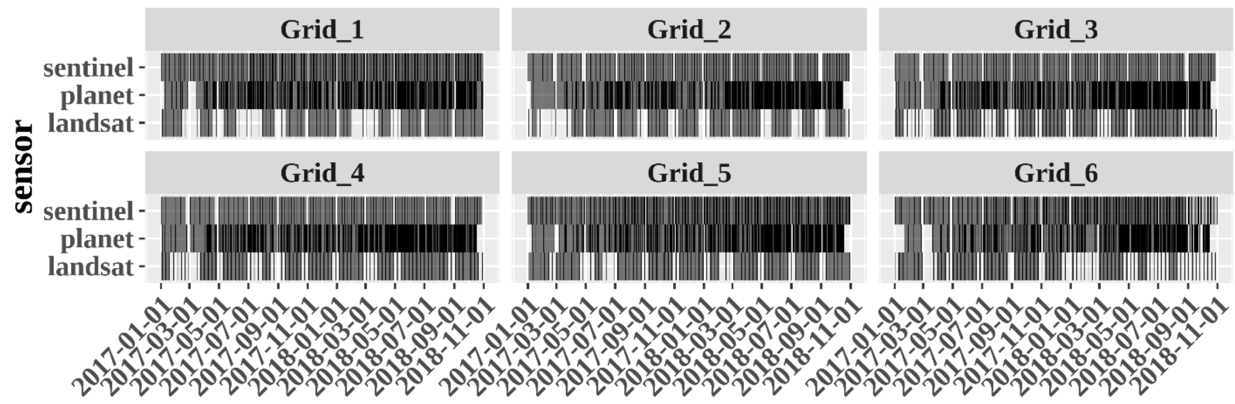

Figure 3.7: Distribution of Start and End Dates of images within the Bi-Monthly distribution of images for all sensors. Dark ticks represent individual images in the collection for all six grids for each sensor type.

The process of creating inter-annual temporal composites across multiple sensors introduces the concept of temporal lag that may be attributed to the variation in start and end dates of images used for each temporal window. This lag can result in land loss that might be visible in a high temporal resolution satellite may only become apparent in the next composite (Figure 3.6) for a different sensor owing to the temporal resolution of the sensor. Thus, apart from choices in the temporal windows, the start and end dates and the number of images used in the adjusted time periods determine captures landscape loss. In our study though the date filters for all image collections throughout two years 2016-2018 were the same, the start and end dates of the images used for each sensor varied (table included in supplemental) owing to the difference in temporal frequency (Gašparović et al., 2018, p. 2; Li and Roy, 2017). We posit that this variation in the composite start and end dates in our composites contributed to a difference in the compared land loss across each sensor.

Temporally coarser images also have a limited number of images that could go into the composite creation pipeline, further limiting the resultant composites. As a result, certain events which may be missed in one time period by a temporally coarse sensor or limited by the number of images that may become prominently visible in the next time period.

3.3.5 Effect of Monotonicity and trajectory of Land Loss

Unmixing as well as NDWI classifies a pixel as land and water by calculating either fractional percentage composition per pixel or simply the index based measure of water based on NDWI. It is then classified as water during the binarization process. The Mann Kendall statistics provides a temporal analysis of the trajectory of pixels as it either converts to a water pixel, or land pixel or keeps changing between the two classes over and over again. In our study, positive monotonicity represents areas where the pixel probability of being classified as water increase. The result is a tendency toward land loss. Grid 3, represented in Figure 3.8, shows a delta area with sediment flow and accretion, the mixed effects of land loss are colored by their standard deviation from the mean. Low or zero standard deviation (greens) represent areas which are close to the mean and have little or no monotonicity.

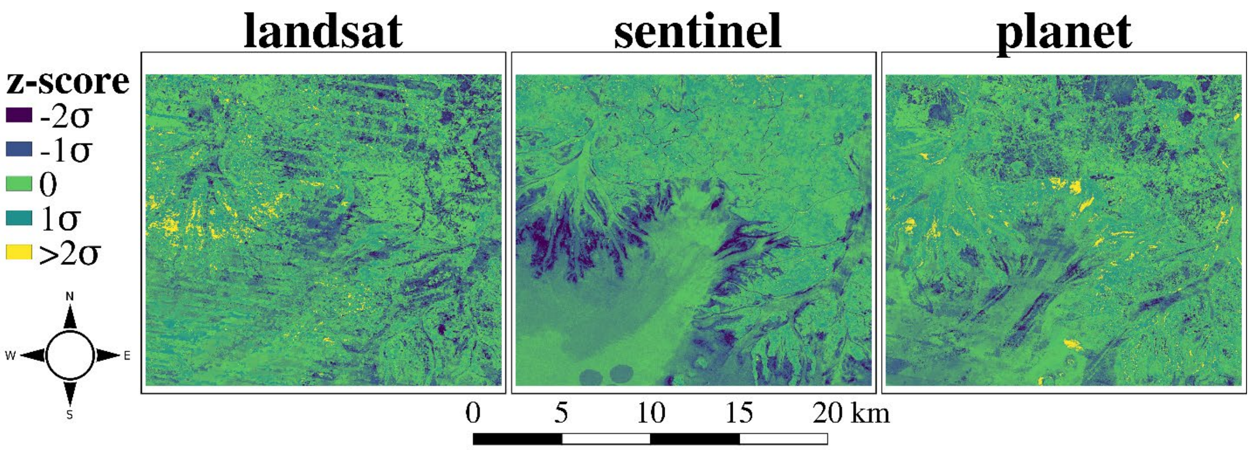

Figure 3.8: Mann-Kendall Z scores as estimates of monotonicity. As an example, applied to Grid-3 for the spectral unmixing derived land and water boundaries.

Landsat (Fig 8, left panel) showed smaller patches areas beyond two standard deviation (95%) of land loss and land gain (note: banding is due to the Landsat 7 ETM+ scan line corrector). Sentinel (Fig. 8, center panel) reveals more negative monotonicity with patches of accretion along the edges of the delta. PlanetScope (Fig. 8, right panel) which was harmonized to Landsat (resulting in scan line corrector banding) shows similar patches of areas with land loss; with increased positive monotonicity in the same areas as Landsat, showing areas with ephemeral land gain. These analyses were performed for all grids, for all sensors (see Supplemental Materials).

Choice of the sensor is paramount to understanding land loss and is a function of the overall effect being observed, the type of methodology being used, and the end result we expect from such analysis. As derivatives from source imagery such as Sentinel-2 Surface Reflectance imagery, along with cloud masking data as well as Planet's udm2 cloud mask data become available, our methodologies will change and evolve. Though the composites will get better and relative difference in estimates should decrease, high frequency of interannual variability still requires a deeper time stack to avoid issues with missing data and holes in our observation. Depending on the rate of change of the observed processes in the landscape sensor characteristics including but not limited to spatial, temporal, and spectral characteristics are important for landscape studies. Rapid land loss or deterioration in our study area requires near-daily imagery and a constant coastal watch that logs loss and gain in areas and compares them robustly across multiple sensors for cross-validation. As methods in remote sensing and machine learning become more available and the overall study of coastal areas at such smaller time scale might become possible, validation would be challenging and would require reported datasets to be integrated into formats that could be used for field calibration and validation.

3.4 Summary

Land water boundary delineation is critical in getting accurate estimates of the amount of land loss and also to make sure that pixel resolution does not have a detrimental effect during overall area estimates. Land loss is a function of space and time, and stochastic events are often hard to capture depending on the frequency of the events and the duration. PlanetScope multiple returns allow us to isolate these episodic events and utilize them for fine grain edge detection of land loss and or land gain. Our estimates are not a direct measure of land-loss. However, the study gives a fine-grained understanding of the issues with image compositing and comparison across multiple sensors, interpretation of land edges effected by water color remote sensing remains an open-ended question.

We hope future studies will leverage computational High-performance Cluster Computing (HPCC) and cloud environments such as NSF funded CyVerse (Devisetty et al., 2016; Goff et al., 2011; Merchant, 2017; Merchant et al., 2016), for resolving issues with software dependencies by creating pre-built images (containers) consisting of all tools used in analyses. Future work will involve the concept of sensor fusion and trying to utilize the fine grain resolution of Sentinel-2 and PlanetScope sensors to create a mixed fused product which would have high spatial and spectral granularity.

3.5 Acknowledgments

SR and DE were supported in part by the Planet Labs Ambassador Program, TLS was supported by Cyverse Grant NSF DBI-1265383, DBI-1743442, Planet Labs imagery was provided by Planet Labs Education and Research Program.

References

Abdi, H., 2007. The Kendall rank correlation coefficient. Encyclopedia of Measurement and Statistics. Sage, Thousand Oaks, CA 508–510.

Allison, M.A., 2012. Historical changes in the Ganges-Brahmaputra delta front. Journal of Coastal Research 14.

Atkinson, P.M., 2005. Sub-pixel target mapping from soft-classified, remotely sensed imagery. Photogrammetric Engineering & Remote Sensing 71, 839–846.

Azzari, G., Lobell, D.B., 2017. Landsat-based classification in the cloud: An opportunity for a paradigm shift in land cover monitoring. Remote Sensing of Environment 202, 64–74.

Barras, J.A., 2007. Satellite images and aerial photographs of the effects of Hurricanes Katrina and Rita on coastal Louisiana. Geological Survey (US).

Bianchi, T.S., Allison, M.A., 2009. Large-river delta-front estuaries as natural "recorders" of global environmental change. Proceedings of the National Academy of Sciences 106, 8085–8092.

Brink, A.B., Eva, H.D., 2009. Monitoring 25 years of land cover change dynamics in Africa: A sample based remote sensing approach. Applied Geography 29, 501–512.

Claverie, M., Ju, J., Masek, J.G., Dungan, J.L., Vermote, E.F., Roger, J.-C., Skakun, S.V., Justice, C., 2018. The Harmonized Landsat and Sentinel-2 surface reflectance data set. Remote Sensing of Environment 219, 145–161.

Congalton, R.G., 1991. A review of assessing the accuracy of classifications of remotely sensed data. Remote sensing of environment 37, 35–46.

Day, J.W., Boesch, D.F., Clairain, E.J., Kemp, G.P., Laska, S.B., Mitsch, W.J., Orth, K., Mashriqui, H., Reed, D.J., Shabman, L., 2007. Restoration of the Mississippi Delta: lessons from hurricanes Katrina and Rita. science 315, 1679–1684.

Devisetty, U.K., Kennedy, K., Sarando, P., Merchant, N., Lyons, E., 2016. Bringing your tools to cyverse discovery environment using docker. F1000Research 5.

Donchyts, G., Baart, F., Winsemius, H., Gorelick, N., Kwadijk, J., van de Giesen, N., 2016a. Earth's surface water change over the past 30 years. Nature Climate Change 6, 810.

Donchyts, G., Schellekens, J., Winsemius, H., Eisemann, E., van de Giesen, N., 2016b. A 30 m resolution surface water mask including estimation of positional and thematic differences using landsat 8, srtm and openstreetmap: a case study in the Murray-Darling Basin, Australia. Remote Sensing 8, 386.

Dong, J., Xiao, X., Menarguez, M.A., Zhang, G., Qin, Y., Thau, D., Biradar, C., Moore III, B., 2016. Mapping paddy rice planting area in northeastern Asia with Landsat 8 images, phenology-based algorithm and Google Earth Engine. Remote sensing of environment 185, 142–154.

Flood, N., 2013. Seasonal composite Landsat TM/ETM+ images using the medoid (a multi-dimensional median). Remote Sensing 5, 6481–6500.

Foga, S., Scaramuzza, P.L., Guo, S., Zhu, Z., Dilley, R.D., Beckmann, T., Schmidt, G.L., Dwyer, J.L., Joseph Hughes, M., Laue, B., 2017. Cloud detection algorithm comparison and validation for operational Landsat data products. Remote Sens. Environ. 194, 379–390.

Foody, G.M., 2004. Sub-pixel methods in remote sensing, in: Remote Sensing Image Analysis: Including the Spatial Domain. Springer, pp. 37–49.

Gallego, F.J., 2004. Remote sensing and land cover area estimation. International Journal of Remote Sensing 25, 3019–3047.

Gao, B.-C., 1996. NDWI—A normalized difference water index for remote sensing of vegetation liquid water from space. Remote sensing of environment 58, 257–266.

Gašparović, M., Medak, D., Pilaš, I., Jurjević, L., Balenović, I., 2018. Fusion of Sentinel-2 and PlanetScope Imagery for Vegetation Detection and Monitorin, in: Volumes ISPRS TC I Mid-Term Symposium Innovative Sensing-From Sensors to Methods and Applications.

Goff, S.A., Vaughn, M., McKay, S., Lyons, E., Stapleton, A.E., Gessler, D., Matasci, N., Wang, L., Hanlon, M., Lenards, A., 2011. The iPlant collaborative: cyberinfrastructure for plant biology. Frontiers in plant science 2, 34.

Gorelick, N., Hancher, M., Dixon, M., Ilyushchenko, S., Thau, D., Moore, R., 2017. Google Earth Engine: Planetary-scale geospatial analysis for everyone. Remote Sensing of Environment 202, 18–27.

Hamed, K.H., 2008. Trend detection in hydrologic data: the Mann–Kendall trend test under the scaling hypothesis. Journal of hydrology 349, 350–363.

Hampton, S.E., Anderson, S.S., Bagby, S.C., Gries, C., Han, X., Hart, E.M., Jones, M.B., Lenhardt, W.C., MacDonald, A., Michener, W.K., 2015. The Tao of open science for ecology. Ecosphere 6, 1–13.

Han-Qiu, X.U., 2005. A study on information extraction of water body with the modified normalized difference water index (MNDWI)[J]. Journal of Remote Sensing 5, 589–595.

Hansen, M.C., Potapov, P.V., Moore, R., Hancher, M., Turubanova, S.A.A., Tyukavina, A., Thau, D., Stehman, S.V., Goetz, S.J., Loveland, T.R., 2013. High-resolution global maps of 21st-century forest cover change. science 342, 850–853.

Helder, D., Markham, B., Morfitt, R., Storey, J., Barsi, J., Gascon, F., Clerc, S., LaFrance, B., Masek, J., Roy, D., 2018. Observations and Recommendations for the Calibration of Landsat 8 OLI and Sentinel 2 MSI for improved data interoperability. Remote Sensing 10, 1340.

Helsel, D.R., Hirsch, R.M., 1992. Statistical Methods in Water Resources. Elsevier.

Hettne, K.M., Dharuri, H., Zhao, J., Wolstencroft, K., Belhajjame, K., Soiland-Reyes, S., Mina, E., Thompson, M., Cruickshank, D., Verdes-Montenegro, L., 2014. Structuring research methods and data with the research object model: genomics workflows as a case study. Journal of biomedical semantics 5, 41.

Hey, T., Tansley, S., Tolle, K.M., 2009. The fourth paradigm: data-intensive scientific discovery. Microsoft research Redmond, WA.

Heylen, R., Scheunders, P., 2011. Non-linear fully-constrained spectral unmixing, in: Geoscience and Remote Sensing Symposium (IGARSS), 2011 IEEE International. IEEE, pp. 1295–1298.

Home, O.D.H.N., List, C.D., Npp, N.P.P., Questions, D.P., Curation, D., Visualizer, S.M., Checker, L.-W., 2013. LEDAPS calibration, reflectance, atmospheric correction preprocessing code, version 2.

Imbens, G.W., Lancaster, T., 1996. Efficient estimation and stratified sampling. Journal of Econometrics 74, 289–318.

Ju, J., Roy, D.P., 2008. The availability of cloud-free Landsat ETM+ data over the conterminous United States and globally. Remote Sensing of Environment 112, 1196–1211.

Ju, J., Roy, D.P., Vermote, E., Masek, J., Kovalskyy, V., 2012. Continental-scale validation of MODIS-based and LEDAPS Landsat ETM+ atmospheric correction methods. Remote Sensing of Environment 122, 175–184.

Kennedy, R.E., Yang, Z., Gorelick, N., Braaten, J., Cavalcante, L., Cohen, W.B., Healey, S., 2018. Implementation of the LandTrendr Algorithm on Google Earth Engine. Remote Sensing 10.

Keshava, N., 2003. A survey of spectral unmixing algorithms. Lincoln laboratory journal 14, 55–78.

Keshava, N., Mustard, J.F., 2002. Spectral unmixing. IEEE signal processing magazine 19, 44–57.

Kolker, A.S., Allison, M.A., Hameed, S., 2011. An evaluation of subsidence rates and sea-level variability in the northern Gulf of Mexico. Geophysical Research Letters 38.

Kovalskyy, V., Roy, D.P., 2013. The global availability of Landsat 5 TM and Landsat 7 ETM+ land surface observations and implications for global 30 m Landsat data product generation. Remote Sensing of Environment 130, 280–293.

Li, J., Roy, D.P., 2017. A Global Analysis of Sentinel-2A, Sentinel-2B and Landsat-8 Data Revisit Intervals and Implications for Terrestrial Monitoring. Remote Sensing 9, 902.

Lu, D., Weng, Q., 2007. A survey of image classification methods and techniques for improving classification performance. International journal of Remote sensing 28, 823–870.

Markham, B.L., Storey, J.C., Williams, D.L., Irons, J.R., 2004. Landsat sensor performance: history and current status. IEEE Transactions on Geoscience and Remote Sensing 42, 2691–2694.

Martinuzzi, S., Gould, W.A., González, O.M.R., 2007. Creating cloud-free Landsat ETM+ data sets in tropical landscapes: cloud and cloud-shadow removal. US Department of Agriculture, Forest Service, International Institute of Tropical Forestry. Gen. Tech. Rep. IITF-32. 32.

McRoberts, R.E., Tomppo, E.O., 2007. Remote sensing support for national forest inventories. Remote Sensing of Environment 110, 412–419.

Méndez-Barroso, L.A., Vivoni, E.R., Watts, C.J., Rodríguez, J.C., 2009. Seasonal and interannual relations between precipitation, surface soil moisture and vegetation dynamics in the North American monsoon region. J. Hydrol. 377, 59–70.

Merchant, N., 2017. Computing at scale: From laptop to cloud and HPC.

Merchant, N., Lyons, E., Goff, S., Vaughn, M., Ware, D., Micklos, D., Antin, P., 2016. The iPlant collaborative: cyberinfrastructure for enabling data to discovery for the life sciences. PLoS biology 14, e1002342.

Nath, S.S., Mishra, G., Kar, J., Chakraborty, S., Dey, N., 2014. A survey of image classification methods and techniques, in: Control, Instrumentation, Communication and Computational Technologies (ICCICCT), 2014 International Conference On. IEEE, pp. 554–557.

Newingham, B., Strand, E., Morgan, P., 2018. USDA Forest Service Rocky Mountain Research Station.

Otsu, N., 1979. A threshold selection method from gray-level histograms. IEEE transactions on systems, man, and cybernetics 9, 62–66.

Patel, N.N., Angiuli, E., Gamba, P., Gaughan, A., Lisini, G., Stevens, F.R., Tatem, A.J., Trianni, G., 2015. Multitemporal settlement and population mapping from Landsat using Google Earth Engine. International Journal of Applied Earth Observation and Geoinformation 35, 199–208.

Pekel, J.-F., Cottam, A., Gorelick, N., Belward, A.S., 2016. High-resolution mapping of global surface water and its long-term changes. Nature 540, 418.

Petitjean, F., Ketterlin, A., Gançarski, P., 2011. A global averaging method for dynamic time warping, with applications to clustering. Pattern Recognition 44, 678–693.

Pratolongo, P., Mazzon, C., Zapperi, G., Piovan, M.J., Brinson, M.M., 2013. Land cover changes in tidal salt marshes of the Bahía Blanca estuary (Argentina) during the past 40 years. Estuarine, Coastal and Shelf Science 133, 23–31.

Rabalais, N.N., Turner, R.E., Scavia, D., 2002. Beyond Science into Policy: Gulf of Mexico Hypoxia and the Mississippi River: Nutrient policy development for the Mississippi River watershed reflects the accumulated scientific evidence that the increase in nitrogen loading is the primary factor in the worsening of hypoxia in the northern Gulf of Mexico. AIBS Bulletin 52, 129–142.

Restrepo, J.D., Kettner, A., 2012. Human induced discharge diversion in a tropical delta and its environmental implications: The Patía River, Colombia. Journal of Hydrology 424, 124–142.

Reyes, E., Martin, J.F., White, M.L., Day, J.W., Kemp, G.P., 2004. Habitat Changes in the Mississippi Delta: Future scenarios and alternatives, in: Landscape Simulation Modeling. Springer, pp. 119–142.

Rouse, L.J., Roberts, H.H., Cunningham, R.H.W., 1978. Satellite observation of the subaerial growth of the Atchafalaya Delta, Louisiana. Geology 6, 405–408.

Roy, D.P., Ju, J., Kline, K., Scaramuzza, P.L., Kovalskyy, V., Hansen, M., Loveland, T.R., Vermote, E., Zhang, C., 2010. Web-enabled Landsat Data (WELD): Landsat ETM+ composited mosaics of the conterminous United States. Remote Sensing of Environment 114, 35–49.

Roy, D.P., Kovalskyy, V., Zhang, H.K., Vermote, E.F., Yan, L., Kumar, S.S., Egorov, A., 2016. Characterization of Landsat-7 to Landsat-8 reflective wavelength and normalized difference vegetation index continuity. Remote Sensing of Environment 185, 57–70.

Roy, S., 2018. samapriya/Planet-GEE-Pipeline-CLI: Planet-GEE- Pipeline-CLI. https://doi.org/10.5281/zenodo.1407464

Sagar, S., Phillips, C., Bala, B., Roberts, D., Lymburner, L., 2018. Generating Continental Scale Pixel-Based Surface Reflectance Composites in Coastal Regions with the Use of a Multi-Resolution Tidal Model. Remote Sensing 10, 480.

Scaramuzza, P., Barsi, J., 2005. Landsat 7 scan line corrector-off gap-filled product development, in: Proceeding of Pecora. pp. 23–27.

Schmidt, G., Jenkerson, C., Masek, J., Vermote, E., Gao, F., 2013. Landsat ecosystem disturbance adaptive processing system (LEDAPS) algorithm description. US Geological Survey.

Shelestov, A., Lavreniuk, M., Kussul, N., Novikov, A., Skakun, S., 2017. Exploring Google Earth Engine platform for big data processing: classification of multi-temporal satellite imagery for crop mapping. Frontiers in Earth Science 5, 17.

Sousa, D., Small, C., 2018. Spectral Mixture Analysis as a Unified Framework for the Remote Sensing of Evapotranspiration. EarthArXiv. October 25.

Sousa, D., Small, C., 2017. Global cross-calibration of Landsat spectral mixture models. Remote sensing of environment 192, 139–149.

Stehman, S.V., 2012. Impact of sample size allocation when using stratified random sampling to estimate accuracy and area of land-cover change. Remote Sensing Letters 3, 111–120.

Storey, J., Roy, D.P., Masek, J., Gascon, F., Dwyer, J., Choate, M., 2016. A note on the temporary misregistration of Landsat-8 Operational Land Imager (OLI) and Sentinel-2 Multi Spectral Instrument (MSI) imagery. Remote Sensing of Environment 186, 121–122.

Syvitski, J.P., Kettner, A.J., Overeem, I., Hutton, E.W., Hannon, M.T., Brakenridge, G.R., Day, J., Vörösmarty, C., Saito, Y., Giosan, L., 2009. Sinking deltas due to human activities. Nature Geoscience 2, 681–686.

Tipton, E., Hedges, L., Vaden-Kiernan, M., Borman, G., Sullivan, K., Caverly, S., 2014. Sample selection in randomized experiments: A new method using propensity score stratified sampling. Journal of Research on Educational Effectiveness 7, 114–135.

Trost, J.E., 1986. Statistically nonrepresentative stratified sampling: A sampling technique for qualitative studies. Qualitative sociology 9, 54–57.

Tuanmu, M.-N., Jetz, W., 2015. A global, remote sensing-based characterization of terrestrial habitat heterogeneity for biodiversity and ecosystem modelling. Global Ecology and Biogeography 24, 1329–1339.

Turner, R.E., Rabalais, N.N., 1991. Changes in Mississippi River Water Quality This Century. Bioscience 41, 140–147.

Walling, D.E., 2008. The changing sediment load of the Mekong River. Ambio 37, 150–157.

Walling, D.E., Fang, D., 2003. Recent trends in the suspended sediment loads of the world's rivers. Glob. Planet. Change 39, 111–126.

White, J.C., Wulder, M.A., Hobart, G.W., Luther, J.E., Hermosilla, T., Griffiths, P., Coops, N.C., Hall, R.J., Hostert, P., Dyk, A., 2014. Pixel-based image compositing for large-area dense time series applications and science. Canadian Journal of Remote Sensing 40, 192–212.

Wilkinson, M.D., Dumontier, M., Aalbersberg, I.J.J., Appleton, G., Axton, M., Baak, A., Blomberg, N., Boiten, J.-W., da Silva Santos, L.B., Bourne, P.E., Bouwman, J., Brookes, A.J., Clark, T., Crosas, M., Dillo, I., Dumon, O., Edmunds, S., Evelo, C.T., Finkers, R., Gonzalez-Beltran, A., Gray, A.J.G., Groth, P., Goble, C., Grethe, J.S., Heringa, J., 't Hoen, P.A.C., Hooft, R., Kuhn, T., Kok, R., Kok, J., Lusher, S.J., Martone, M.E., Mons, A., Packer, A.L., Persson, B., Rocca-Serra, P., Roos, M., van Schaik, R., Sansone, S.-A., Schultes, E., Sengstag, T., Slater, T., Strawn, G., Swertz, M.A., Thompson, M., van der Lei, J., van Mulligen, E., Velterop, J., Waagmeester, A., Wittenburg, P., Wolstencroft, K., Zhao, J., Mons, B., 2016. The FAIR Guiding Principles for scientific data management and stewardship. Sci Data 3, 160018.

Wilson, N., Greenberg, J., Jumpasut, A., Collison, A., 2017. In-Orbit Radiometric Calibration of the Planet Dove Constellation.

Xia, L., 1998. Measurement of rapid agricultural land loss in the Pearl River Delta with the integration of remote sensing and GIS. Environment and Planning B: Planning and Design 25, 447–461.

Xu, Y.J., Wu, K., 2006. Seasonality and interannual variability of freshwater inflow to a large oligohaline estuary in the Northern Gulf of Mexico. Estuarine, Coastal and Shelf Science 68, 619–626.

Zenodo, 2016. Zenodo.

Zhang, D., Wang, J., Zhang, Y., 2013. Hard and soft classification method of multi-spectral remote sensing image based on adaptive thresholds. Spectroscopy and Spectral Analysis 33, 1038–1042.

Zhang, H.K., Roy, D.P., Yan, L., Li, Z., Huang, H., Vermote, E., Skakun, S., Roger, J.-C., 2018. Characterization of Sentinel-2A and Landsat-8 top of atmosphere, surface, and nadir BRDF adjusted reflectance and NDVI differences. Remote Sensing of Environment 215, 482–494. https://doi.org/10.1016/j.rse.2018.04.031

Chapter 4

Title: Urban Flood Vulnerability in Belém, Brazil: Application of Adjusted Vulnerability Index using Multilayer Geo-constrained Networks

Authors: Samapriya Roy[1], Landon Yoder[2], Vitor M. Dias[3] and Eduardo Brondizio[4]

[1]Department of Geography, Indiana University, Bloomington, [2]Indiana School of Public and Environmental Affairs, Indiana University, Bloomington, [3]Indiana Department of Sociology, Indiana University, Bloomington, [4]Indiana Department of Anthropology, Indiana University, Bloomington, Indiana

Corresponding author: *Samapriya Roy, email: roysam@iu.edu*

Abstract

Deltas are among some of the most vulnerable areas in the world: facing constant threats from flooding, degradation, and land loss. With an annual population growth rate of 1.59%, exceeding the world growth rate of 1.11%, deltas also house some of the most vulnerable populations in the world. We here introduce a spatial measure of urban residents vulnerability to flooding, an adjusted vulnerability index (AVI) that builds upon a vulnerability index previously published in Regional Environmental Change (Mansur et al. 2017). The AVI includes indicators related to flood exposure, socioeconomic sensitivity, and infrastructure. This vulnerability index was used to analyze flood risk and urban flood vulnerability in Belém across 1,265 census sectors and 52 neighborhoods (also called Bairros). We wanted to understand the effect of spatial interactions and networks on vulnerability across these census sectors and neighborhoods. This paper 1) introduces a novel method to couple spatial and

temporal vulnerability indices based on vulnerability indicator variables and 2) incorporates this with higher resolution indicators of urban vulnerability. The spatially adjusted vulnerability index uses a multilayer network analysis tied with a local indicator of spatial autocorrelation to look at spatial dispersion and aggregation. We find that 51% of census sectors have a high or very high vulnerability. We also analyzed vulnerability within and outside the areas considered 'subnormal agglomeration' with unplanned settlements by the Brazilian Institute of Geography and Statistics (IBGE) and proxy variables that are critical to understanding flood risks. Areas with unplanned settlements seem to be most affected by urban flooding and face increasing urbanization and housing unit density. We found that channelization across the city, along with failing infrastructure, has further led to an overall increase in flood exposure experienced by people living in Belém. Finally, our analyses further calculated a mean vulnerability index at the level of neighborhoods or bairros to analyze the effect of spatial aggregations. Our results show that spatial vulnerability is spatially clustered and mostly effected by both biophysical and socio-economic factors and planned and unplanned settlements experience varying nature of emergent vulnerability. Our analyses may serve as a template for spatial and temporal integration of vulnerability measures in urban deltaic environments and urban areas at large.
Keywords: Delta, Vulnerability, Network analysis, Multilayer, Urban flooding

4.1 Introduction

It is estimated that over half a billion people depend directly or indirectly on delta environments worldwide (Syvitski et al. 2009; Renaud and Kuenzer 2012). During the past decade, 85% of the world's deltas experienced severe flooding (Syvitski et al. 2009), which is likely to increase in severity and frequency within this century owing to sea level rise and climate change (Syvitski et al. 2009; Newton et al. 2012; Renaud and Kuenzer 2012). Deltas are among the most productive, dynamic, and fragile ecosystems, but account for less than 3% of land globally. Human population densities in deltas are 12 times higher than the global average, and growth rates in deltas (1.59%) also currently outpace the global average (1.11%). In the Global South, fast-growing urban areas in deltaic regions are confronting the compounding impacts of environmental change and sea-level-rise, deficient infrastructure, and unequal socioeconomic conditions, which together place large sectors of the population in vulnerable settings. As such, deltas social-ecological systems are considered not only sentinels of change but emblematic of the complex interactions of accelerated environmental and social change (Brondizio et al. 2016). Despite the importance of urban spatial structure on residents' vulnerability to flooding, few studies on vulnerability have incorporated spatial analysis into their models. Given these trends, this study will examine how accounting for biophysical, socioeconomic, and infrastructural factors, jointly shape urban vulnerability and highlight the underlying implications of an urban population subjected to flooding.

Vulnerability, as measured in urban environments such as cities found along deltas, is a function of the spatial structure of cities (e.g., housing patterns and conditions, available infrastructure and its maintenance), socioeconomic conditions across different spatial units (e.g., city block, census sector, neighborhoods, city level, etc), local topography and hydrology, and other interacting factors, which have a crucial role in mediating or enhancing the effect of hazards. In this study, we analyze the vulnerability to flooding of residents in Belém, Brazil, the largest city of the Brazilian Amazon. The city of Belem and the Belem Metropolitan Region accounts for 50% and 67 %, respectively, of the total population of the Amazon Delta Estuary (ADE) region, which includes other 49 cities, mostly small. Belem's life is intertwined with the marked pulses of semi-diurnal tides. Belem is characterized by a large low-income population, living in unplanned urban settlements created through phases of accelerated expansion (often along streams), unequal distribution or absence of drainage infrastructure, and subjected to increasingly recurrent flooding. These conditions and the availability of data make it a microcosm for measuring and testing effects of spatial dependence and networks on overall flood vulnerability models.

Cities in the global south present a unique perspective on urban growth and are often overlooked in their particularities and challenges (Nagendra et al. 2018). Belém is also an interesting case study as it encapsulates the amalgamation of poorly planned urban infrastructure, high population density, and marked economic disparities. Urban population in the ADE region as a whole has grown "by around 300%, particularly between 1970 and 2010", in most cases in urban areas without the means to manage and provide services to such rate of growth (Brondizio et al. 2016). The case of Belem offers an opportunity to incorporate the analysis on the possible role of urban spatial structure in levels of vulnerability to flooding.

In a prior study (Mansur et al. 2016), we applied vulnerability modeling by introducing the Analytic Hierarchy Process (AHP) (Saaty 1987, 2008, 2013; Vargas 1990) to 41 urban areas of various population sizes across the ADE. Our analyses introduced a multiscale model for looking at vulnerability indicator variables and also integrated multiple vulnerability types into a single combined vulnerability index. While the approach used in (Mansur et al. 2016) is novel in weighting vulnerability contributions, the overall analysis did not take into account spatial effects, dependencies, or dispersions. Therefore, we here introduce a multilayer network analysis (hereafter 'multilayer analysis') to account for spatial distribution and dependence while also calculating vulnerability indices. We model spatial dependence using Local Indicator of Spatial Autocorrelation (LISA), which was applied to each indicator variable (Cliff and Ord 1970; Anselin 1995; Cheng et al. 2012), and each network formed by an indicator variable then forms the multilayer network. By using land use and land cover datasets along with building rooftop data and drainage channel length, this paper advances the analysis of vulnerability risks from the level of census sectors (smallest publically available unit of analysis), neighborhoods, and the entire city, including areas designated as ‘subnormal agglomerations’, which corresponds to 40% of the city area with over 38% of the overall population.

Building upon Mansur et al. (2017), the AHP approach used in this analysis allows us to integrate spatial network and dependencies using network analysis (Saaty 1987, 2008, 2013; Vargas 1990). Through this approach, we investigate the following three questions: i) How do changes in urban growth and infrastructure affect the spatial distribution of vulnerability? ii) Does overall vulnerability vary spatially across census sectors and neighborhoods (bairros)? iii) How do proxy indicators of flood vulnerability inform the combined vulnerability index?

4.1.1 Conceptual models of vulnerability

Vulnerability is broadly defined as the risk populations face and/or their inability of to cope with hazards (Mitchell and Mitchell 1996; Mitchell 1999), where hazards are socio-ecological forces capable of causing physical as well as psychological and emotional harm (Kelly and Adger 2000; White et al. 2001; Brooks 2003; Hurst 2008; Adger and Kelly 2012). Vulnerability is comprised of biophysical exposure and socioeconomic susceptibility (also known as ‘sensitivity’ in the vulnerability literature) to a natural hazard (Brooks 2003; Turner et al. 2003). For example, low-lying areas are highly exposed to flooding, but residents in these areas can have vastly different levels of susceptibility to flooding based on whether their municipality has fortified the shoreline with a high seawall or not, or whether they have socioeconomic conditions and/or an extensive network of family or friends to provide support, such as lodging, subsistence, and empathy.

Though many previous models of quantitative vulnerability used estimates of hazards, many neglected to incorporate spatial weighting into their overall assignment of vulnerability. (Balica et al. 2009, 2012; Overeem and Brakenridge 2009; Adger and Kelly 2012) A-spatial measures of vulnerability do not take into consideration local spatial clustering. The role of the spatial structure of these systems is likely understated in these spatially agnostic models. Models, such as the Delta Socio-Ecological System (SES) framework (Sebesvari et al. 2016), take into account system robustness and measures susceptibility of a system. Such models include susceptibility to risks both inside and outside an SES and further proposes hazards and impacts of these hazards at different social scales within the SES. However, spatial setup and interaction among these spatial and social units are not explicit in the SES Framework but remains critical to urban systems. While there is extensive literature on vulnerability, the process of integrating spatial morphology and structure and its use in vulnerability models are still developing (Kelly and Adger 2000; Brouwer et al. 2007; Adger and Kelly 2012).

While place-based vulnerability models, such as the one proposed by (Cutter 1996; Rashed et al. 2007; O'Brien and Wolf 2010), incorporate geographic context, they do not account for the spatial configuration of the system, and, in turn, how such configuration may effect, enhancing or mitigating, different socio-economic-environmental contexts. Incorporating spatial components in hazard sensitivity analysis and vulnerability models is particularly important, given the singularities of urban socio-spatial configurations around the world. This notion of hazard mitigation is also informed opportunities and challenges for collective, adaptive social capacity in spatial networks amongst different sectors and neighborhoods in urban areas (Cardona 2011, 2013; Nishat and Mukherjee 2013). For example, during times of frequent urban flooding, people often stay or live with friends and families to avoid dealing with short-term weather uncertainty (Lima 2001; Costa and Brondízio 2011; Pegado et al. 2012b; Mansur et al. 2018). Earlier research by others in the field has further pointed to how collective mitigation in spatial units, such as neighborhoods, increases an individual's ability to cope with hazards (Swift 1989; Burton 1997; Adger and Kelly 1999, 2012).

4.1.2 Natural and Anthropogenic Drivers of Flooding in Belem

Belém is located in the northern Brazilian state of Pará. The city is positioned in the floodplain of the southern branch of the ADE, specifically on the edge of the Guajará Bay and the Guamá river mouth, in the Para River Estuary (Figure 4.1). Topographically, about 40% of the city is below sea level (Pegado et al. 2012a). Semi-diurnal tides and seasonal floods influence the floodplain, the latter influenced by rain regimes in the region and elsewhere in the basin (Guedes et al. 2009; Costa and Brondízio 2011; Pegado et al. 2012a). Also, the majority of the river channels in Belém are degraded and its riverbanks disorderly occupied, aggravating the severity of floods in the city (Gilbert 1998; Perz 2000; Pegado et al. 2012a).

Consequently, projected sea-level rise and enhanced human pressures in the city are likely to continue to exacerbate flood impacts in this region (Newton et al. 2012; Pegado et al. 2012a; Tessler et al. 2015). The city has a substantial portion of unplanned housing developments or informal settlements, many in low-lying areas called '*baixadas*.' However, recent evidence from a case study of Belém shows that rainfall and high tides do not need to coincide for floods and inundation to happen, even though tidal level still influences these events (Santos and Rocha 2014:44). This pattern stems, at least partially, from the fact that the majority of the river channels in Belém are degraded, with a high degree of sedimentation, and many choked with garbage, aggravating the severity of floods in the city (Gilbert 1998; Perz 2000; Pegado et al. 2012a).

Following the urbanization policies from the beginning of the twentieth century, Belém's policy-makers have attempted to rectified and controlled the streams in the city connected to the Guajará Bay, such as when implementing the channel system to drain water and sanitary waste (Dias and Dias 2007; Brondizio et al. 2016; Soares et al. 2018). Urban expansion in Belem started during the early 1970s along with changes promoted in the Amazon region as a whole by centralized development programs. As a significant part of urban expansion in Belem has been marked predominantly by low-income residents, occupation occurred in available and less regulated low-lying spaces, which provided access to water and resources. As such, at least in part, urban expansion of floodplain and upland areas occurred along with socioeconomic differences. Progressively, Belem has expanded away from its main water-front, as expressed by locals, "Belém has turned its back to the river" (Dias and Dias 2007; Ponte 2015).

The population of Belém increased to nearly 1.5 million, and its metropolitan area to 2.5 million in 2010 (IBGE 2010). Most of this growth has been fueled by unplanned growth in informal settlements. In 2002, the overall unplanned settlement reached 40% of the municipality of Belém and accounted for over 38% of the overall population (Pegado et al. 2012a). By 2010, unplanned settlements comprised over 50 percent of Belém's population. Furthermore, 90 percent of the city's households are not connected to the sewage system (Lima 2001; Mansur et al. 2016, 2017). Belém encapsulates the idea of the Amazon as an "urbanized forest," with urban problems that are common to many cities throughout the global south (Padoch et al. 2008, 2014; Pinedo-Vasquez and Padoch 2009).

At the same time, Belem has received significant investments in urban drainage infrastructure. Over 300 million USD has been invested in micro- and macro-drainage projects since the 1980s, which have created new spaces for the city to grow, but with mixed results that stem from the poor implementation, site suitability, and maintenance of these infrastructure projects (Mansur et al. 2017). These drainage projects today crisscrossing the city, but continue to be poorly maintained, and in parts are unfinished. These channels thereby contribute to flooding, often unpredictably, and increasingly independently from tidal influence (Pegado et al. 2012a, b; Mansur et al. 2017). This pattern of urban growth has also increased overall impervious areas, which in turn are contributing to worsened flooding in the city (Ponte and Brandao; Pegado et al. 2012a; Mansur et al. 2016).

The impact of sea-level rise in Belem's is still unknown, but evidence suggests that it is already affecting tidal levels, salinity, and potentially already exacerbating urban and rural flooding levels (Vogt et al. 2016). Over 40% of the area is below the sea level during high tide (mean high tidal heights of over 3.72 m). Belém is prone to the tidal movement of water in and out of the city through these drainage channels discussed earlier. Increasing amounts of impervious surfaces in Belem compound the flood risks created by rising sea levels (Barnett 2003; Barnett and Adger 2007). Since a large portion of the city is below the sea level, drainage channels and the rivers retain and cause rapid urban flooding. Low lying areas with higher population densities and with unplanned settlements such as houses on stilts are further prone to flood damage, including the combined impacts of flooding and sewage spills. Tidal backflows and reduction in channel capacity over the years have further lead to increased flooding (Tucci 2002; Fewtrell et al. 2008; Pegado et al. 2012b; Filizola et al. 2014). Over time, these drainage channels which crosscut the entire city act as river flood zones submerging more area rather than acting as conduits to allow for free passage of water out of the city.

4.2 Materials and Methods

We use the census sector as our spatial unit of analysis because it is the finest level at which population data were publicly available. Though finer level datasets are available, most of them are restricted by access and restricted for publication. The Brazilian Institute of Geography and Statistics (IBGE) tracks 'unplanned settlements' (categorized as "subnormal agglomerations") in both census sectors and larger neighborhoods, called Bairros, which often consist of multiple census sectors. These unplanned settlements reflect economically vulnerable populations and poorly constructed dwelling, both of which are likely to increase resident's susceptibility to hazards. Our study areas consist of 1,265 census sectors, out of which 679 of them were classified as unplanned settlements, and these 1,265 sectors lie with 52 total Bairros (Figure 4.1). It is important to note that Bairros do not have any administrative boundary and legal powers regarding territorial functions. However, community ties and relationships among census sectors are often formed within these neighborhoods, and public services are often planned at the neighborhood level.

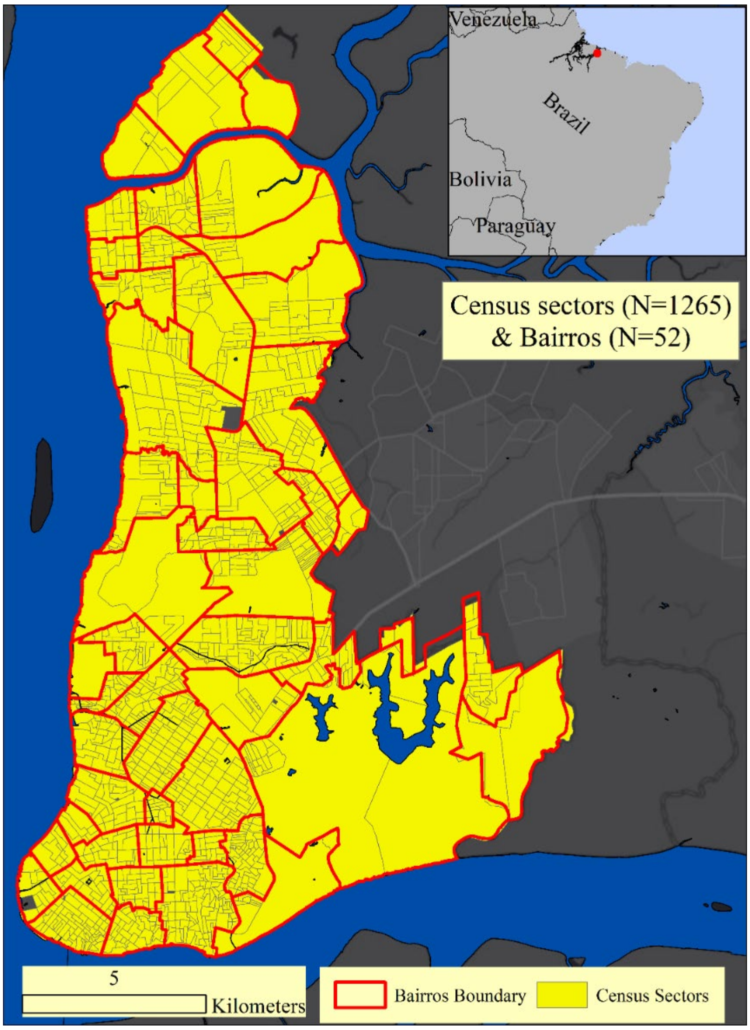

Figure 4.1: Spatial units set up within Belém, Brazil

For our study, though the analysis was performed at the level of census sectors, the results were further subdivided into census sectors that are planned and unplanned. To get at the aggregated values of vulnerability for Bairros, the vulnerability index value of these neighborhoods was calculated as a mean value for the census sectors that lie within each of these bairros.

We divide our datasets into 1) core data for measuring overall vulnerability (Mansur et al. 2016) and 2) data focused on spatial configurations and flooding. For generating the Adjusted Vulnerability Index (AVI), we create a spatial network for which we take a subset of the core variables that are historically relevant towards establishing urban flooding and associated vulnerability (Pegado et al. 2012b; Mansur et al. 2016). We treat each census sector as a node, meaning we have a fixed number of nodes (n=1,265) for every attribute. The introduced model measures the network model measures the spatial interaction between fixed actors (census sectors) and the overall interaction among sectors.

4.2.1 Datasets and Derivatives

The study consists of a range of datasets that are made available from our earlier work (Table 4.1; (Mansur et al. 2016), Brazilian government agencies, sensor-based platforms documenting urban growth and tidal dynamics, and fieldwork.

Table 4.1: Indicator variables adapted from Mansur et al. 2016, these are also used for the development of the adjusted vulnerability index

Dimension	Indicator group	Indicators
Exposure	Flood risk exposure	Population under risk of flooding
		The area under risk of flooding
Socio-economic sensitivity	Household income	No income and income less than one minimum wage
		Income less than five and more than one minimum wage
	Population age groups	Children (<10 years old) and elderly (>65 years old)
	Location	Population living in unplanned settlements
Infrastructure	Sanitation services	Households with public water supply

		Households served by solid waste collection
		Households with domestic effluent piped to a sewer system
	Housing conditions	Households without a drainage system
		Households with accumulating solid waste in front of the house
		Households with an incidence of open-air sewage
		The area considered unplanned settlement

Additional datasets were either generated or collected from multiple sources and are reported below. Each derivative dataset was shared as supplementary material for the analysis. Additional data sets were gathered from national and local government agencies (Table 4.2), including the high resolution 200-by-200 m grid of urban areas with a count of the number of households from IBGE, rooftop count provided by COHAB (i.e., the Popular Housing Company), additional datasets (Table 4.2) and in-situ field measurements (collected by the third author) of channel's width, length, and slope based. In sum, we have all the elements to measure flow capacity of these channels. Thus, using the in-situ field data, we add another layer to the overall assessment of vulnerability.

The third author and a geography-major undergraduate research assistant (RA) are both from Belém, carried out fieldwork in different parts of the city, and extensively discussed which sample of channels could furnish reliable, though approximate, indicators about the situation of the drainage capacity in the city. Field interviews conducted by authors (Figure 4.2) were used to establish flooding timeline and recurrence (supplemental interview). They also met with the co-author of a recent case study of Belém who adopted a similar approach to obtaining his measures to talk about these plans (dos Santos and da Rocha 2014). No concerns were expressed in regards to our methodological choice. Thus, we selected the *Canal das Docas* and *Canal da Tamandaré* to conduct in-situ measurements, which are two channels in relatively good conditions regarding their flow capacity for comparison with poorly maintained channels in the city. (These channels are also located in neighborhoods where income is above the average, which should arguably garner more attention from, and maintenance by, public officials than poorer parts of the city.)

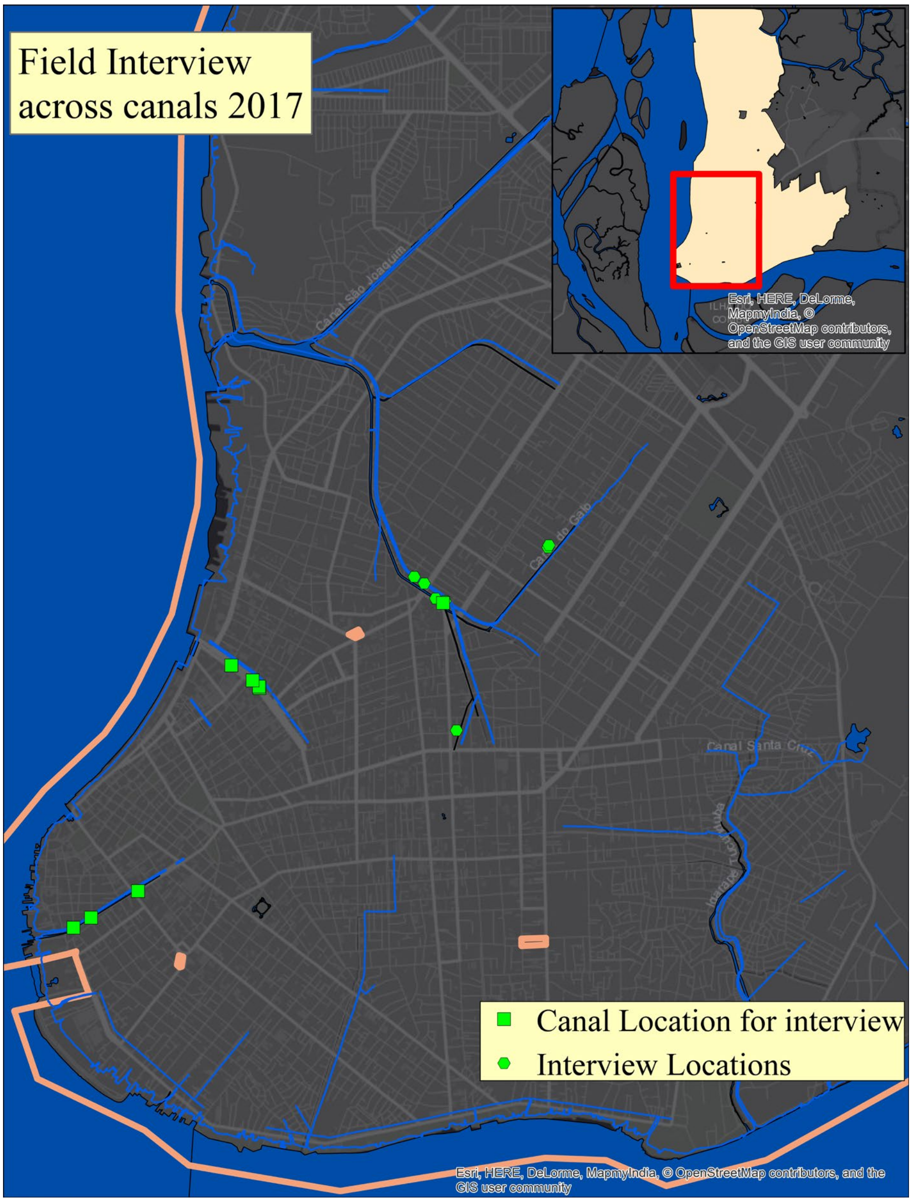

Figure 4.2 Locations of canals chosen for an interview and actual interview locations for field work

These datasets were coupled with additional datasets such as elevation map to ascertain low lying areas and certain points with high flood frequencies to be overlaid with the inundation risk mask provided by COSANPA. On this point, the researcher with whom the third author and the RA spoke explained that he was not certain about the methodology that COSANPA used to calculate and then validate its inundation risk indicators, but he was familiar with these shapefiles.

Since this scholar was focusing on a case study within Belém to validate other measures used in his article (dos Santos and da Rocha 2014) and not the entire city, he decided to collect his data on inundation, an analysis on which we expand using COSANPA's files that extend to Belém's territory.

Table 4.2: Datasets and institutional dataset providers

Dataset	**Institutional Provider**
Census 2010	*IBGE (Brazilian Institute of Geography and Statistics - Instituto Brasileiro de Geografia e Estatística in Portuguese)*
Rooftop data	*COHAB (Popular Housing Company - Companhia para Habitação Popular in Portuguese)*
Permeability layer	*COSANPA (Company of Sewage of Pará - Companhia de Saneamento do Pará in Portuguese)*
Inundation risk layer	*COSANPA (Company of Sewage of Pará - Companhia de Saneamento do Pará in Portuguese)*
Contour Data	*CODEM (Company for the Development and Management of the Metropolitan Area of Belém - Companhia de Desenvolvimento e Administração da Área Metropolitana de Belém in Portuguese)*
River Network	*COHAB (Popular Housing Company - Companhia para Habitação Popular in Portuguese)*
Land Use and Land Cover	Derived using Landsat and High Res IKONOS, WV2 data
Tidal Height, Temperature and Precipitation	XTIDE and CHIRPS (Climate Hazards Group Infrared Precipitation with Station Data)
Digital Elevation Model	Contour lines used to derive elevation surface with a 10m resolution

4.2.2 Land use and Land Cover Change Analysis

We used Landsat 5, 7, and 8 datasets to generate land use and land cover over Belém, using the Normalized Difference Built Index (NDBI) and the Normalized Difference Vegetation Index (NDVI). These indices were produced for both planned and unplanned settlements over time to compare the overall growth in the city to the growth in the unplanned settlements. High-resolution satellite imagery about 2-3 m was also utilized to get at the classification of land use and land cover looking at finer details such as overall growth in the impervious area. The analysis was performed in Google Earth Engine (Gorelick et al. 2017; Shelestov et al. 2017), and the results were included in the supplementary materials. Land use and land cover analysis were performed on Landsat imagery with every 5-year collections from 1990 onwards. A total of 565 Landsat images were used to create 5-year composites and a Normalized Difference Built Index (NDBI) was used in conjunction with Normalized Difference Vegetation Index (NDVI) and Normalized Difference Water Index (NDWI) to act as overlaying masks (Otsu 1979; Gao 1996; Zha et al. 2003; Roberts et al. 2017). NDBI highlight urban areas where there is higher reflectance in the shortwave infrared band compared to the near infrared band.

$$NDBI = \frac{SWIR - NIR}{SWIR + NIR} \quad NDVI = \frac{NIR - RED}{NIR + RED} \quad NDWI = \frac{NIR - SWIR}{NIR + SWIR}$$

NDBI is used in conjunction with NDVI, which highlights vegetation, and NDWI, which highlights water. NDVI and NDWI are used as masks to exclude areas with vegetation and water and focus on urban and built areas using the NDBI.

Once the NDBI image was generated, we used Otsu’s thresholding method (Otsu 1979) to binarize each pixel in the image as urban and non-urban areas. Otsu’s analysis looks at thresholding value to minimize within class variance and generates a single threshold value for each single band NDBI image. This was applied to each NDBI generated from the imagery composites over six, 5-yr periods, with the last period extending from 2015-present., High-resolution multispectral images (IKONOS, WV-1, and WV-2) were acquired from Digital Globe (2.5m resolution) from three different periods (i.e., 2011, 2013, and 2015) to estimate urban built area. These images, however, had swath widths that were usually smaller than the overall area of interest and as a result, the reported results were only included for those census sectors which had complete coverage (581 out of the 679 census sectors that constitute the unplanned settlements). The endmembers were collected for the high-resolution imagery and constrained spectral un-mixing was applied to the imagery to get the urban built class, along with water, road, and vegetation. This subpixel classification allowed for the calculation of percentage urban area along with vegetation and water class for the multiband imageries (Keshava and Mustard 2002; Keshava 2003). Our spectral unmixing from the linear mixing model (LMM) where we have *M* endmembers:

$$x = \sum_{i=1}^{M} a_i s_i + w = Sa + w$$

Where x is the L by 1 received spectrum vector, and S is the L by M matrix formed by the L by M matrix, a is the fractional abundance (M by 1 matrix), and w is the L by additive observation noise vector (Keshava and Mustard 2002). However, since we are interested in the urban built environment apart from the overall urban area, this band with percentage probability per pixel was extracted and was coupled with interclass clustering using Otsu's method similar to that applied to NDBI in Landsat imagery, and the results were reported. The analysis was made for the unplanned settlements since they had nearly complete overlap over our classified area for the high-resolution imagery.

4.2.3 Tidal and Precipitation Data

Tidal data was collected from a tide gauge at 1.4333° S, 48.5000° W, and also generated from tide tables and XTide (Flater 1996, 1998). To get yearly tidal high and low tide heights, we used a Python program to scrape and parse tabular daily data from 2000-2018. This dataset had a daily resolution with 3 data points each day for 18 years and had been included in the supplement for use in assessing sudden peaks in daily tidal height data. Highest observed high tide values were about 3.94 m observed in August 2012 and again in August 2016 and these were also coupled with the highest observed low tide values of 1.37 to 1.34 m observed in 2012 and 2016 respectively. Rainfall data were reported from earlier literature (Pegado et al. 2012b; Mansur et al. 2016) and were verified using CHIRPS (Climate Hazards Group Infrared Precipitation with Station Data), which provides quasi-global precipitation data from 1981 onwards (López-Carr et al. 2014; Funk et al. 2015; Katsanos et al. 2016). The average value of over 2000 mm and nearly 3000 mm was verified for 2000-2018 as well, and an average precipitation value was derived for each year. The highest values were 3200 mm approximately in 2011 and with a high peak of about 3112 mm in 2017. Highest temperature data similarly followed suit with over 33 C temperature recorded in 2011 and 2016.

4.2.4 Rooftop, Contour and Elevation Data

Contour Data was provided using a land-based contour survey. These points were converted into contour lines, and a Triangular Irregular Network (TIN) was then used to create a DEM surface interpolated to 10m resolution. Zonal statistics were calculated for each census sector to get mean elevation and this was used as an underlying layer for analysis of the inundation maps and points of historic flooding.

Rooftops were vectorized and provided as a vector file, this included edits and check from Open Street Map. Rooftop counts are an indicator of the number of houses and serve as a proxy to urbanization as a process. However, differentiating rooftops are harder to delineate in areas with unplanned growth owing to connected rooftop structures and building rooftop material making count and delineation harder. Nevertheless, they serve as direct indicators of urbanization and indirect indicators of population and urban growth.

4.2.5 Spatial Multilayer Network setup

For our study, we divided the problem into two main components i) Building a single spatial network consisting of multiple layers where each vulnerability variable is a layer in the multilayer spatial network and ii) Collapsing the multilayer network into a single layer multi-attribute network. The methodology (Figure 4.4) consists of the following steps i) An analytical hierarchical process (AHP) was coupled with Shannon's entropy (Shannon 1948; Lin 1991; Martín and Rey 2000) to create a combined entropy metric (CEM). ii) Our method established a hierarchy between different variables or attributes in the multilayer network which explains overall vulnerability to flooding.

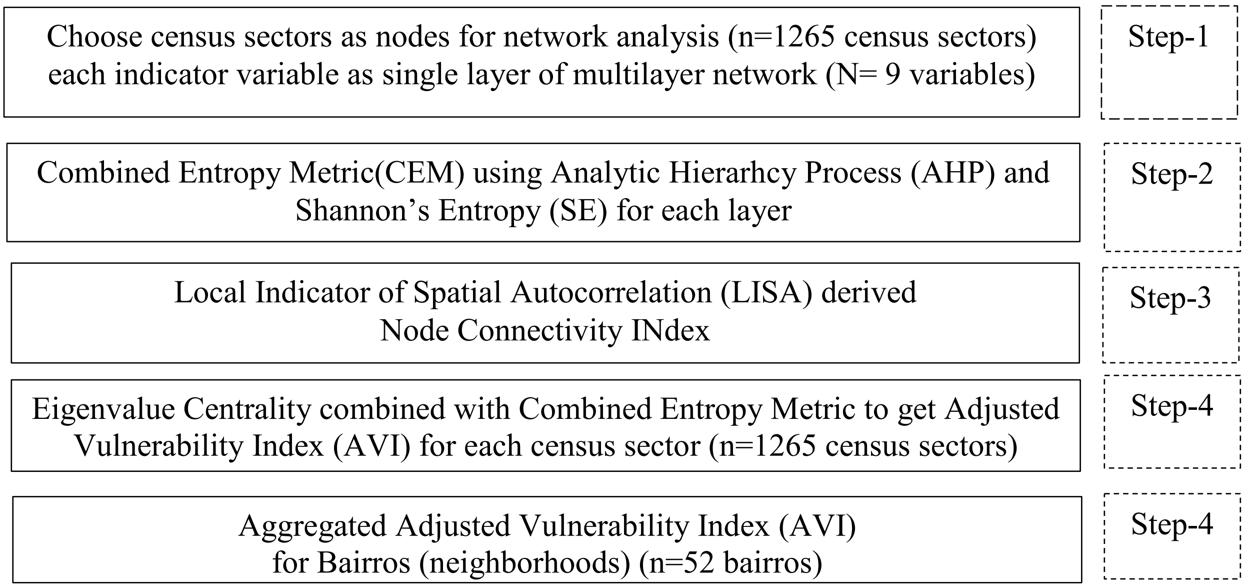

Figure 4.4: Overall Methodology for Calculating Multilayer System Vulnerability

Since the network is spatially situated within the spatial morphology of the city, a Local Indicator of Spatial Autocorrelation (LISA) was applied (Anselin 1995; Fluet-Chouinard et al. 2015), and a network Eigenvalue centrality was then calculated and combined with CEM to generate adjusted vulnerability index (AVI). Additional analysis and data models are integrated into this to help assess urban flooding and change in the spatial configuration of the city both spatially and temporally. Our methodology is described further in the following subsections. Reassessing vulnerability with the help of a network analysis allows for a new dimension at looking at how vulnerabilities interact spatially. The Analytic Hierarchical Process (AHP) used to generate weights is limited by the fact that the pairwise comparisons used in AHP do not consider spatial dispersion and effects. In this paper, these spatial effects are utilized and applied using the network analysis to yield a spatially adjusted vulnerability index (AVI).

4.2.6 AHP Based Pairwise Comparison

AHP is a decision-making tool that allows the user to perform a pairwise comparison and reduce a multidimensional hierarchy between the variables to a single decision (Saaty 1987, 2008, 2013; Vargas 1990). In the process, AHP established a list of priorities for each variable, which then affects the overall outcome. The pairwise comparison between each variable was transferred to a matrix in the form (Figure 4.4 & 4.5). We used the analytic hierarchical processing (Zahedi 1986; Saaty 1987, 2008) method to generate priority eigenvector among the variables that were analyzed for analysis of urban flood vulnerability.

The AHP analysis was applied to the same subset of indicator variable groups (Figure 4.3) which was adopted from the earlier paper (Mansur et al. 2016). The final goal was to establish a net hierarchy between indicator groups and variables, and grouped into three different categories: i) exposure indicator variables; ii) socio-economic sensitivity indicators, and iii) infrastructure indicator variables. A matrix and pairwise comparison was set up using the correlation coefficient for each variable and was then converted using Saaty's Scale (Saaty 1987, 2008, 2013; Vargas 1990). The overall hierarchy is useful for establishing the importance of each variable among the multiple layers of the Multilayer networks.

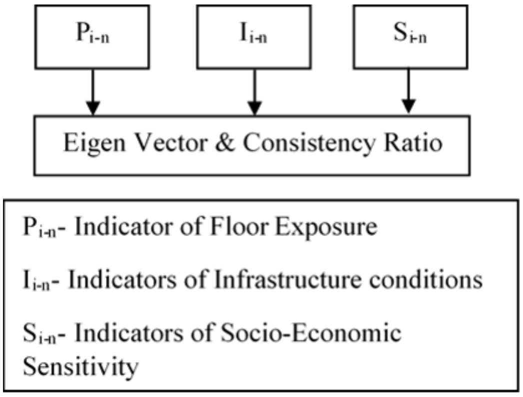

Figure 4.5: Modified from Mansur et al. 2016

The weights depend on the size of the matrix (n by n). A consistency ratio (CR) was calculated to make sure that the matrix values and established hierarchies are close to being consistent. While randomness index was fixed depending on the number of variables (n), so we calculate CR as the ratio of consistency index by randomness index. The eigenvector was then finally calculated, and the consistency ratio using the randomness index and this establishes an overall hierarchy among layers in the multi-layer network. Since the number of census sectors is the same for each variable, our methodology allowed us to establish a varying level of hierarchy measure among different layers. In this case, the vulnerability weight was used as a measure that is coupled with spatial heterogeneity.

4.2.7 Spatial Constraints to Hierarchical Network Data

Shannon's Entropy (SE) (Shannon 1948; Hill 1973; Martín and Rey 2000) was applied (Equation 1) to address the spatial heterogeneity of each variable. Where H_n is SE value,

$$H_n = -\sum P_i log_e(P_i)$$

Where,

P_i = proportion of variable in the zone/sector

n = Total number of zones

In this case, zone/sector refers to the census sector, which is used instead of nodes. A python program was written (Supplementary Code) to calculate SE for each variable. SE measures the spatial dispersion of indicator variables. The higher the SE, the higher the overall spatial heterogeneity of the values between indicator variables. Of the proportion of value in the zone/sector, SE has been used in earlier studies to get at spatial distribution and heterogeneity (Krstanovic and Singh 1992a, b; Bhatta et al. 2010) among use cases in urban processes. While AHP produced among variable hierarchy or measure of weight between among two or more indicator variables, SE provides within-group distribution or variability of the variable values. Combining AHP and SE allows us to utilize both within- and between-group ranking and variability measures across the Multilayer network and as such, combines spatial effects to weight wise hierarchy. This is the Combined Entropy Metric, as discussed in the succeeding sections.

4.2.8 Combined Entropy Metric

While AHP is a robust method to generate an overall hierarchy between indicator variable, Shannon's entropy (SE) established the spatial spread and dispersion measured by the entropy value. As such the combined entropy metric (CEM) is the normalized value or the product of AHP and SE per variable and was calculated for all variables after confirming that they are consistent using the value of Consistency Ratio (CR) we calculated earlier. Since the value of Shannon's entropy can range from 0 to infinity, the normalization approach used to calculate CEM also allows us to make sure that we maintain the overall sum of CEM equals one. These values were then used as a weight for the directed network graph in the multilayer network (Table 4.3). This step allows us to attach spatial dispersion and distribution characteristics to the existing AHP metric.

$$Combined\ Entropy\ Metric(CEM) = \frac{AHP\ x\ SE}{\sum AHP\ x\ SE}$$

Where,

AHP= Eigenvector value from the AHP (for variable i) and SE= Shannon's Entropy value (for variable i).

Table 4.3. The table shows AHP, spatial entropy, and combined entropy metric

Indicator Variable	AHP	SE	CEM
Percentage Population at risk	0.25	10.25	0.29
Income less than recommended	0.20	10.30	0.23
No Income	0.18	10.30	0.21
Open Air Sewage	0.11	4.55	0.07
Household without Drainage	0.07	7.76	0.07
Accumulated Solid Wastes	0.06	8.66	0.06
Access to Sewers	0.05	4.08	0.04
Solid Waste	0.03	10.10	0.02
Water Supply	0.01	9.69	0.02

The normalized CEM was used as a weight which could be applied to the setup of the overall multilayer network. Since Shannon's entropy is a combined measure of dispersion, this is a single measure for each indicator variable, however, to get at the spatial dynamics and interactions of the census sectors a spatial autocorrelation measure such as the Local Indicator of Spatial Autocorrelation (LISA) becomes necessary.

4.2.9 LISA and the Node Connectivity Index

Local Indicator of Spatial Autocorrelation (LISA) has been effectively used to measure the impact of neighborhood processes and spatial pattern on each other and to capture if spatial clustering is a sign of spatial dependencies. Spatial Autocorrelation broadly examines the spatial dependency of data where observations closer to each other are more similar to each other (positive autocorrelation) or dissimilar (negative autocorrelation). It is, therefore, a measure of the spatial distance between the observation and the similarity between them in values. However global measures of spatial autocorrelation like Moran's I have problems with generating only a single measure of autocorrelation for the whole system because it relies on an assumption of spatial stationarity (i.e., that system-wide phenomena are consistent everywhere). Spatial stationarity principles have been challenged, and local variations, such as geographically weighted regression, have been suggested as preferable to handle issues with spatial stationarity (Fotheringham et al. 1998; Fotheringham 2009). Local models, such as Local Indicator of Spatial Autocorrelation (LISA), measures spatial clustering and establishes a spatial autocorrelation index value and a cluster for each variable relation (positive, negative and non-significant autocorrelation). The sum of LISAs for the entire landscape is proportional to the Global Moran's I, which allows for cross-checking between local and global autocorrelation indices. We used Local Indicator of Spatial Autocorrelation(LISA) instead of Global Moran's I for our analysis to overcome the problems of structural homogeneity and to better understand local interactions at the relevant scale of the spatial processes.

$$I_i = z_i \sum_j w_{ij} \, z_j$$

Here z_i is the original variable (SI in this paper) in standardized or deviation from, w_{ij} is the spatial weight, with the summation being across row i of the spatial weights matrix. The analysis generates cluster types or outlier types which represent the behavior of each pixel to its neighbors (Cliff and Ord 1970; Anselin 1995; Ord and Getis 1995, 2001; Wulder and Boots 1998; Fluet-Chouinard et al. 2015). The analysis generates cluster types or outlier types that represent the behavior of each node in the network about their neighbors. Within each single attribute layer, we use LISA to divide nodes into five different classes (High-High, High-Low, Low-High, and Low-Low autocorrelated nodes, and Non-Significant nodes, which can be treated as isolated. The total number of nodes of a single class equaled the total number of possible connections that a node could make, however, each class can only be connected to spatially contiguous neighborhoods and hence geospatially constrained. This ratio of actual connections that each node has to the maximum possible number of connections possible was constructed as Node Connectivity Index (NC_i)

$$NC_i = \frac{Total\ number\ of\ connected\ nodes\ in\ each\ cluster}{Total\ number\ of\ Class\ nodes\ or\ possible\ connections}$$

This allowed us to develop a multiclass multilayer directed network, which was then analyzed for network metrics and more specifically, Eigenvalue centrality measures. Local Indicator of Spatial Autocorrelation allows the user to generate five classes of node types to be used in the network analysis. These are the clustering types denoting positive, negative, and statistically insignificant autocorrelation. Both positive and negative autocorrelations were used to maintain a consistent number of nodes and connectivity in the urban area; this includes keeping non-significant sectors as isolated nodes.

4.2.10 Network Metrics: Eigenvalue Centrality

Eigenvalue centrality is a measure of network centrality, keeping in consideration the importance of node connectivity and looks at global connectivity within network communities and is a better representative of spatial connectivity. There is evidence to show that Eigenvalue centrality works better than other measures such as indegree and closeness centrality (Ruhnau 2000; Bonacich 2007). Our network is further constrained spatially, and hence, connectivity of nodes are spatially dependent. For our centrality measures, the centrality is proportional to the sum of centralities of vertices which are connected. In our case λ being the largest eigenvalue of A (where A is the adjacency matrix) and n is the number of vertices:

$$Ax = \lambda x, \lambda x_i = \sum_{j=1}^{n} a_{ij} x_j, i = 1, \ldots \ldots . n$$

Once there Eigenvector Centralities (EVC) have been calculated we multiple EVC with the Combined entropy metric (CEM) to gauge the spatial distribution, connectivity, as well as heterogeneity, using both Shannon’s entropy and Analytic Hierarchical Process. This yields the spatially adjusted vulnerability index.

$$\boldsymbol{Adjusted\ Vulnerabiliy\ Index} = \sum_{i}^{n} \boldsymbol{CEM} * \boldsymbol{Eigen\ Value\ Centrality}\ (\boldsymbol{Layer})$$

4.3 Results

We examine combined spatial vulnerability to flooding by using multi-layer network analysis. We look at the clustering of vulnerability scores, the density of housing in planned and unplanned settlements, changes in urbanization and its consequences for impervious surfaces, and how vulnerability maps onto historically flood-prone areas. This approach allows us to identify how social, biophysical, and infrastructural factors function in combination to generate higher or lower vulnerability scores. While vulnerability is strongly influenced by infrastructure, urban expansion and socioeconomic conditions create emergent vulnerability conditions. Our study shows mutually that both infrastructure based biophysical vulnerability and socio-economic vulnerability largely influence the overall vulnerability measurement. Unplanned settlements seem to be growing at rates eight times greater than in planned areas, even with poor urban infrastructure. The increase in impermeable areas in planned settlements and increase in sediment flow to channels in unplanned settlements create a positive feedback loop which increases overall flow while subsequently reducing channel capacity affecting overall flooding. While each census sector experiences their measure of vulnerability and unique combination of variables that cause said vulnerability, vulnerability seems to be clustered in spatial units larger than the census sectors themselves. Such spatial effects such as the value of the same variables in neighboring census sectors is measured using spatial autocorrelation measures. Over 51% of census sectors have high or very high vulnerability, 26% of census sectors have medium vulnerability and 23% of the sectors have low vulnerability.

4.3.1 Distribution of LISA Autocorrelation of Vulnerability

We find that more than 50% of census sectors are positively clustered with either high or low vulnerability scores. Our methodology allowed this spatial clustering to be considered in the calculation AVI. Two-hundred and forty-six (246) census sectors are categorized as High-

High (HH) vulnerability class, encompassing a population of 283206 or 21.17% in 2010; 415 census sectors are categorized in Low-Low (LL) vulnerability classes, encompassing a population of 405836 or 30.34 % in 2010. The Low-High (LH) and High-Low (HL) classes make up 25 and 17 census sectors, respectively, with negative autocorrelation, while the remaining the census sectors (562) do not have any significant spatial autocorrelation. Within the LISA classes, the highest vulnerability value was 0.95, and the lowest was at 0.05, with a mean distribution of 0.39. Of the 679 total census sectors that are unplanned settlements, 186 of them, or 27%, can also be classified as an HH class. By contrast, only 112 census sectors that are unplanned settlements lie within the LL class or 16%. Thus, positively autocorrelated vulnerability index values constitute 43% of all census sectors within the areas with unplanned settlements.

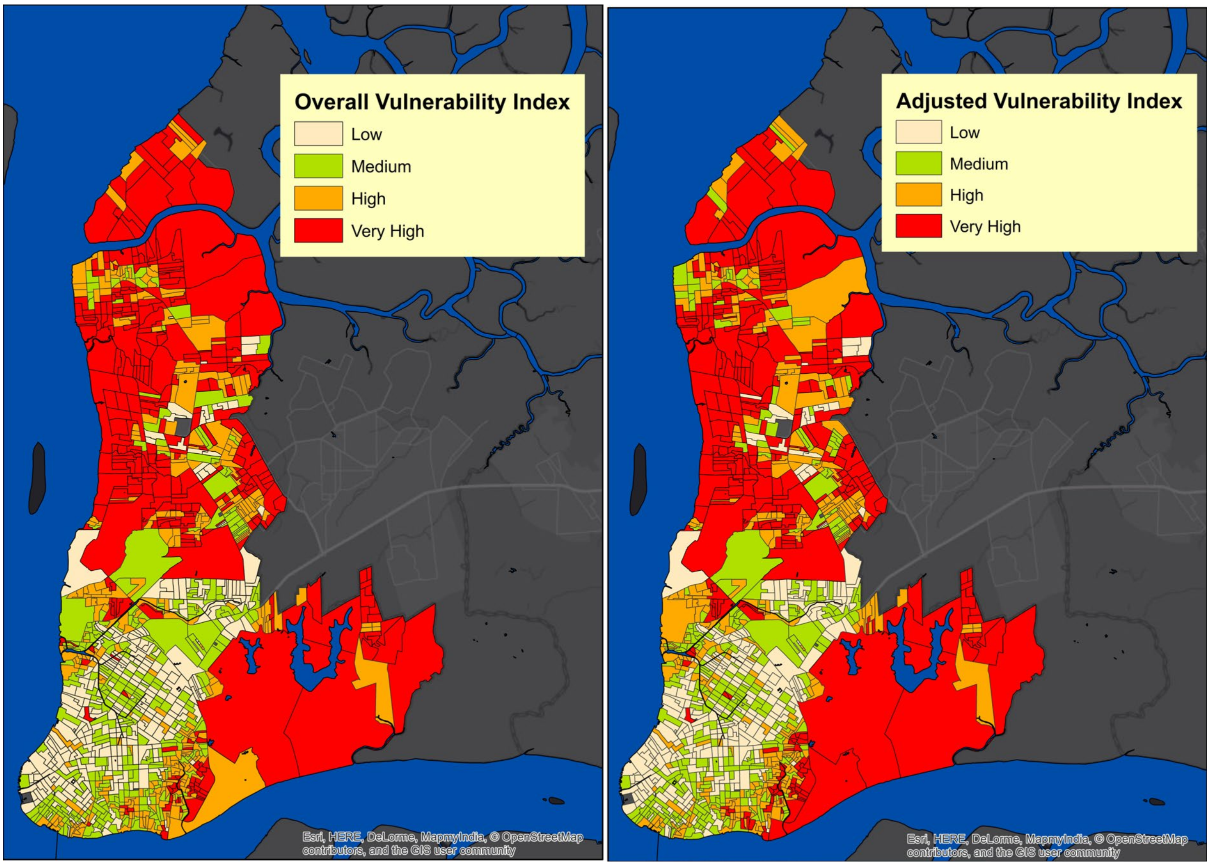

Figure 4.6: Left: Modified from Mansur et al 2018 and Right: Adjusted Vulnerability Index

While there are modest changes in terms of area covered under high and very high vulnerability, the Adjusted Vulnerability Index proposed in this paper reduces the overall percentage of population under very high risk (Figure 4.6, Figure 4.7, Table 4.4).

Table 4.4: Overall vulnerability index and the adjusted vulnerability index. The adjusted vulnerability index has nearly equally proportional vulnerability across gradients of vulnerability. This is indicative of the model, taking into account network relationships and spatial clustering effects to adjust for overall vulnerability.

Mansur et al 2016	Population	% Population	AVI	Population	% Population
Very High	507106	38	Very High	364355	27
High	327596	24	High	342383	25
Medium	306736	23	Medium	334484	25
Low	206969	15	Low	307185	23

By analyzing spatial clustering and network based relationships in the current paper, the authors hope to explore community model of inherent resilience in groups. The top 25% of the most vulnerable census sectors have a vulnerability index value of 0.48 or higher and the top 10% of the most vulnerable census sectors have a vulnerability index value of 0.60 or higher. For the census sectors that are unplanned settlements, 263 are over the 75th percentile of which 100 of them are over the 90th percentile at value 0.6 and higher. For planned census sectors, only 77 of them are over the 75th percentile of which only 30 are over the 90th percentile for the AVI.

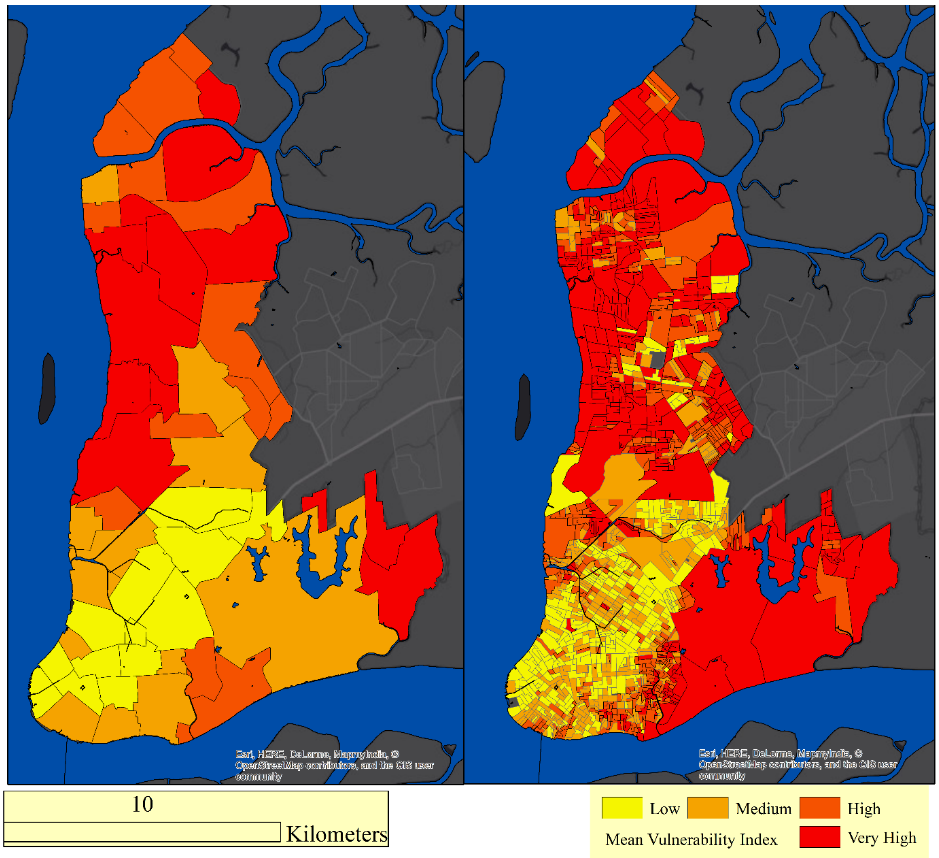

Figure 4.7: Left: Adjusted Vulnerability Index (AVI) across bairros (neighborhoods) and Right: AVI across census sectors

4.3.2 Land Use and Land Cover (Decadal Change)

Land cover considered as urban. i.e., densely populated and with a high proportion of impervious surfaces, has been increasing overall in this area with a net increase from 101 km^2 to 116 km^2 from 1990 to 2018. For the census sectors in unplanned settlements, the increase was from 43 km^2 to about 53 km^2 (23.31%), and from 58 km^2 to 63 km^2 (9.27%) for the remaining census sectors. The most vulnerable census sectors (top 25%) have the rate of urban land cover increase at 27.51%; this overlaps closely to the 23.31% rate experienced in unplanned settlements. This unplanned infrastructure growth is thereby closely tied to overall vulnerability to flooding. While the Landsat classification supported the analysis of overall urban expansion (Figure 4.8), we used high-resolution land cover classification for the subset of census sectors categorized as unplanned settlements (581 out of 679) to examine the built area over time, which changed from 14.79 km^2 in 2011, 15.51 km^2 in 2013 and 15.54 km^2 in 2015.

Within the census sectors characterized as unplanned settlements, the number of rooftops has a range of about a single rooftop intersecting with a census sector and a high of about 500 houses per sector, and within the rest of the city, the range is between a single rooftop to about 658 rooftops. In terms of rooftops per square kilometer the range lies between 3 to 13,000 rooftops/km^2 for unplanned settlements with a mean rooftop density of 4,164 rooftops/km^2. A density of 13,000 roof tops/km^2 represents a specific census sector (geocode 150140255000015), which has over 266 houses in an area of 0.019 km^2. For the rest of the city census sectors that are not part of unplanned settlements have a housing density, ranging from 3 to 6,768 rooftops/km^2 with a mean density of about 2,670 rooftops/km^2.

The number of housing units in an urban sector incorporates not only horizontal built growth but also vertical growth. Therefore, we obtained the number of housing units per census sector from the 2010 census to get total household units per square kilometer. For the census sectors in unplanned settlements, housing units ranged from 57 to 45,372 housing units/km^2, with a mean of about 5,314 housing units/km^2. The highest total number of housing units was 218 housing units in 0.004 km^2. For census sectors that do not lie in within unplanned settlements, the highest housing unit density is 33,344 housing units per km^2 and the lowest at about 1 housing unit per km^2. The mean value is at 4,175 housing units/km^2.

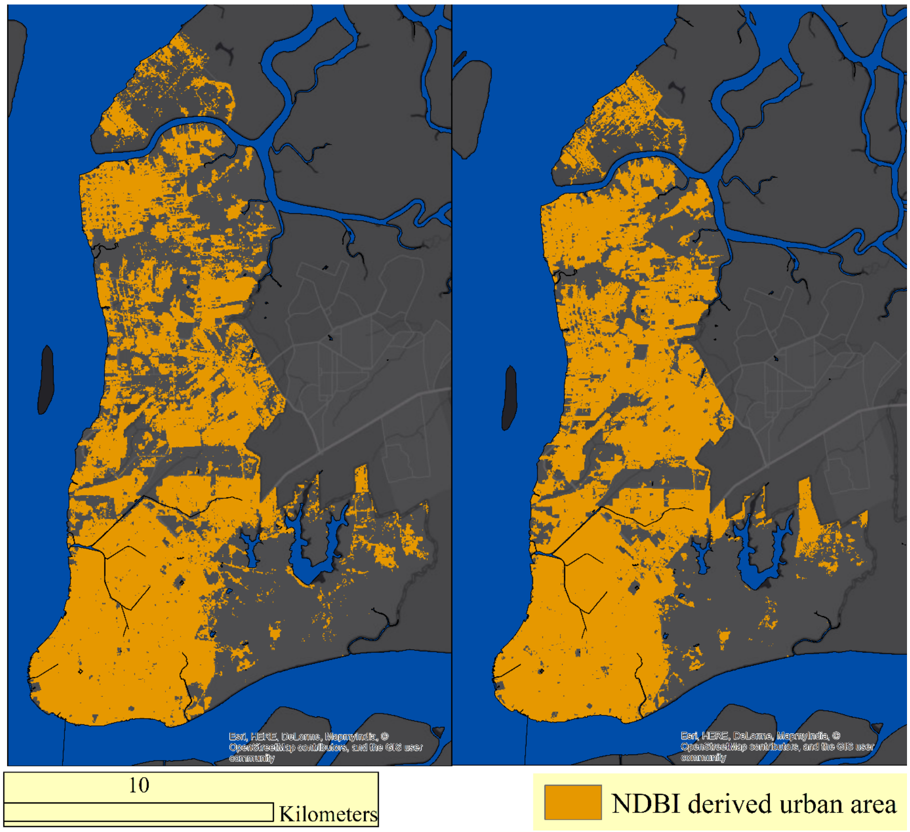

Figure 4.8: NDBI and OTSU method derived urban extent Left: from 1990-1995 composite and Right: 2015-2018 composite

Increasing urbanization and count of building footprint indicates an increase in the overall impermeability which further leading to increase in overland flow and associated flooding. The impermeability layer was used to assess that out of a total of 174 census sectors out of the 1265 total sectors in our AOI (i.e., 14%) have at least one or more permeable areas within them. Of these permeable sectors, 79 lie in unplanned settlements, while the remaining 95 lie outside subnormal areas. The remaining census sectors in our AOI, 1091 (86%) are impermeable.

4.3.3 Elevation and historic inundation

From the contour derived elevation data (Digital Elevation Model), mean elevation was calculated for each census sector. Of the 679 sectors that are defined as SN, the range in elevation is 3-19m, with an average of 8m. The highest overall mean elevation in a single sector was 20m, while for the lowest areas the average per-sector elevation was 3m. Of the

156 census sectors that can be defined as low lying elevation (i.e., elevation less than 4m), 139 of them lie within unplanned settlements.

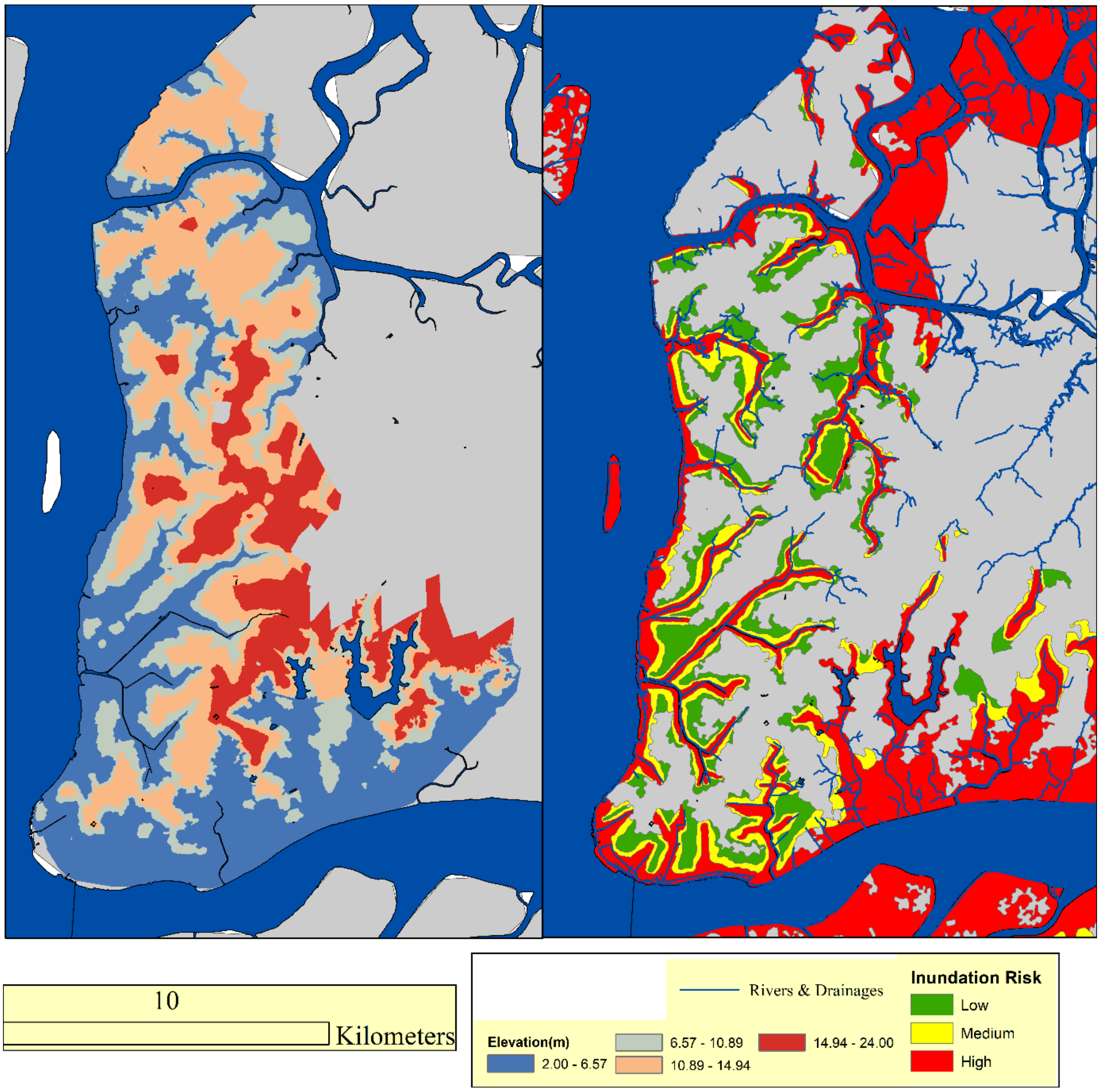

Figure 4.9: Left contour survey derived digital elevation model and Right: historic flood inundation risk along with rivers, channels, and drainages. (Source: CONSAMPA)

We find that 75% of historically flooded areas are census sectors have higher physical risks but lower social risks. Only 25% of historical flooding has occurred in unplanned settlements (Figure 4.9). This is consistent with our finding that overall vulnerability assessments point to other areas where the census sector may experience heightened risks due to higher social risks, without necessarily having similarly high physical risks. Based on the inundation risk map (Figure 4.9), we find that inundation risk perfectly overlays with the contour derived DEM that we created earlier and depict areas near lower elevation where flood water may try to exit out via the channels or accumulate as a result of the natural topography.

These inundated areas, despite being served by failing macro and micro drainage channels, are susceptible to flooding by two methods i) the water from tidal and backflow into the channels makes the channels behave as flood banks and the areas they are serving are the ones that are highest at risk. ii) the combination of topography, total urban area coverage, living density, and impermeable area that increases the overall flow of water in the surface, causing flooding again.

4.4 Discussion

Our findings point to several important challenges and insights for reducing vulnerability in Belem and other increasingly populated deltaic urban areas. First, our spatial analysis of planned and unplanned settlements reveals that socioeconomic factors shape residents' susceptibility to hazards more substantially than biophysical exposure. Second, while it is unsurprising that housing density is greater in unplanned settlements, we show that it is eight times greater than in planned areas. Unplanned settlements having mutually reinforcing drivers of high vulnerability, where limited financial options for dwelling construction facilitate more stress on existing flood control with an area of already constrained economic resources. Third, we show that vulnerability itself is clustered representing spatial dependence and interactions amongst census sectors and bairros. Spatial clustering of vulnerability points towards underlying interactions and areas of the cities facing similar distribution and contribution to variables that constitute the overall vulnerability.

Our spatial analysis demonstrates the impact of urban infrastructure on people's vulnerability. While we would anticipate that clustering of HH and LL vulnerability would be strongly correlated with elevation and proximity to water, by incorporating a wider range of spatially explicit social and biophysical variables, we show that increasing urbanization (and the impervious surface is directly connected to increasing high-frequency and high-volume flooding. Increasing urbanization over the last couple of decades drastically increased the amount of impermeable area (Ponte and Brandao; Gilbert 1998; Perz 2000; Lima 2001). Most of the macro and micro drainage projects were designed to align with the local topography. However, the canals that were built were not always lined with concrete. Instead, unlined stream banks erode and add more sediments into the channel, which reduces channel capacity. These increased in the urban built environment and urban density means that there is a larger number of housing units living in the same vulnerable area and as a result, though urban footprint for certain buildings has remained the same, vertical growth in building height has allowed even more people to be effected by the spatial vulnerability.

Our cluster analysis revealed that unplanned settlements are located together and act as pockets of high socioeconomic susceptibility to floods. Also, we found that areas with low vulnerability to flooding also appeared clustered. Both dynamics indicate that socioeconomic susceptibility can be the primary driver of vulnerability to flooding, even with low or high values of biophysical exposure. While a mean vulnerability index for all census sectors in bairros allowed for determining the spread of vulnerability in its constituent census sectors it also allowed for comparison across neighborhoods. The vulnerability itself is tied to and is most influenced by infrastructure-based indicator variables while the study also shows that income is nearly equally important, these were based on the spatial adjustment and acted as adjustment weights to calculated AVI.

Finally, our study provides several methodological contributions to the literature. We introduced several long-term datasets that were derived from both sensor-based datasets such as tidal, land use and land cover, precipitation along with field survey which gave us a gradient of channels allowing us to build upon our understanding of vulnerability and overlay it with other proxies that act as flood indicators. Additional data were also collected from multiple agencies such as CONSANPA, CODEM, IBGE, and COHAB. These indicators included ground derived contour points and lines which were utilized to create a high-resolution look at the urban topography. We posit that the city's channelization through past drainage projects counterproductively increased flooding into the city rather than providing drainage during heavy rainfall events. This effect of channelization with open surface channels have been discussed in earlier works in similar setups (Tucci 2002; Fewtrell et al. 2008; Peixoto et al. 2009).

While some census sectors will benefit from topography gradients and urban infrastructure including auxiliary channels to help ease transient flooding, most census sectors are likely to face increased flood frequency and volume for large unplanned settlements. Unplanned and unstructured settlements with limited economic means give rise to more temporary growth in the urban area. Since the flood control channels in these areas are not paved and neither the roadways means they are prone towards more sediment flow to accumulate from these areas into the channels. This further leads to narrowing of channels as has been reported by field interviews conducted by the authors.

Vulnerability, as established throughout the paper, is a complex amalgamation of multiple factors that creates risk, which then translates to vulnerability. Vulnerability though felt at the level of the individual is also spatially linked process not just spatially but also owing to social dynamic and community resilience that might exist in groups of people living in such areas. The vulnerability model proposed in this paper establishes a robust method to gauge parametric vulnerability across space and takes into account spatial relationships that are often not found in aspatial models. The model can be used across time, and new parameters can be added, and the model will adjust to additional layers in the multilayer based vulnerability index. Across census sectors, proxy datasets such as building density, climatic variability and inundation maps of the region point to proxy indicators that could enrich such models and expand our understanding of how the models themselves should evolve.

4.5 Conclusion

Our paper provides a novel methodology and creates an adjusted vulnerability index, which combines spatial configuration and reassesses indicator variables that determine the overall vulnerability that Belem faces to urban flooding. Spatial dispersion and connectivity allow us to explore relationships between factors affecting vulnerability as well as the collective spatial vulnerability that might exist in neighborhoods and unplanned settlements or subnormal agglomerations as they are called and classified by the government. The study further includes proxies that serve as vulnerability indicators and allow us to understand how growth in population combines with urban infrastructure in a positive feedback loop. The core methodology of this paper serves as a contribution to understanding spatial and social interactions at a macroscopic scale within neighborhoods or bairros as well over the larger city. In the future studies, we hope to include additional datasets, including risk area determination based on the Brazilian Institute of Geography and Statistics (IBGE's) recent classification of risk and risk areas. The authors hope to utilize the 2020 census data for a temporal study of the same region to assess the temporal performance of these models. The 2020 census will also allow for longitudinal comparison of key changes in infrastructure and indicator values to the method we developed designed to handle both spatial as well as temporal relationships.

Density of population and the experience of these people living across the canal is captured in the narrative of the field interviews across people living in areas where canals have helped reduce flooding and in few where they have been linked to increased frequency of flood, One cannot help but notice how the canals often functionally overlay the same boundaries as that which separates the unplanned settlements from the planned ones. Apart from standard models on flood vulnerability and social vulnerability models such as Flood Risk Index (Kiem et al. 2003; Hirabayashi et al. 2013), Social Vulnerability Index (Cutter et al. 2003; Bjarnadottir et al. 2011) and Socio-Economic Vulnerability Index (McLaughlin et al. 2002; Brouwer et al. 2007, p.), models of vulnerability will benefit from accounting for spatial effects. The issue of richer and more real-time data on flood events and the extent and scale of flooding would be extremely valuable to improve such models, along with estimates of carrying capacity of existing infrastructure. With changing climate extreme events in large portions of the world are only supposed to intensify, we are no longer living in an area where proximity to river channels could be used for simple flood plain modeling, we must change our definitions of flood plains keeping in consideration anthropogenic changes and channel infrastructures. Such models evolve and can serve as important indicators of coevolving systems where social and spatial changes influence each other, and it allows us to study the city as a living organism in interaction with its overall population.

References

Adger WN, Kelly PM (2012) Social vulnerability and resilience. In: Living with Environmental Change. Routledge, pp 41–56

Adger WN, Kelly PM (1999) Social vulnerability to climate change and the architecture of entitlements. Mitigation and adaptation strategies for global change 4:253–266

Anselin L (1995) Local indicators of spatial association—LISA. Geographical analysis 27:93–115

Balica SF, Douben N, Wright NG (2009) Flood vulnerability indices at varying spatial scales. Water science and technology 60:2571

Balica SF, Wright NG, van der Meulen F (2012) A flood vulnerability index for coastal cities and its use in assessing climate change impacts. Natural hazards 64:73–105

Barnett J (2003) Security and climate change. Global environmental change 13:7–17

Barnett J, Adger WN (2007) Climate change, human security and violent conflict. Political geography 26:639–655

Bhatta B, Saraswati S, Bandyopadhyay D (2010) Urban sprawl measurement from remote sensing data. Applied geography 30:731–740

Bjarnadottir S, Li Y, Stewart MG (2011) Social vulnerability index for coastal communities at risk to hurricane hazard and a changing climate. Natural Hazards 59:1055–1075

Bonacich P (2007) Some unique properties of eigenvector centrality. Social networks 29:555–564

Brondizio ES, Vogt ND, Mansur AV, et al (2016) A conceptual framework for analyzing deltas as coupled social–ecological systems: an example from the Amazon River Delta. Sustainability Science 11:591–609

Brooks N (2003) Vulnerability, risk and adaptation: A conceptual framework. Tyndall Centre for Climate Change Research Working Paper 38:1–16

Brouwer R, Akter S, Brander L, Haque E (2007) Socioeconomic vulnerability and adaptation to environmental risk: a case study of climate change and flooding in Bangladesh. Risk analysis 27:313–326

Burton I (1997) Vulnerability and adaptive response in the context of climate and climate change. Climatic Change 36:185–196

Cardona OD (2011) Disaster risk and vulnerability: Concepts and measurement of human and environmental insecurity. In: Coping with Global Environmental Change, Disasters and Security. Springer, pp 107–121

Cardona OD (2013) The need for rethinking the concepts of vulnerability and risk from a holistic perspective: a necessary review and criticism for effective risk management. In: Mapping vulnerability. Routledge, pp 56–70

Cheng T, Haworth J, Wang J (2012) Spatio-temporal autocorrelation of road network data. Journal of Geographical Systems 14:389–413

Cliff AD, Ord K (1970) Spatial autocorrelation: a review of existing and new measures with applications. Economic Geography 46:269–292

Costa SM, Brondízio ES (2011) Cities along the floodplain of the Brazilian Amazon: characteristics and trends. In: The Amazon Várzea. Springer, pp 83–97

Cutter SL (1996) Vulnerability to environmental hazards. Progress in human geography 20:529–539

Cutter SL, Boruff BJ, Shirley WL (2003) Social vulnerability to environmental hazards. Social science quarterly 84:242–261

Dias CS, Dias SIS (2007) Belém do Pará: história, urbanismo e identidade. Planejamento Urbano e Regional: ensaios acadêmicos do CAUFAG Cascavel: Smolarek Arquitetura dos Santos FAA, da Rocha EJP (2014) Alagamento e inundação em áreas urbanas. Estudo de caso: cidade de Belém. Revista GeoAmazônia 2:33–55

Fewtrell TJ, Bates PD, Horritt M, Hunter NM (2008) Evaluating the effect of scale in flood inundation modelling in urban environments. Hydrological Processes: An International Journal 22:5107–5118

Filizola N, Latrubesse EM, Fraizy P, et al (2014) Was the 2009 flood the most hazardous or the largest ever recorded in the Amazon? Geomorphology 215:99–105

Flater D (1998) XTide Manual: Harmonic tide clock and tide predictor. EUA Google Scholar

Flater D (1996) A brief introduction to XTide. Linux Journal 1996:6

Fluet-Chouinard E, Lehner B, Rebelo L-M, et al (2015) Development of a global inundation map at high spatial resolution from topographic downscaling of coarse-scale remote sensing data. Remote Sensing of Environment 158:348–361

Fotheringham AS (2009) "The problem of spatial autocorrelation" and local spatial statistics. Geographical analysis 41:398–403

Fotheringham AS, Charlton ME, Brunsdon C (1998) Geographically weighted regression: a natural evolution of the expansion method for spatial data analysis. Environment and planning A 30:1905–1927

Funk C, Peterson P, Landsfeld M, et al (2015) The climate hazards infrared precipitation with stations—a new environmental record for monitoring extremes. Scientific data 2:150066

Gao B-C (1996) NDWI—A normalized difference water index for remote sensing of vegetation liquid water from space. Remote sensing of environment 58:257–266

Gilbert A (1998) Rainforest Cities: Urbanization, Development, and Globalization of the Brazilian Amazon. JSTOR

Gorelick N, Hancher M, Dixon M, et al (2017) Google Earth Engine: Planetary-scale geospatial analysis for everyone. Remote Sensing of Environment 202:18–27

Guedes G, Costa S, Brondizio E (2009) Revisiting the hierarchy of urban areas in the Brazilian Amazon: a multilevel approach. Population and environment 30:159–192

Hill MO (1973) Diversity and evenness: a unifying notation and its consequences. Ecology 54:427–432

Hirabayashi Y, Mahendran R, Koirala S, et al (2013) Global flood risk under climate change. Nature Climate Change 3:816

Hurst SA (2008) Vulnerability in research and health care; describing the elephant in the room? Bioethics 22:191–202

Katsanos D, Retalis A, Michaelides S (2016) Validation of a high-resolution precipitation database (CHIRPS) over Cyprus for a 30-year period. Atmospheric Research 169:459–464

Kelly PM, Adger WN (2000) Theory and practice in assessing vulnerability to climate change andFacilitating adaptation. Climatic change 47:325–352

Keshava N (2003) A survey of spectral unmixing algorithms. Lincoln laboratory journal 14:55–78

Keshava N, Mustard JF (2002) Spectral unmixing. IEEE signal processing magazine 19:44–57

Kiem AS, Franks SW, Kuczera G (2003) Multi-decadal variability of flood risk. Geophysical Research Letters 30:

Krstanovic PF, Singh VP (1992a) Evaluation of rainfall networks using entropy: I. Theoretical development. Water Resources Management 6:279–293

Krstanovic PF, Singh VP (1992b) Evaluation of rainfall networks using entropy: II. Application. Water Resources Management 6:295–314

Lima JJ (2001) Socio-spatial segregation and urban form: Belem at the end of the 1990s. Geoforum 32:493–507

Lin J (1991) Divergence measures based on the Shannon entropy. IEEE Transactions on Information theory 37:145–151

López-Carr D, Pricope NG, Aukema JE, et al (2014) A spatial analysis of population dynamics and climate change in Africa: potential vulnerability hot spots emerge where precipitation declines and demographic pressures coincide. Population and Environment 35:323–339

Mansur AV, Brondízio ES, Roy S, et al (2016) An assessment of urban vulnerability in the Amazon Delta and Estuary: a multi-criterion index of flood exposure, socio-economic conditions and infrastructure. Sustainability Science 11:625–643

Mansur AV, Brondizio ES, Roy S, et al (2018) Adapting to urban challenges in the Amazon: flood risk and infrastructure deficiencies in Belém, Brazil. Regional Environmental Change 18:1411–1426

Mansur AV, Brondizio ES, Roy S, et al (2017) Adapting to urban challenges in the Amazon: flood risk and infrastructure deficiencies in Belém, Brazil. Regional Environmental Change 1–16

Martín MA, Rey J-M (2000) On the role of Shannon's entropy as a measure of heterogeneity. Geoderma 98:1–3

McLaughlin S, McKenna J, Cooper JAG (2002) Socio-economic data in coastal vulnerability indices: constraints and opportunities. Journal of Coastal Research 36:487–497

Mitchell J (1999) Crucibles of hazard: mega-cities and disasters in transition. United Nations University Press

Mitchell JK, Mitchell JK (1996) The long road to recovery: Community responses to industrial disaster. United Nations University Press Tokyo

Nagendra H, Bai X, Brondizio ES, Lwasa S (2018) The urban south and the predicament of global sustainability. Nature Sustainability 1:341

Newton A, Carruthers TJ, Icely J (2012) The coastal syndromes and hotspots on the coast. Estuarine, Coastal and Shelf Science 96:39–47

Nishat A, Mukherjee N (2013) Climate change impacts, scenario and vulnerability of Bangladesh. In: Climate Change Adaptation Actions in Bangladesh. Springer, pp 15–41

O'Brien KL, Wolf J (2010) A values-based approach to vulnerability and adaptation to climate change. Wiley Interdisciplinary Reviews: Climate Change 1:232–242

Ord JK, Getis A (1995) Local spatial autocorrelation statistics: distributional issues and an application. Geographical analysis 27:286–306

Ord JK, Getis A (2001) Testing for local spatial autocorrelation in the presence of global autocorrelation. Journal of Regional Science 41:411–432

Otsu N (1979) A threshold selection method from gray-level histograms. IEEE transactions on systems, man, and cybernetics 9:62–66

Overeem I, Brakenridge RG (2009) Dynamics and vulnerability of delta systems. GKSS Research Centre, LOICZ Internat. Project Office, Inst. for Coastal Research

Padoch C, Brondizio E, Costa S, et al (2008) Urban forest and rural cities: multi-sited households, consumption patterns, and forest resources in Amazonia. Ecology and Society 13:

Padoch C, Stewart A, Pinedo-Vasquez M, et al (2014) Urban residence, rural employment, and the future of Amazonian forests. In: The social lives of forests: Past, present, and future of woodland resurgence. Chicago University Press, Pegado RS, Blanco CJC, Roehrig J, et al (2012a) The importance of physical indicators in areas of urban flood: the case of the metropolitan region of Belém. International Journal of Civil and Environmental Engineering 12:42–48

Pegado RS, Calvacante CJB, Roehrig J, et al (2012b) Flooding in the city of Belém-PA, Brazil: causes and mitigation measures. In: Integrated Water Resources Management, IWRM Congress 2012. Fraunhofer Verlag Stuttgart, pp 1–7

Peixoto JMA, Nelson BW, Wittmann F (2009) Spatial and temporal dynamics of river channel migration and vegetation in central Amazonian white-water floodplains by remote-sensing techniques. Remote Sensing of Environment 113:2258–2266

Perz SG (2000) The quality of urban environments in the Brazilian Amazon. Social Indicators Research 49:181–212

Pinedo-Vasquez M, Padoch C (2009) Urban and rural and in-between: Multi-sited households, mobility and resource management in the Amazon floodplain. Mobility and migration in indigenous Amazonia: Contemporary ethnoecological perspectives 11:86–96

Ponte J, Brandao AJD das N Urban drainage in the Metropolitan Region of Belém, Brazil: an urbanistic study. SIO-LONG, Ao; ALAN HOI-SHOU, Chan; HIDEKI, Katagiri 358–371

Ponte JPX (2015) Belém do Pará: cidade e água. Cadernos Metrópole 17:41–60

Rashed T, Weeks J, Couclelis H, Herold M (2007) An integrative GIS and remote sensing model for place-based urban vulnerability analysis. Integration of GIS and remote sensing Wiley, Chichester 199–224

Renaud FG, Kuenzer C (2012) The Mekong Delta system: Interdisciplinary analyses of a river delta. Springer Science & Business Media

Roberts D, Mueller N, Mcintyre A (2017) High-dimensional pixel composites from earth observation time series. IEEE Transactions on Geoscience and Remote Sensing 55:6254–6264

Ruhnau B (2000) Eigenvector-centrality—a node-centrality? Social networks 22:357–365

Saaty RW (1987) The analytic hierarchy process—what it is and how it is used. Mathematical modelling 9:161–176

Saaty TL (2008) Decision making with the analytic hierarchy process. International journal of services sciences 1:83–98

Saaty TL (2013) Analytic hierarchy process. In: Encyclopedia of operations research and management science. Springer, pp 52–64

Sebesvari Z, Renaud FG, Haas S, et al (2016) A review of vulnerability indicators for deltaic social–ecological systems. Sustainability Science 11:575–590

Shannon CE (1948) A mathematical theory of communication. Bell system technical journal 27:379–423

Shelestov A, Lavreniuk M, Kussul N, et al (2017) Exploring Google Earth Engine platform for big data processing: classification of multi-temporal satellite imagery for crop mapping. Frontiers in Earth Science 5:17

Soares AAS, Carvalho AC, Soares DAS, Bastos RZ (2018) Fundamentos para a gestão das inundações periódicas nas planícies de Belém (Pará-Brasil) com vistas ao seu desenvolvimento local. Contribuciones a las ciencias sociales, Málaga 39:37–56

Swift J (1989) Why are rural people vulnerable to famine? IDS bulletin 20:8–15

Syvitski JP, Kettner AJ, Overeem I, et al (2009) Sinking deltas due to human activities. Nature Geoscience 2:681–686

Tessler ZD, Vörösmarty CJ, Grossberg M, et al (2015) Profiling risk and sustainability in coastal deltas of the world. Science 349:638–643

Tucci C (2002) Flood control and urban drainage management in Brazil. waterlines 20:6–8

Turner BL, Kasperson RE, Matson PA, et al (2003) A framework for vulnerability analysis in sustainability science. Proceedings of the national academy of sciences 100:8074–8079

Vargas LG (1990) An overview of the analytic hierarchy process and its applications. European journal of operational research 48:2–8

Vogt N, Pinedo-Vasquez M, Brondízio ES, et al (2016) Local ecological knowledge and incremental adaptation to changing flood patterns in the Amazon delta. Sustainability Science 11:611–623

White GF, Kates RW, Burton I (2001) Knowing better and losing even more: the use of knowledge in hazards management. Global Environmental Change Part B: Environmental Hazards 3:81–92

Wulder M, Boots B (1998) Local spatial autocorrelation characteristics of remotely sensed imagery assessed with the Getis statistic. International Journal of Remote Sensing 19:2223–2231

Zahedi F (1986) The analytic hierarchy process—a survey of the method and its applications. interfaces 16:96–108

Zha Y, Gao J, Ni S (2003) Use of normalized difference built-up index in automatically mapping urban areas from TM imagery. International Journal of Remote Sensing 24:583–594

Chapter 5: Conclusion and Summary

The main focus of my dissertation has been twofold: i) to analyze the spatial and temporal patterns of land loss across the Lower Mississipi River Delta (LMRD) in Louisiana and ii) to study the impact of urbanization and anthropogenic feedbacks on urban flood vulnerability in Belem, Brazil.

A fundamental goal of landscape science is to connect landscape patterns to their underlying processes across different spatial and temporal scales (Liding et al., 2008; Turner, 1989; Turner et al., 2001). The driving processes of landscape patterns can be either anthropogenic, environmental, or some combination of the two. For example, in urban landscapes, anthropogenic activities such as urbanization, and consequent building of flood control infrastructure have altered the underlying hydrology leading to an increased tendency for flood events. On the other hand, the environmental processes of sediment flow, deforestation, channelization, and subsidence, which in and of themselves are indirectly attributed to human activities, can increase landscape fragmentation and overall land loss.

My dissertation assesses land loss as a measure of spatial and temporal stability of land pixels and evaluates the morphology of land loss. Anthropogenic activities often modify deltaic systems, and these modifications coupled with changing climate across urban deltas can increase flood vulnerability. To evaluate the impact of understanding land loss and flood vulnerability we investigated three different topics; i) Land loss and fragmentation in the Mississippi river basin ii) Comparison of landscape fragmentation using multiple sensors within the Mississippi river basin and iii) Flood vulnerability assessment using network analysis within Belem, Brazil. The overall dissertation juxtaposes two spatially-variant landscapes that have both been extensively modified by human influences. The key points and takeaways are summarized in the following paragraphs.

Chapter 2:

The use of temporal metrics land loss to describe landscape fragmentation in deltaic systems is still rare (Britsch and Dunbar, 1993, 1993; Couvillion et al., 2011; Penland et al., 2000). Thus, most previous analyses have focused only on permanent land loss and not considered loss events that first oscillate between land and water (Britsch and Dunbar, 1993, 1993; Couvillion et al., 2011; Penland et al., 2000). In recent years, the analytical methods used to detect and decipher the spatial patterns of land loss have evolved significantly, with significant improvements in cloud computing as well as the ability to analyze deep time stacks of imagery (Donchyts et al., 2016a, 2016b; Gorelick et al., 2017). In my work, a novel stability index approach was developed to understand the temporal probability of each land pixel to convert to water and become lost permanently. The main contribution of this paper is to question the long-held assumption in land loss models that all loss is permanent and to incorporate our stability index (SI) to understand the dynamic nature of land-to-water transitions over time. This paper further examines if these losses are clustered in space and time by using Local Indicator of Spatial Autocorrelation (LISA) (Anselin, 1995; Fotheringham, 2009). Using these LISA classes, I then analyzed the positively-autocorrelated clusters (i.e., low-low autocorrelation and high-high autocorrelation) for landscape morphology using metrics such as patch density and shape (Cushman et al., 2008; Lang et al., 2008), demonstrating that both positively autocorrelated LISA clusters are directly correlated to patch density and shape.

- We showed that land loss is a mix of single and multiple transitions between land and water classification and point to multiple process regimes that act on land surfaces.

- We showed that while a spatial analysis is relevant to create an overall trajectory, the Stability index that we created provides a temporal provenance of loss over time.
- We further demonstrated that there is a relationship between land loss and the landscape metrics of overall fragmentation and shape of land loss. These relationships created by the spatial autocorrelations are indicative of process regimes acting on different parts of the landscape.

Chapter 3:

My second paper (Chapter-3) revisits the LMRD and highlights the use of different remote sensing platforms and earth observation datasets to estimate delta land loss (Bernier et al., 2006; Britsch and Dunbar, 1993; Edmonds et al., 2017; Overeem and Brakenridge, 2009; Syvitski et al., 2009). In this chapter, I performed a comparative analysis of multiple sensors that vary in their spatial, temporal and spectral resolution. We examined the improvement of finer spatial and temporal resolution Earth Observation Systems (EOS) by comparing data from legacy Landsat series imagery, along with Sentinel-2 and the PlanetScope CubeSat constellation imagery (Gašparović et al., 2018; Li and Roy, 2017; Reiche et al., 2018). I also created an automated, stratified-sampling approach (Imbens and Lancaster, 1996; Nassiuma, 2000; Neyman, 1934; Trost, 1986) for sampling end-member signatures. I applied this method to two different land loss estimation metrics, including spectral unmixing (Heylen and Scheunders, 2011; Keshava, 2003; Keshava and Mustard, 2002) and the index-based approaches: Modified Normalized Difference Water Index and Normalized Difference Water Index (Donchyts et al., 2016b; Gao, 1996; Han-Qiu, 2005). To improve repeatability of such analyses for other researchers working in different systems, all analyses were performed on Google Earth Engine (GEE), Google's cloud computing system and the codes were published online for all users. Trend detection was further carried out using Mann-Kendall trend analysis (Abdi, 2007; Hamed, 2008; Neeti and Eastman, 2011) to assess overall loss and gain dynamics at a pixel level. Overall, this paper contributes to better identification of at-risk areas and populations and could be used to help protect vulnerable populations, providing indirect savings to local governments through improved mitigation strategies.

- Spatial and temporal windows of observations are variant across multiple sensors and the observed classification outcomes are sensitive to the spatial and spectral resolution of observations.
- We introduced a stratified sampling approach and combined it with Mann-Kendall statistics to analyze monotonicity over the temporal timeframe of the analyses.
- Spectral and spatial variability are key in identifying land-water boundaries effectively. While finer spatial resolution allows for better edge detection, spectral resolution improves end-member separation through the use of multiple bands.

Chapter 4:

In urban deltas with large human populations, flood vulnerability tends to increase over time. My third paper (Chapter-4) looks at Belem, Brazil, which is an urban area within the Amazon River Delta. This chapter harnesses both physical and socio-economic datasets to create a spatially distributed dataset. The main contribution of this paper is the creation of an adjusted vulnerability index that is derived from i) spatial dispersion measures founded in Shannon's entropy (Martín and Rey, 2000, 2000; Shannon, 1948) ii) a multilayer network analysis and iii) local indicators of spatial autocorrelation (LISA). This methodology allows us to look at spatial dispersion and aggregation of vulnerability indicator variables in determining the overall vulnerability in the region. My work analyzes vulnerability at varying spatial scales relevant to human interaction, with census sector being the finest spatial resolution. These spatial units are clustered in groups such as planned and unplanned settlements as categorized by the Brazilian Institute of Geography and Statistics (IBGE) and aggregated to bairros which are neighborhoods comprised of census sectors. Furthermore, I introduced a methodology that analyzes indicator variables along with proxy climate and infrastructure variables in diagnosing flood risks in the context of a city that has introduced channelization, but where failing infrastructure has exacerbated overall flood vulnerability.

- We created a novel spatially-adjusted vulnerability index to assess flood vulnerability in an urban delta using Physical and socioeconomic indicator variables, proxy climate and infrastructure variables and a multilayer network analysis model.
- We determined that vulnerability seemed to be clustered and there are observable differences in vulnerability between planned and unplanned settlements.
- We confirmed that physical indicators coupled with socio-economic indicators and proxy variables, such as building density and infrastructure metrics, serve as useful proxies of the overall variability in flooding vulnerability.

In this dissertation, I focused on landscape ecology pattern-process relationships. I further analyzed social relationships to spatial data and incorporated spatial network analysis in deltaic systems. My research contributes to several novel methodologies to the study of these vulnerable ecosystems, including the Stability Index and the Adjusted Vulnerability Index. The dissertation further focuses on the repeatability of analysis throughout all chapters. In summary, through my thesis I attempted to connect pixel-level analyses to underlying physical process and social relationships at the landscape scale.

Samapriya Roy
Department of Geography roysam@iu.edu
Bloomington, IN 47405

SPECIALIZATION & INTERESTS

Remote Sensing and GIS Applications. Urban systems analysis, patterns, and hydrology. Land Use and Land Cover Change Science.

EDUCATION

2019 **Doctor of Philosophy**
Indiana University at Bloomington (IUB)
Department of Geography – "*Delta Dynamics: Understanding Process, Pattern, and People Using Remote Sensing And Systems Analysis In Coastal Louisiana And Amazon River Delta*"
GPA – 3.6

2013 **Master of Science**
Indiana University-Purdue University at Indianapolis (IUPUI)
Department of Earth Sciences – "*Remote sensing & GIS applications for drainage detection and modeling in agricultural watersheds*"
GPA – 3.4

2011 **Bachelors of Technology**
Visvesvaraya National Institute of Technology, India (VNIT)
Department of Civil Engineering – "*Social network analysis for mapping segmented growth in urban cities in India*"
GPA – NA (*at this institution*)

EXPERIENCE

- **Customer and Researcher Engagement (December 2018-Present)**.Championing Planet's customer products and offerings in-person and via online assistance, by presenting at conferences, writing technical tutorials, and publishing articles and videos. Building tools, demos and sample applications, and continuously improving the applications that customers and developers experience using Planet's APIs and analytics endpoints. Identifying strategic partnership opportunities and growing Planet's customer base and research community across multiple scales, domain expertise and applications. Influencing the direction of Planet's developer products and offerings by gathering insights from customer engagement and the developer community. Interacting and engaging with users in Planet's Education and Research program to source novel customer applications and unique insights.
- **Senior Developer Advocate Intern, Planet Labs (May 2018- September 2018)**. Responsibilities include Growing and supporting Planet's technical user communities and developing new analytical tools and tutorials. Teaching workshops and delivering conference talks to technologists in academic communities and to developers in the geospatial and cloud industries. Collaborating on remote sensing science, including primary research on the evolution, geomorphology, and long-term welfare of the world's coastal ecosystems.

- **Developer Advocate Intern, Planet Labs (January 2018- May 2018).** Responsibilities include growing and supporting user communities for Planet's

Developer Center and the Education and Research Program. Developing new analytical tools, tutorials, and workshops for technical users of Planet data and tools.

- **Coastal SEES Collaborative Research: Changes in actual and perceived coastal flood risks due to river management strategies (NSF: 1426997)**. Partner-PI. National Science Foundation. Responsible for looking at land loss models and remote sensing application to coastal land loss. Includes model building and assessment along with hydrological model based vulnerability assessment of same area looking at landscape pattern and progress.

- **Catalyzing action towards sustainability of deltaic systems with an integrated modeling framework for risk assessment (DELTAS: 1342946)**. Partner-PI. National Science Foundation, Belmont Forum. Partner PI [International collaborative network of 24 institutions] (2015-2016) Responsible for looking at physical models of vulnerability and risk assessment in deltaic areas and among populated regions within Brazil. Includes model building and assessment along with hydrological model based vulnerability assessment of the same area.

- **National Aeronautics and Space Administration(NASA: NNX11AF50G)** (01/01/2013–12/31/2014) Carbon Dynamics, Land Cover Change, and Vulnerability of the World's Largest Coastal Mangrove Ecosystem to Climate Change, with Dr. Rinku Roy Chowdhury
Responsibilities included a review of existing datasets and literature. Evaluation of existing LULC classes using Landsat ETM+ and GeoEye classified raster datasets. Assessment of existing census and socio-ecological data.

- **National Science Foundation (NSF: 1065785)** (07/01/2013–06/30/2015). Collaborative Research: Ecological Homogenization of Urban America, with Dr. Rinku Roy Chowdhury Responsibilities, included analysis of land cover data at census block group and parcel levels using landscape metrics and analysis of land cover heterogeneity or homogeneity at both levels. This includes developing batch models for running large data sets and creating consistent data and analytical output for all 6 urban sites in the project.

- **United States Department of Agriculture & Natural Resource Conservation (USDA & NRCS: 68-52KY-11-058)** project for Creating and Automating Potential Polygon location and Site Characterization for Upland Storage in Watersheds, using Arc Map. A CTI (Compound Topographic Index) based Toolbox was developed using Model Builder (® ESRI) as a part of project deliverables to automate location of these potential sites.
(September 2011- August 2012)

- Research Associate with Water Resource Management Group at IIT Kanpur, for the **Ganga River Basin Management Plan (GRBMP)**, under **Ministry of Environment and Forests Responsibilities**: Included an assessment of the hydrology of the Upper Ganga Basin and working on flow simulation and scenario development for flow calculation. Organization: Indian Institute of Technology (IIT), Kanpur, January to June 2011.

- Research Intern at the Core Geospatial and Utilities (CGO) business Unit Responsibilities at **Risk Management Solution in India (RMSI)**, Dehradun: Created a characteristic model called SMCPM (Scenario Modeling with Catchment Priority Model) which utilizes the SCN method accompanied with SMART and MAUT utilization for user-based criterion input and priority output. 22nd June to 21st August 2010

PUBLICATIONS

Peer-Reviewed Journal Articles & Products

- Caldwell, R. L., Edmonds, D. A., Baumgardner, S., Paola, C., Roy, S., and Nienhuis, J. H.: A global delta dataset and the environmental variables that predict delta formation, Earth Surf. Dynam. Discuss., https://doi.org/10.5194/esurf-2019-12, in review, 2019.
- Roy, S., L. Yoder, V.M. Dias, E. Brondizio. Spatial Clustering using Multiplex Geo-constrained Networks in Amazon River Delta *In Preparation*
- Roy, S., D. A. Edmonds, S. Robeson, A. C. Ortiz. “Decadal Changes in Mississippi Delta Morphology: Analyzing Landscape Patterns using Satellite Time Series Data” *In preparation*
- Swetnam T, S. R. Yool, S. Roy, D.A. Falk (2018) The Ecosystem Moisture Stress Index. *(Submitted for peer review)*Title: The Ecosystem Moisture Stress IndexCorresponding Author: Tyson Swetnam, Co-Authors: Stephen R Yool, Ph.D.; Samapriya Roy, MS; Donald A Falk, Ph.D.
- Ortiz, A. C., S. Roy, and D. A. Edmonds (2017), Land loss by pond expansion on the Mississippi River Delta Plain, Geophys. Res. Lett., 44, doi:10.1002/2017GL073079.
- Mansur, A. V., Brondizio, E. S., Roy, S., Soares, P. P. D. M. A., & Newton, A. (2018). Adapting to urban challenges in the Amazon: flood risk and infrastructure deficiencies in Belém, Brazil. Regional Environmental Change, 18(5), 1411-1426.
- Mansur, A. V., Brondízio, E. S., Roy, S., Hetrick, S., Vogt, N. D., & Newton, A. (2016). An assessment of urban vulnerability in the Amazon Delta and Estuary: a multi-criterion index of flood exposure, socio-economic conditions, and infrastructure.Sustainability Science, 11(4), 625-643.
- Roy, S., & Katpatal, Y. B. (2011). Cyclical Hierarchical Modeling for Water Quality Model-Based DSS Module in an Urban River System. Journal of Environmental Engineering, 137(12), 1176-1184.

Tools and Products (Not an exhaustive list)

- Samapriya Roy. (2019, April 1). samapriya/porder: porder: **Simple CLI for Planet ordersV2 API** (Version 0.2.3). Zenodo. http://doi.org/10.5281/zenodo.2620196
- Samapriya Roy. (2018, October 6). samapriya/satadd: satadd: **CLI pipeline for Planet, Satellogic, Google Earth Engine and Digital Globe Imagery** (Version 0.0.3). Zenodo. http://doi.org/10.5281/zenodo.1450622
- Samapriya Roy. (2018, October 4). samapriya/pygbdx: pygbdx: **Simple CLI for GBDX** (Version 0.0.2). Zenodo. http://doi.org/10.5281/zenodo.1445734
- Samapriya Roy. (2018, September 22). samapriya/Planet-Mosaic-Quads-Download-CLI: **Planet Mosaic Quads Download CLI** (Version 0.0.4). Zenodo. http://doi.org/10.5281/zenodo.1432872
- Samapriya Roy. (2019, January 10). samapriya/geeup: geeup: **Simple CLI for Earth Engine Uploads** (Version 0.1.4). Zenodo. http://doi.org/10.5281/zenodo.2537353
- Samapriya Roy. (2018, September 1). samapriya/Planet-GEE-Pipeline-CLI: **Planet-**

GEE-Pipeline-CLI (Version 0.4.0). Zenodo. http://doi.org/10.5281/zenodo.1407464
- Samapriya Roy. (2018, March 8). samapriya/gee_asset_manager_addon: **GEE Asset Manager with Addons** (Version 0.2.3). Zenodo. http://doi.org/10.5281/zenodo.1194308
- Samapriya Roy. (2018, July 29). samapriya/pydrop: pydrop: **Minimal Python Client for Digital Ocean Droplets** (Version 0.0.3). Zenodo. http://doi.org/10.5281/zenodo.1323340
- Samapriya Roy. (2018, June 30). samapriya/Clip-Ship-Planet-CLI: **Clip-Ship-Batch Planet Command Line Interface** (Version 0.2.5). Zenodo. http://doi.org/10.5281/zenodo.1302068

TECHNOLOGY EXPERIENCE

- **Developer** –Developed **internal** Planet Admin Tool for Bulk Account Creation & Change Subscriptions (https://hello.planet.com/code/devex/psub), as well as **open-source** tools for downloading and preprocessing of remote sensing datasets.
  - Built open source workshops, hackathons, and tutorials for users.
  - Open impact projects URL: https://samapriya.github.io/projects/open-impact/
- **Programming Skills** – Intermediate knowledge of **Python**, **MATLAB**, **JavaScript**, & **Shell Script**.
  - Published Tools – Python & JavaScript (*24*). MATLAB (*4*). Shell Script (*4*).
- **Integration & Automation** – Advanced knowledge: **Git**, **Github**, **Docker**, & **Slackbot**.
  - Pushed Developer Tools through **Gitlab** and **Github**
  - Dockerized tools for High-Performance Cluster Computing using **Singularity** and **Docker**, and used external integration tools such as **Slack**.

PRESENTATIONS & training (*invited*)

- **Stanford Big Earth Hackathon October 6-November 30, 2018** Invited talk how to download data from Planet data API and integration for local analysis and analysis in Google Earth Engine.
- **SatSummit September 19-20 2018: Hands-on Satellite Imagery Processing and Analysis at Scale**. This was a hands-on introduction to Planet Data API and application within Google Earth Engine plus an introduction to Planet's open data products and offerings.
- **Terra 2018 Pointcloud and Remote Sensing Workshop**: Invited talk about Planet data, API mechanics and working with Planet Data inside Google Earth Engine. This was an online workshop along with Joseph Mascaro held at Ensenada, B.C.
- **NEON Data Institute 2018: Remote Sensing with Reproducible Workflows using Python**: Invited talk about Planet data, API mechanics and working with Google Earth Engine. This was an online talk as I joined remotely with participants.
- **Stanford Big Earth Hackathon** April 14-15th 2018, Stanford University: Invited to coordinate use of Planet data and API mechanics to formulate and work on Earth Sciences and big data problems with students as Developer advocate intern.
- **CSDMS 2018 Annual Meeting**, May 22 -24th 2018, Boulder Colorado, USA: Organized Clinic Introduction to Google Earth Engine.
- **American Geophysical Union Fall Meeting 2017**: Invited Talk: Earth Science in Real Time with the Planet SmallSat Constellation. December 11-15th 2017

PRESENTATIONS & training (*other*)

- **Cyverse Container Camp 7th to 9th March**: Container Technology for Scientific Research Introduction to Docker and Singularity images in High-Performance Computing environments.
- **American Geophysical Union Fall Meeting 2017**: Spatial and Temporal Patterns of Land Loss in Mississippi River Delta Submitted for Presentation December 11-15th 2017
- **Polar Geospatial BootCamp 2017**: Focus on looking at high-resolution satellite data along with using the stereoscopic method to create high-resolution digital elevation model. August 7-10th 2017, Minneapolis, Minnesota
- **Google Earth Engine Summit 2017**: Focus on methodology and large-scale data analysis. Mountain View, California. June 12-14th 2017.
- Edmonds, Douglas A., Caldwell, Rebecca L., Baumgardner, Sarah, Paola, Chris, Roy, Samapriya, Nelson, Amelia: A global analysis of human habitation on river deltas. **European Geosciences Union General Assembly**, Vienna, 23-28th April 2017
- Roy, Samapriya., Edmonds, Douglas., Visualizing land loss across high spatio-temporal scales across Louisiana Coast, **Planet Labs** Headquarters December 2016.
- **Deltas Belmont Forum** End of Project Meeting August 2016: Large Scale data analysis and visualization application to specific delta cases along with the urban land cover change.
- **Google Earth Engine Summit 2016**: Focus on methodology and large-scale data analysis. Mountain View, California. June 13-16th 2016.
- **Community Surface Dynamics Modeling System (CSDMS)** Annual Meeting, A Composite Vulnerability for Urban Areas in Deltaic Regions: An application in the Amazon Delta, Colorado. 17-19th May 2016.
- **Indiana Geographic Information Council** Conference 2016. Locally & Globally Applied Classification Algorithms for Urban Land Cover Detection using Earth Engine. May 9-11th May 2016.
- Summer Training at the **United States Army Core of Engineers (USACE)** and South Florida Water Management District (SFWMD) joint Modeling Group (2015): South Florida Water Management Model, West Palm Beach, 26th July to 31st July 2015.
- Roy, Samapriya (2015) Hydrological Modeling for studying impacts of Urbanization: A cross- site assessment at **Community Surface Dynamics Modeling System (CSDMS)** Annual Meeting, Colorado. 26-28nd May 2015
- Roy, Samapriya et.al (2015) Urban Watersheds and urbanizing hydrology: Assessment through dynamic modeling, Oral presentation at the **Association of American Geographers(AAG)** Annual Meeting, April 21-April 25th, 2015
- Roy, Samapriya, Roy Chowdhury, Rinku and Ficklin, Darren (2015) Dynamic Hydrological Modeling using SWAT within Florida Coastal Everglades. **Florida Coastal Everglades LTER** Mid Term Review Meeting, March 11-13, 2015.
- Roy, Samapriya, Darren L. Ficklin, Rinku Roy Chowdhury, Scott Robeson, Jarlath O Neil Dunn, James B Heffernan, Meredith K Steele, Peter M Groffman (2014) Dynamic Assessment of Urban Hydrologic Component using SWAT. **International Long-Term Ecological Research (ILTER)**: All Scientist

Meeting of the Americas, Valdivia, Chile, December 1-3rd, 2014

GRANTS & FELLOWSHIPS

- **College of Arts and Sciences Graduate Student Travel Award** for attending Google Earth Engine Summit 2017 **$200** April 2017.
- Awarded the **Graduate & Professional Student Government Travel Award** for attending Google Earth Engine Summit 2017 **$500** April 2017.
- Awarded the **John Odland Graduate Research Fellowship** to support graduate research **$500** March 2017
- Awarded the **Lester Spicer Department of Geography Poster Award Fellowship** to support graduate research **$250** March 2017
- Awarded the **William R. Black Leadership Memorial Fellowship** for **$500** March 2017
- Co-PI on **Extreme Science and Engineering Discovery Environment (XSEDE) Allocation Grant** along with Douglas Edmonds for 50,000 Super-computing Units and 500 GB storage volume for project "Automated API based Pipeline for high volume satellite data", grant number **TG-GEO160014** at Indiana University.
- **Co-PI** on the **Planet Labs Ambassador program** providing us unprecedented daily satellite data for entire Louisiana coast an estimated value of over **40,000 square kilometers** and estimated access to over **500,000 square kilometers daily (approximately)** maximum access value considering RapidEye is approx. **500,000 x $1.28/sqkm = $640,000**
- **Digital Globe Imagery Grant** for an area of over 1500 square kilometer (estimated value at **$25,500**) April 2016.
- Awarded the **John Odland Graduate Research Fellowship** to support graduate research **$500** March 2016.
- Awarded the **IndianaView Student Scholarship Program** to participate and conduct research **$750** March 2016
- Awarded the **Partners of America (POA) 100,000 Strong** award, for **$1000** towards travel to the ILTER All Scientist Meeting of the Americas, Valdivia, Chile December 2014
- Awarded the **ILTER Travel Award**, for **$500** towards travel to the ILTER All Scientist Meeting of the Americas, Valdivia, Chile December 2014

TEACHING EXPERIENCE

- Lead Instructor, G338: Introduction to Geographic Information Systems, Summer 2017, Indiana University, Bloomington
- Lead Instructor, G237: Mapping our World, Spring 2017, Indiana University, Bloomington
- Lead Instructor, G237: Mapping our World, Fall 2016, Indiana University, Bloomington
- Teaching Assistant, G237: Mapping our World, Spring 2016, Indiana University, Bloomington
- Lead Instructor, G237: Mapping our World, Fall 2015, Indiana University, Bloomington
- Guest Lecture I202 Lecture Topic: Spatial Epidemiology September 25th, 2014 at Indiana University, Bloomington
- Teaching Assistant: Environmental Geology Course, G117 Spring 2013, Indiana University Purdue University, Indianapolis
- Teaching Assistant: Environmental Geology Course, G117 Fall 2012, Indiana

University Purdue University, Indianapolis

- Teaching Assistant: Environmental Geology Course, G117 Spring 2012, Indiana University Purdue University, Indianapolis

AFFILIATIONS & MEMBERSHIPS

Student Member, American Society of Civil Engineers (ASCE) 2008-present
Environmental and Water Resources Institute (EWRI) 2010-present
Student Member, American Association of Geographer (AAG) 2014-present

COMMITTEE MEMBERSHIPS

- Co-Chair for GIS Day at Bloomington, Indiana University, 2016
- College Committee on Graduate Education, Graduate Student Representative (2015-2016)
- Planning Committee for GIS Day at Bloomington, Indiana University 2015.

CERTIFICATIONS & TRAINING

- Collaborative Institutional Training Initiative (CITI) Human Research 2014
- Trimble Geospatial Training: eCognition- analysis strategies August 14th- 15th, 2014

FIELD RESEARCH EXPERIENCE

Field research in Bangladesh – 05/15/2014 to 06/18/2014

- Conducted 140 household surveys, with data collection aimed at assessing socio-economic-political drivers of land use and livelihood vulnerability in 4 villages of the Sundarbans mangrove forest region.